**Title**

Synthesis of Multiscale Transient Analytical, Experimental, and Numerical Modeling of Latent Energy Storage for Asynchronous Cooling

**Author**

Helmns, Dre

**Publication Date**

2019

# Synthesis of Multiscale Transient Analytical, Experimental, and Numerical Modeling of Latent Energy Storage for Asynchronous Cooling

by

Dre Helmns

A dissertation submitted in partial satisfaction of the

requirements for the degree of

Doctor of Philosophy

in

Mechanical Engineering

in the

Graduate Division

of the

University of California, Berkeley

Committee in charge:

Professor Van P. Carey, Chair
Professor Chris Dames
Professor Per-Olof Persson

Spring 2019

# Synthesis of Multiscale Transient Analytical, Experimental, and Numerical Modeling of Latent Energy Storage for Asynchronous Cooling

# Abstract

Synthesis of Multiscale Transient Analytical, Experimental, and Numerical Modeling of Latent Energy Storage for Asynchronous Cooling

by

Dre Helmns

Doctor of Philosophy in Mechanical Engineering

University of California, Berkeley

Professor Van P. Carey, Chair

Novel energy technologies have the potential to address climate change by efficiently using natural resources and reducing greenhouse gas emissions into our shared global atmosphere. In preparation for a future society powered by renewables, engineering solutions must include environmentally conscious and cost-effective methods to store, transport, and convert energy.

I have numerically investigated the use of latent thermal energy storage (TES) technology, with solid to liquid phase change material (PCM), to shift cooling loads to off-peak hours. I first non-dimensionalized differential equations describing sensible and latent heat transfer in the PCM, and their finite difference counterparts, in order to facilitate scaling for the wide array of asynchronous cooling applications that could benefit from this technology. Next, I compared closed form analytical solutions and experimental testing of a TES prototype with the numerical prediction of its melting and freezing processes. Both the analytical solutions and the experimental tests matched the predicted results within 10% agreement, validating the computational model's capacity to capture the physics governing the transient behavior of the device with high precision and accuracy. As no adjustable parameters were tuned to maximize agreement, the numerical model can be effectively employed to determine the performance of different designs without the need to fabricate, charge, and test them.

Using this model, I explored potential improvements to power and refrigeration cycles for power plants and commercial buildings integrated with thermal storage. I accomplished this task by taking simple representations of these systems in MATLAB and transforming them into declared relationships between complex components using the dynamic programming language of Modelica. Simulations in integrated development environments of both languages demonstrate improvements of up to a 1.4% increase in power plant energy output and a 2.4% decrease in building chiller energy consumption with thermal storage. With thoughtful selection of the phase change material and better charging and discharging control strategies for the thermal energy storage, further performance enhancement of such systems can be achieved.

to my chosen family

This goes out to all the real ones, blood and otherwise, who have supported me along the way. To my mom, for reminding me that each generation must surpass the one before, and pushing me to get these three letters so that others would respect me even if they cannot understand me. To my friends at UC Berkeley, for being my shoreline in the endless ocean of academia and helping me find solid ground to stand on every single day. To my homies on the outside who have been so proud of me for accomplishing a research feat that I still don't have the language to articulate. To my queer and trans community for reminding me why I'm here; until all marginalized communities are represented at every level of these institutions, equality will never be achieved. With abundant gratitude, love, and solidarity.

-dre

# Contents

# List of Figures

# List of Tables

# Acknowledgments

I offer my sincerest thanks to Professor Van P. Carey who guided me through my tenure in the Mechanical Engineering MS/PhD program. Without his unwavering support and words of encouragement, I assuredly would not be finishing this degree. I am grateful for the opportunity to work with my former research project partners, Zach Theroff and Lauren Gagnon, who made coming to lab collaborative and fun. I seriously appreciate you reading my papers, deciphering my code, and giving me invaluable feedback along the way. I would like to extend my gratitude to everyone I've had the privilege to share space with in the Energy and Multiphase Transport Lab. Dave, Ruth, Claire, Jordan, Zach, Paige, Lauren, Emma, Sam, and Alanna, I've learned something and grown from my relationships with each of you. Thanks for working on math and sketching pictures at our reappropriated whiteboard with me. I have thoroughly enjoyed cooking together, sharing food, playing boardgames, and laughing at the absurdity of it all. I've met some incredible people beyond the windowless walls of 5117 too. Eric Ibarra, I can't thank you enough for your friendship through tough classes and rough patches that I'm so glad we've made it through. Josh Wilbur, you are one of my favorite people on this strange rock. Thank you for all of our holy place kombucha breaks, prelim exam study escapes, and making me feel safe whenever you're around.

# Chapter 1

# Introduction

*Hypothesis*: Thermal energy storage (TES) with phase change material (PCM) can decrease the low system temperature of power or refrigeration cycles and lead to improved efficiency.

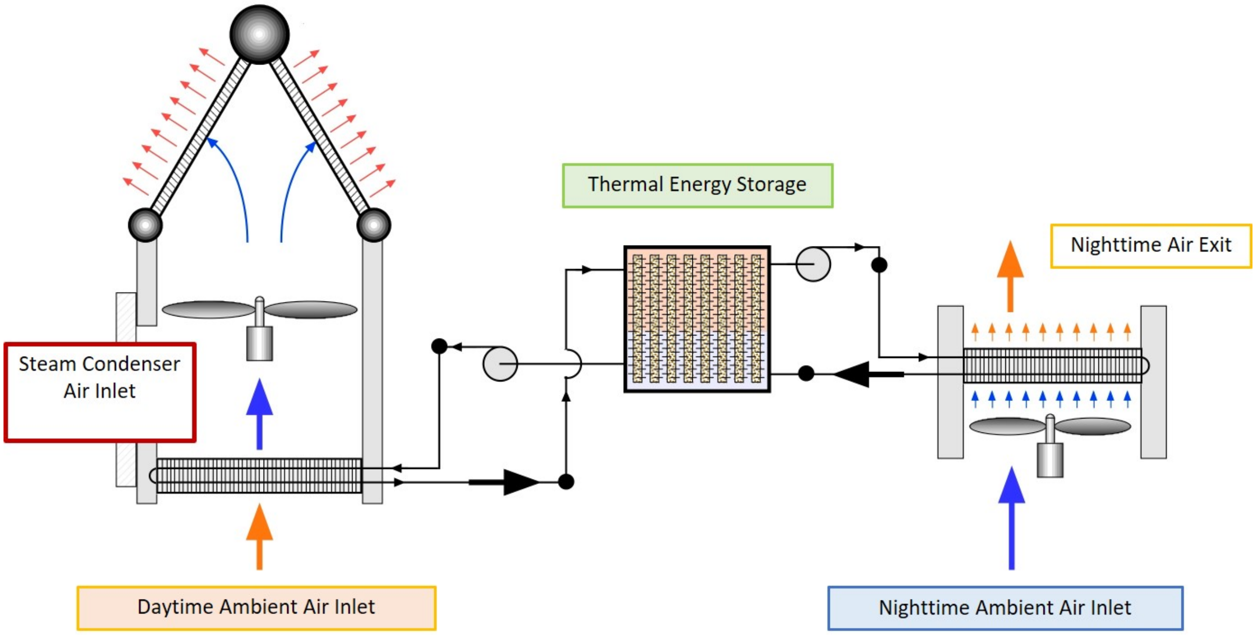

Figure 1.1: Thermal energy storage integrated into an asynchronous cooling system.

This dissertation will outline numerical models designed to test this hypothesis by demonstrating performance improvements for an air cooled steam condenser or water cooled pre-conditioning coil. An example of this type of asynchronous cooling system is shown in 1.1.

## 1.1 Overview

This chapter presents an analysis of a thermal energy cold storage device containing phase change material that can be melted or frozen by circulating a chilled working fluid through it. During cold charging, the cold working fluid flows into and through the tubes of the storage unit, transferring heat from the matrix structure to the working fluid in order to freeze the PCM. During cold extraction, the hot working fluid flows into and through the tubes, transferring heat to the matrix structure of the storage unit, thereby cooling the working fluid by melting the PCM.

## 1.2 Motivation

The proposed TES device can be used to gather energy during the day, store it, and then reject it asynchronously (at night) rather than continuously throughout the day as is standard in many applications. This is particularly useful for a number of reasons. First, asynchronous cooling removes the need for peak load production, which is typically more expensive both financially and environmentally. Second, temperature differences are greater at night when ambient air is cooler, rendering heat transfer more thermodynamically efficient (from a simple Carnot standpoint). The type of cold storage considered here can be used for asynchronous cooling in a number of applications including rural refrigeration, building air conditioning, and steam power plants [36]. For example, cold storage can be accomplished overnight by cooling a working fluid in an air-cooled heat exchanger and circulating the cooled working fluid through the cold thermal energy storage unit. Then, during the day, when outside temperatures peak, the working fluid can be chilled by sending it through the thermal storage unit and the resulting chilled working fluid can be used to enhance condenser cooling. Augmented cooling via thermal energy storage of phase change material can increase the efficiency of power or refrigeration cycles [13].

The idea is to provide a cold sink for this air cooled condenser without wasting water or burning additional fuel. In other words, the aim is to decrease the cold temperature at which heat is rejected. This proposal is novel because condensers commonly reject heat to ambient air or other surroundings continuously throughout operation. Here, the energy is stored and asynchronously rejected when the temperature difference with this heat sink is more favorable.

## 1.3 Effectiveness Modeling

### TES Energy Balance

We assume the working fluid in the storage unit either flows through a single passage or the flow is manifolded to multiple identical passages. Turns are ignored here for the purposes of this analysis and we instead focus on a unit cell of one long passage, with the mass flow rate

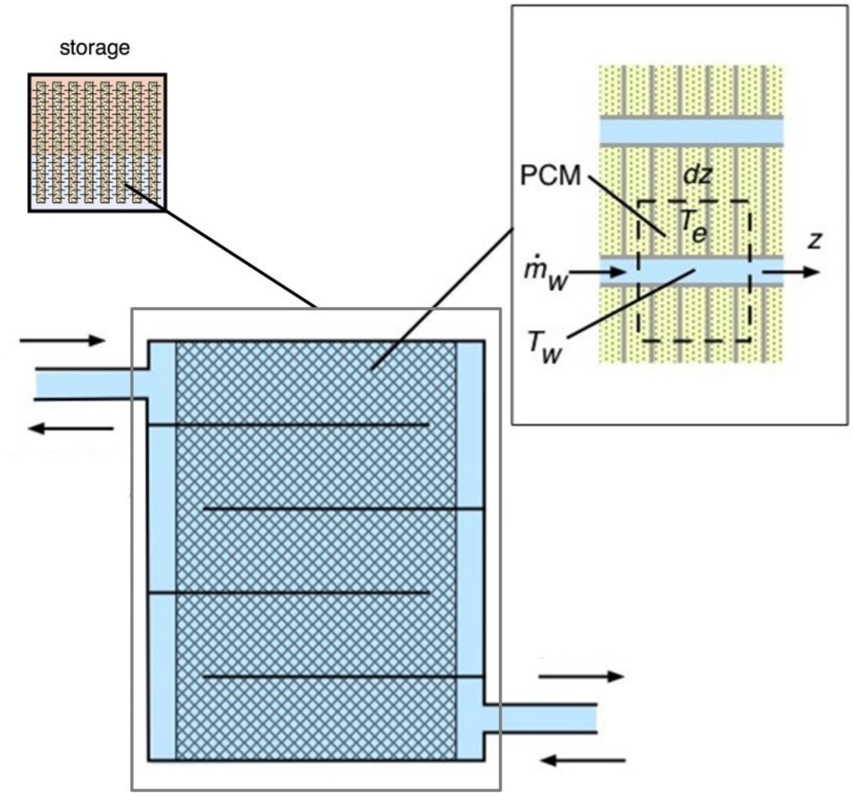

Figure 1.2: Schematic of a differential element of the flow path through a TES unit.

per passage designated as $\dot{m}_w$. The unit cell, of length $dz$, is composed of the working fluid flow passage and the surrounding PCM section. This element includes the tube wall and fin structures that conduct heat into the PCM material.

To derive the governing equations, we start with a control volume analysis, with one control volume around a differential element of the PCM matrix and another around a differential section of the flow passage. We apply the conservation of energy to each of these control volumes, noting that the stored thermal energy must be balanced by the thermal energy transport across the control surfaces of each unit cell.

From the definition of enthalpy for a solid-liquid mixture, thermal energy in the PCM matrix can be stored in sensible and latent forms [55]. The differential change in enthalpy of the storage element is designated as $dH_e$:

$$dH_e = \rho_e \nu' dz[c_{p,e}(T_e - T_{ref}) + x_e h_{ls}] \tag{1.1}$$

where $\bar{\rho}_e \nu' dz$ is the mass of PCM, $\bar{c}_{pe}(T_e - T_{ref})$, and $x_e h_{ls}$ reflects its sensible and latent thermal energy respectively. The above expression is differentiated with respect to time, and an energy balance is written between change in stored enthalpy of the element and the convective and conductive heat transfer across control surfaces to this element [5]. We use

Newton's Law of Cooling as the constitutive equation to describe what form the heat transfer takes across the control surface separating the PCM matrix and flow passage:

$$\frac{\partial(dH_e)}{\partial t} = Us_w dz(T_w - T_e) \tag{1.2}$$

where $Us_w dz$ is the conductance from the working fluid to the PCM matrix and $(T_w - T_e)$ is the driving temperature difference. Taking the time derivative of the right hand side of Eqn. (1.1) and dividing through by constants $\bar{\rho}_e \nu' dz \bar{c}_{pe}$, we can group like terms to formulate a governing equation relating stored enthalpy change to conductive and convective heat transfer into or out of the unit cell:

$$\frac{\partial T_e}{\partial t} + \frac{\partial x_e}{\partial t}\left(\frac{h_{ls}}{\bar{c}_{pe}}\right) = \frac{Us_w}{\bar{\rho}_e \bar{c}_{pe} \nu'}(T_w - T_e) \tag{1.3}$$

In Equation (1.3), at a given location, either the element temperature, $T_e$ (sensible heat transfer), or the melt fraction, $x_e$ (latent heat transfer), can change with time, but not both simultaneously. Therefore, the governing differential Eqn. (1.3) can be split into the following two forms for sensible and latent heat transfer:

$$\frac{\partial T_e}{\partial t} = \frac{Us_w}{\bar{\rho}_e \bar{c}_{pe} \nu'}(T_w - T_e) \quad ; \quad \frac{\partial x_e}{\partial t} = 0 \tag{1.4}$$

$$\text{for } T_e \neq T_m \text{ and } x_e = 0 \text{ or } x_e = 1.$$

$$\frac{\partial x_e}{\partial t} = \frac{Us_w}{\bar{\rho}_e h_{ls} \nu'}(T_w - T_e) \quad ; \quad \frac{\partial T_e}{\partial t} = 0 \tag{1.5}$$

$$\text{for } T_e = T_m \text{ and } 0 < x_e < 1.$$

Likewise, conservation of energy on a control volume around the working fluid (inside the flow passage) of the unit cell requires that stored energy must be balanced by advection as well as heat transfer to and from the PCM matrix:

$$\frac{\partial T_w}{\partial t} = -\left(\frac{\dot{m}_{closed}}{\rho_w A_c}\right)\frac{\partial T_w}{\partial z} + \frac{Us_w}{\rho_w A_c c_{p,w}}(T_e - T_w) \tag{1.6}$$

These energy balances neglect conduction in the downstream direction. One can show that the ratio of stream-wise conduction to transport to or from the PCM is small for TES designs of interest. In other words, the heat diffusion effect is small compared to convection and conduction normal to the flow passage walls for the configuration considered here. These coupled equations are first order in time and space, necessitating initial conditions for temperatures and melt fraction as well as a boundary (inlet) condition for the working fluid temperature.

## TES Governing Equations

Drawing upon previous work, we can formulate the governing energy balance equations using dimensionless numbers and use these to resolve the temperature and melt fraction fields within the TES device [45, 57, 21, 20]. The transport equations are written in terms of dimensionless position, time, and temperature. Position is non-dimensionalized by dividing by the length of the flow passage. Time is non-dimensionalized by dividing by the residence time of the working fluid in the storage device. Temperature is non-dimensionalized by dividing by the maximum temperature difference experienced in the system. This is done because the TES absorbs heat in one range and rejects it in another, dictating the minimum and maximum temperatures for the system during the cycle. With this constraint, the melt temperature, $T_m$, should fall somewhere between $T_{min}$ and $T_{max}$.

$$\theta = \frac{T_e - T_{min}}{T_{max} - T_{min}} \quad , \quad \phi = \frac{T_w - T_{min}}{T_{max} - T_{min}} \tag{1.7}$$

$$\hat{z} = \frac{z}{L} \quad , \quad t^* = \frac{t}{t_{res}} \quad , \quad t_{res} = \frac{\rho_w A_c L}{\dot{m}_w} \tag{1.8}$$

Replacing dimensional parameters with their dimensionless counterparts converts the equations to

$$\frac{\partial \phi}{\partial t^*} = -\frac{\partial \phi}{\partial \hat{z}} + N_{tu}(\theta - \phi) \tag{1.9}$$

for sensible heat transfer in the flow passage and

$$\frac{\partial \theta}{\partial t^*} = N_{tu} R_{we}(\phi - \theta) \quad ; \quad \frac{\partial x_e}{\partial t^*} = 0 \tag{1.10}$$

$$\text{for } \theta \neq \theta_m \text{ and } x_e = 0 \text{ or } x_e = 1.$$

$$\frac{\partial x_e}{\partial t^*} = N_{tu} R_{we} \mathrm{St_{io}}(\phi - \theta) \quad ; \quad \frac{\partial \theta}{\partial t^*} = 0 \tag{1.11}$$

$$\text{for } \theta = \theta_m \text{ and } 0 < x_e < 1.$$

for sensible and latent heat transfer in the storage element where

$$N_{tu} = \frac{U s_w L}{\dot{m}_w c_{pw}}, \quad R_{we} = \frac{\rho_w c_{pw} A_c}{\rho_e c_{pe} \nu'}, \quad \mathrm{St_{io}} = \frac{c_{pe}(T_{max} - T_{min})}{h_{ls}} \tag{1.12}$$

The parameters in the non-dimensional governing transport equations are dimensionless groups with physical relevance. $N_{tu}$, the number of transfer units, is used to specify dimensions and quantify the heat transfer rate associated with different designs. $R_{we}$, the ratio of thermal capacities, can be used to select an appropriate PCM. The Stefan number, $\mathrm{St_{io}}$, indicates whether heat transfer will be primarily sensible or latent.

The partial differential Eqns. (1.9), (1.10), and (1.11) are solved numerically via an explicit finite difference discretization of the domain. The derivatives are replaced with forward difference algebraic expressions. For this finite difference discretization of derivatives, the initial and boundary conditions can be specified to model the cycling of the storage device [40]. In particular, we can set initial conditions for extraction (melting) or charging (freezing) to match the thermally equilibrated state after periods of storage. Furthermore, the transient inlet boundary condition can account for coupling with an external heat exchanger and the varying temperatures and fluctuating heat transfer rates experienced there.

$$\text{At} \quad t^* = 0: \quad \theta = \theta(\hat{z}), \quad x_e = x_e(\hat{z}), \quad \phi = \phi(\hat{z}) \qquad \text{for } 0 \leq \hat{z} \leq 1. \tag{1.13}$$

$$\text{At} \quad \hat{z} = 0: \quad \phi = \phi(t^*) \qquad \text{for } t^* > 0. \tag{1.14}$$

With any numerical method, it is imperative to ensure both stability and consistency of results. Due to the explicit nature of the Forward Euler and Upwind schemes, stability is only attainable below threshold values of $\Delta t^*$ and $\Delta \hat{z}$. In order to increase the time step and grid size (thereby reducing computation time), it might be necessary to write derivatives as well as solve the governing equations differently. This can be accomplished via established methods for advective equations (e.g. Lax-Wendroff), or, the application of parabolic problem solutions to hyperbolic systems (e.g. Crank-Nicolson).

In order to quantify how well the storage device works, we define a performance metric for the extraction and charging loops. Effectiveness, $\varepsilon_{tes}$, is the calculated melt fraction at the last time step to the melt fraction if the PCM is either completely melted or solidified.

Extraction effectiveness is defined as:

$$\varepsilon_{tes,ext} = \frac{\sum_{\hat{z}=0}^{1} x_e(t^*_{end}, \hat{z})}{\sum_{\hat{z}=0}^{1} x_{e,max}(t^*, \hat{z})} \quad \text{where} \quad x_{e,max} = 1 \tag{1.15}$$

where we neglect the contributions via sensible storage because, for the applications with small operating temperature differences considered here, latent storage dominates. This is consistent with the low Stefan number approximation adopted later in this dissertation. Charging effectiveness, like extraction effectiveness, is defined as:

$$\varepsilon_{tes,char} = \frac{\sum_{\hat{z}=0}^{1} 1 - x_e(t^*_{end}, \hat{z})}{\sum_{\hat{z}=0}^{1} 1 - x_{e,min}(t^*, \hat{z})} \quad \text{where} \quad x_{e,min} = 0 \tag{1.16}$$

It follows that the effectiveness is a function of the dimensionless parameters in the model:

$$\varepsilon_{tes} = \varepsilon_{tes}(t^*, N_{tu}, R_{we}, \mathrm{St}_{\mathrm{io}}) \tag{1.17}$$

where the functional relation for $\varepsilon_{tes}$ is embodied in the solution of the dimensionless differential equations. This formulation also defines the key dimensionless parameters that dictate performance and facilitates analysis to define optimal ranges of these parameters. The overall effectiveness of the device should be taken as the minimum between extraction and charging and could be improved by adjusting working fluid mass flow rate and operation time ($t^*$) for a given design geometry ($N_{tu}$), phase change material ($R_{we}$), and operating conditions ($\mathrm{St_{io}}$).

## 1.4 Parametric Studies

As mentioned above in the derivation of the governing equations, the values of dimensionless groups $t^*$, $N_{tu}$, $R_{we}$, and $\mathrm{St_{io}}$ are embodied in the effectiveness prediction for a potential TES unit. To better understand this functional relationship, we can examine the parameters individually and establish desired ranges of these for high effectiveness designs.

### Variation of $N_{tu}$

In examining these dimensionless groups, we will start with $N_{tu}$ which incorporates the overall heat transfer coefficient, $U$, in its definition. The analytical framework is set up for a constant $N_{tu}$ based on a mean $\bar{U}$ value, which must be averaged both spatially and temporally as described in Chapter 2. With an average $\bar{U}$ determined, we can look at how its corresponding dimensionless counterpart, $N_{tu}$, impacts effectiveness.

For specified values of the storage design parameters $R_{we}$, $\mathrm{St_{io}}$, and $\theta_m$, computations can be done for different combinations of $N_{tu}$ and dimensionless termination time, $t^*_{end}$, to determine the resulting effectiveness of the extraction and charging processes. Figure 1.3 illustrates the results of multiple solutions to define the dependence of the effectiveness on $t^*_{end}$ and $N_{tu}$.

From this figure, we can draw conclusions on what a reasonable value for $N_{tu}$ should be in order to achieve a target effectiveness (for a specified $R_{we}$ and $\mathrm{St_{io}}$). For high efficiency TES devices, the recommended range of $N_{tu}$ is between 1.0 - 12.0 for a reasonable operation time ($t^*_{end} > 15$) and conditions ($R_{we} = 1$, $\mathrm{St_{io}} = .1$) as device operation below this threshold cannot achieve desired effectiveness targets. As $N_{tu} = U s_w L / \dot{m}_w c_{p,w}$, the recommendation that $N_{tu}$ should be one or greater is a reflection that the heat transfer to/from the PCM matrix must equal or outweigh the working fluid's capacity to advect the energy along the flow passage.

In most design scenarios, there is a fixed time window for operation and an impetus to make the TES as small as possible while still accomplishing heat transfer during that time. This inevitably leads to a design trade-off between $t^*_{end}$ and $N_{tu}$. If the process can take longer, the task can be done with a smaller heat exchanger, or conversely, if the TES device is larger, the process can take less time. In order to go about examining the design space for an effective TES device, there are a couple of insights that can be gained from Fig. 1.3. There are several regimes which are of great interest. At low $N_{tu}$ ($N_{tu} \leq 1$), the only way to achieve high performance is to greatly increase $t^*_{end}$. To do this would entail increasing the total operation time or decreasing the residence time in the flow passage. Lowering the residence time could be done by selecting a lower density fluid, decreasing the channel cross

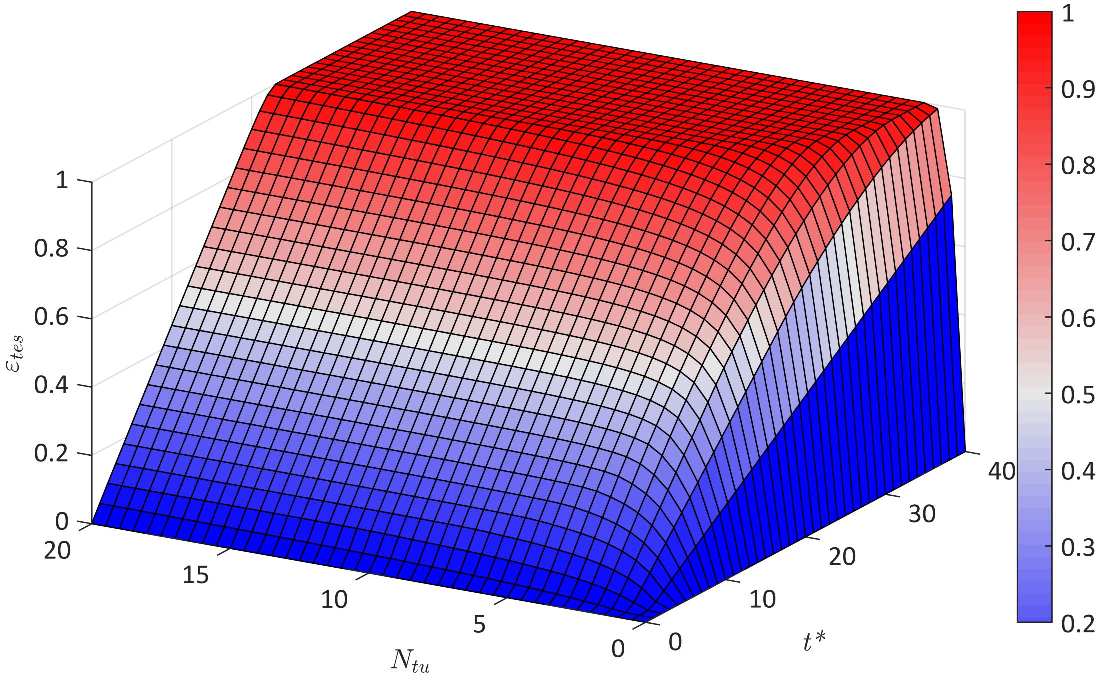

Figure 1.3: Predicted effectiveness variations with $t^*_{end}$ and $N_{tu}$ for $R_{we} = 1$, $\mathrm{St_{io}} = .1$, $\theta_m = .5$, and extraction starting from a completely frozen state or charging starting from a completely melted state with constant thermal properties.

sectional area, decreasing the length of the flow passage, or increasing the mass flow rate. At mid-range $N_{tu}$ $(1.0 < N_{tu} < 12.0)$, there is some room to decrease $t^*_{end}$ while increasing $N_{tu}$ and vice versa. $N_{tu}$ can be increased by enhancing the overall heat transfer, increasing the heat transfer area, decreasing the mass flow rate or specific heat of the working fluid. At high $N_{tu}$ $(N_{tu} \geq 12)$, we notice diminishing returns. Any further increase in $N_{tu}$ will not make much difference, and the only relevant parameter to adjust is $t^*_{end}$. In this range of $N_{tu}$, once $t^*_{end}$ is increased to the point of achieving a desired effectiveness value, any further increase in $t^*_{end}$ is superfluous. This will be examined further in Chapter 3.

## Variation of $R_{we}$

For specified values of the storage design parameters $N_{tu}$, $\mathrm{St_{io}}$, and $\theta_m$, computations can be done for different combinations of $R_{we}$ and dimensionless termination time, $t^*_{end}$, to determine the resulting effectiveness of the extraction and charging processes. Figure 1.4 illustrates the results of multiple solutions to define the dependence of the effectiveness on $t^*_{end}$ and $R_{we}$.

From this figure, we can draw conclusions on what a reasonable value for $R_{we}$ should be in order to achieve a target effectiveness (for a specified $N_{tu}$ and $\mathrm{St_{io}}$). For high efficiency TES

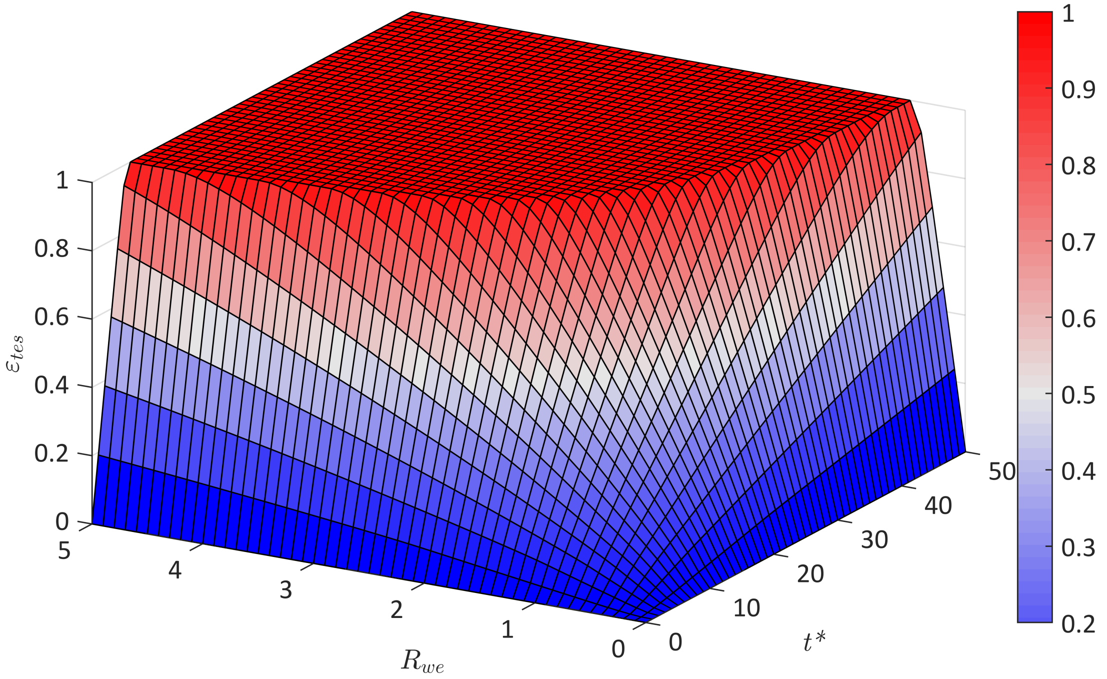

Figure 1.4: Predicted effectiveness variations with $t^*_{end}$ and $R_{we}$ for $N_{tu} = 10$, $\mathrm{St_{io}} = .1$, $\theta_m = .5$, and extraction starting from a completely frozen state or charging starting from a completely melted state with constant thermal properties.

devices, the recommended range of $R_{we}$ is between 0.4 - 1.8 for a reasonable operation time ($t^*_{end} > 15$) and conditions ($N_{tu} = 10$, $\mathrm{St_{io}} = .1$) as device operation below this threshold cannot achieve desired effectiveness targets. As defined, $R_{we} = \rho_w c_{p,w} A_c / \bar{\rho}_e \bar{c}_{pe} \nu'$, so the recommendation that $R_{we}$ be somewhere near unity is a reflection that the working fluid and PCM should have a similar energy capacity.

## Variation of $\mathrm{St_{io}}$

For specified values of the storage design parameters $N_{tu}$, $R_{we}$ and $\theta_m$, computations can be done for different combinations of $\mathrm{St_{io}}$ and dimensionless termination time, $t^*_{end}$, to determine the resulting effectiveness of the extraction and charging processes. Figure 1.5 illustrates the results of multiple solutions to define the dependence of the effectiveness on $t^*_{end}$ and $\mathrm{St_{io}}$.

From this figure, we can draw conclusions on what a reasonable value for $\mathrm{St_{io}}$ should be in order to achieve a target effectiveness (for a specified $N_{tu}$ and $R_{we}$). For high efficiency TES devices, the recommended range of $\mathrm{St_{io}}$ is between 0.06 - 0.20 for a reasonable operation time ($t^*_{end} > 15$) and conditions ($N_{tu} = 10$, $R_{we} = 1$) as device operation below this threshold cannot achieve desired effectiveness targets. The Stefan number is written

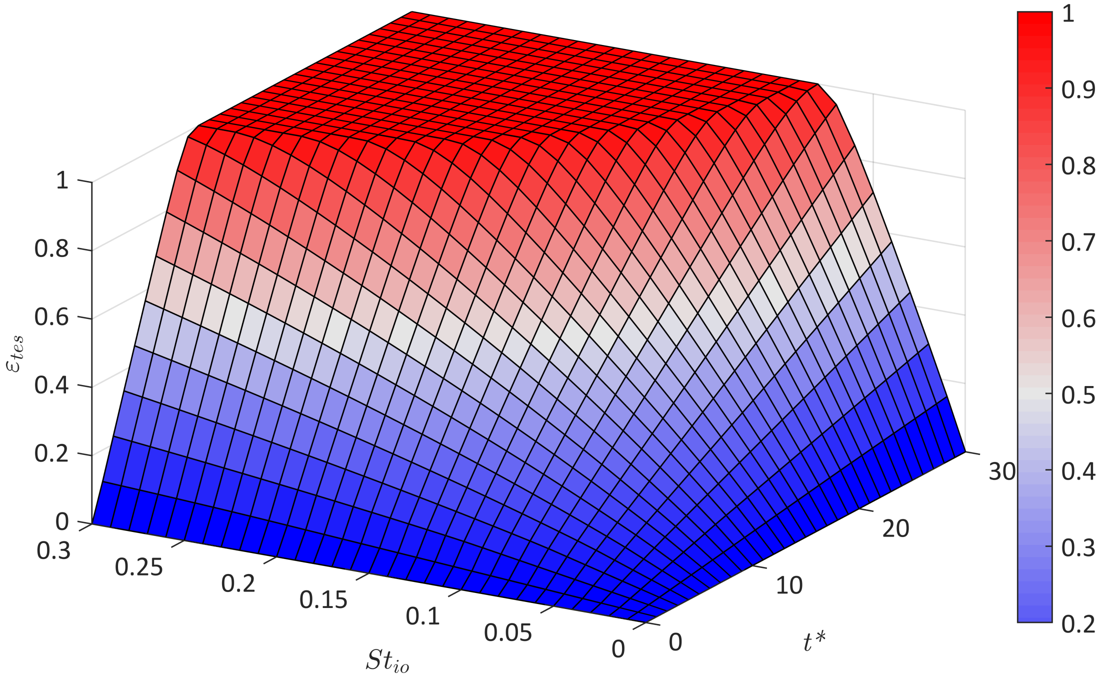

Figure 1.5: Predicted effectiveness variations with $t^*_{end}$ and $\mathrm{St_{io}}$ for $N_{tu} = 10$, $R_{we} = 1$, $\theta_m = .5$, and extraction starting from a completely frozen state or charging starting from a completely melted state with constant thermal properties.

as $\mathrm{St_{io}} = \bar{c}_{pe}(T_{max} - T_{min})/h_{ls}$. This dimensionless group reflects the ratio of sensible to latent heat transfer. As such, it makes sense that for the thermal energy storage we aim to accomplish, employing phase change in a constrained temperature range, the latent heat transfer and resulting effectiveness should be high, rendering $\mathrm{St_{io}}$ less than one, consistent with the low Stefan number approximation adopted here.

## Key Takeaways from Parametric Studies

These parametric studies are particularly valuable in defining an appropriate design space for the TES. From a practical perspective, it is important to parse through the suggested ranges and make design decisions. The ratio of thermal capacities, $R_{we}$, is set early on by selecting materials for the working fluid and PCM and is constrained by the properties of both of these. The Stefan number, $\mathrm{St_{io}}$, is defined by the operating conditions of the system and is constrained by the ambient temperatures surrounding the subsystem. The least constrained terms in designing a TES device are $N_{tu}$ and $t^*_{end}$. Optimizing effectiveness is a trade-off between these two parameters.

Results further show that modeling or prototype experiments can provide $U$ data that can be used to design large scale TES units for relevant applications. The analysis framework developed here provides the means for establishing the required values of $U$ and its corresponding dimensionless parameter, $N_{tu}$, needed to achieve a specific level of extraction and charging effectiveness.

## 1.5 Conclusions

After deriving the relevant conservation and performance equations, we examined various parameters of a thermal energy storage device to determine an effective and efficient design space. We used these parametric studies to define the required combination of dimensionless parameters for a high performing device.

We indicate which dimensionless parameters affect performance as well as the relationship between them. $R_{we}$ relates the thermal capacities of the working fluid to typical phase change materials. This parameter can be optimized between $\sim .4 - 1.8$ by selecting a working fluid with ideal thermal properties as well as a low cost phase change material with high energy density. $\mathrm{St}_{\mathrm{io}}$ relates sensible to latent heat transfer in the phase change material. This can be varied by adjusting the initial condition of the TES unit to incorporate greater subcooling or superheating. This study, instead, focused primarily on demonstrating the usefulness of this device by defining a performance metric, $\varepsilon_{tes}$, that quantified how much latent heat transfer via phase change occurred rendering $\mathrm{St}_{\mathrm{io}}$ between $\sim .06 - .20$. $N_{tu}$ corresponds most directly to heat exchanger effectiveness as it encapsulates transport parameters including $\dot{m}_{closed}$ and $U$; it is optimal between $\sim 1.0 - 12.0$. It is apparent that there is a threshold dimensionless time, $t^*$, in order to reach prescribed effectiveness targets. Optimizing design of a TES device and subsystem often requires a trade-off between $t^*_{end}$ and $N_{tu}$. For different $N_{tu}$, $R_{we}$, and $\mathrm{St}_{\mathrm{io}}$, the time required to complete the prescribed amount of latent heat transfer varies. Once the required values of $N_{tu}$, $R_{we}$, $\mathrm{St}_{\mathrm{io}}$, and $t^*_{end}$ are defined, detailed design of the thermal storage unit can be focused on the goal of establishing a flow passage and PCM packaging design that achieves the required values of these parameters. This framework thus can be used to optimize the thermal energy storage device for repeated cycling in load shifting applications.

The remainder of this work will employ the equations derived in this chapter to multiple aspects of thermal storage. First, analysis will zoom in to focus on a heat transport in a single unit cell, which is necessary to effectively define dimensionless parameters. Then, the scope will expand to include other components that interact with a storage device in the subsystem model. The findings at the unit cell, device, and subsystem scales will be validated by experimental data. From there, the modeling will be applied beyond the simple case studies provided in intermediate chapters. The culmination of this work will involve extrapolating beyond simple coding to fully develop and explore the relationships among relevant variables for a building energy system.

# Chapter 2

# Unit Cell Model

## 2.1 Introduction

In this chapter, we examine several approaches to determining an appropriately space and time averaged overall heat transfer coefficient for a heat exchanger containing PCM undergoing both sensible and latent heat transfer. We focus on theoretically modeling the overall heat transfer coefficient, $U$, for a thermal energy storage device. Analysis is based on a modified Stefan problem approach to account for the increasing thermal resistance in the phase change material over time. This method incorporates the varying position of the phase change interface when determining the overall heat transfer coefficient. With $U$ defined, we focus on our second objective of evaluating the performance of a selected TES design. Using the dimensionless framework in Chapter 1, we quantify the efficiency of the energy input and extraction processes, as well as the effectiveness of repeated cycling. From here, the advantages and disadvantages of different geometric configurations can be assessed. Thanks to the non-dimensionalization of the domain and relevant parameters, the unit can be scaled for various heating and cooling applications. The analysis in this chapter shows that using a time averaged heat transfer coefficient for Stefan-like melting or freezing of phase change material is a valid approach to modelling sensible and latent heat transfer of a TES unit.

Phase change materials, especially in relation to thermal energy storage, have been studied quite extensively, though few have pursued a means of accounting for the variable conductance during the phase change process [56]. There are a handful of papers, however, that should be addressed. An approach for handling the transient effects during latent heat transfer was developed by Lacroix [31]; while the strategy of using an enthalpy approach is similar to the present paper, Lacroix neglected to give explicit treatment to the transient thermal conductance as the present paper does. El-Dessouky and Al-Juwayhel performed analysis on phase change thermal energy storage systems using a second law approach. Their work focused on the cyclic melting and freezing of PCM. However, a number of assumptions were made, limiting the scope of the approach. For example, the phase change material was assumed to be at its melt temperature throughout, rather than tracking the location of the melt front and allowing sensible heat storage [46, 11]. Again, the present paper is based on an enthalpy approach, as was the work by Ismail and Gonçalves. To solve the conduction problem numerically, they employed an alternating direction implicit method [25]. By using an implicit method, an extra level of complexity is added to the computation process. The present paper uses an *effectiveness*-NTU (number of transfer units) method, also called an $\varepsilon$-NTU method, to develop an explicit solution. While Tay, Belusko, and Bruno also used an $\varepsilon$-NTU method, their process resulted in an analytical solution. They used a variable conductance model which accounted for a change in $U$ related to a moving melt front [48]. However, their analysis is focused on determining the effectiveness of a TES device via basic $\varepsilon$-NTU relations, whereas the present paper applies numerical methods to simulate the TES device performance and compare with an average $N_{tu}$ value.

## Definition of Unit Cell

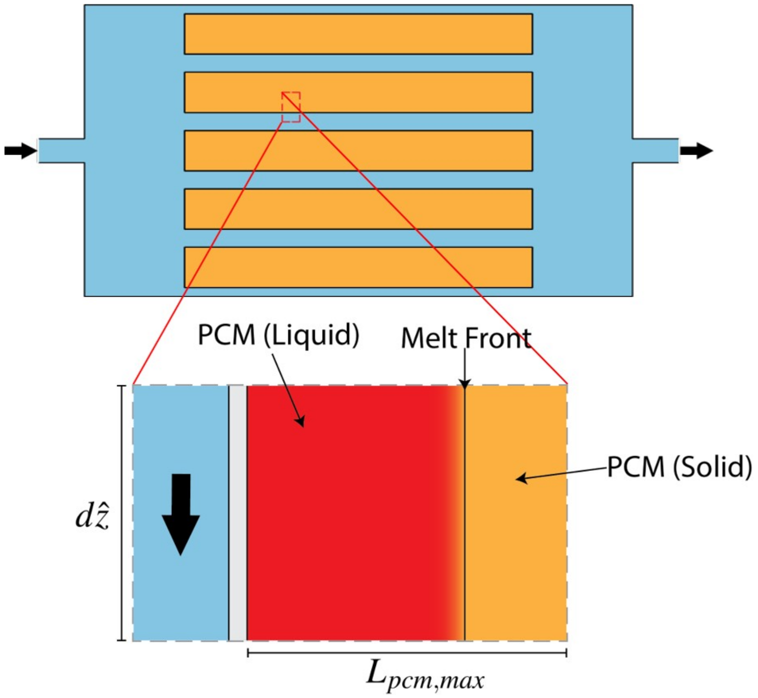

Figure 2.1: Unit cell within thermal storage device showing partially melted PCM.

The problem considered in this paper revolves around a one-dimensional heat transfer problem that consists of convection from a working fluid to a thin wall and pure conduction from this wall to the melt front of a portion of PCM. This finite element is represented in Fig. 2.1, which is defined as the "unit cell." The size of the unit cell is $d\hat{z}$ by $L_{pcm,max}$. The arrow indicates the flow direction of working fluid. This one-dimensional heat transfer problem can be repeated along the direction of the flow with changes in the working fluid temperature as energy is transferred to the unit cells.

## 2.2 Prediction of Overall Heat Transfer Coefficient

The effectiveness modeling in Chapter 1 includes the overall heat transfer coefficient, $U$, in the governing equations by incorporating it into the dimensionless parameter, $N_{tu}$. The overall heat transfer coefficient is defined from the flow passage centerline to the PCM adiabat between parallel flow passages, which can be understood from 2.2. The overall heat transfer coefficient and must include convection in the working fluid and conduction in the storage matrix. The framework is based on a mean $U$ value, which must be averaged both spatially and temporally.

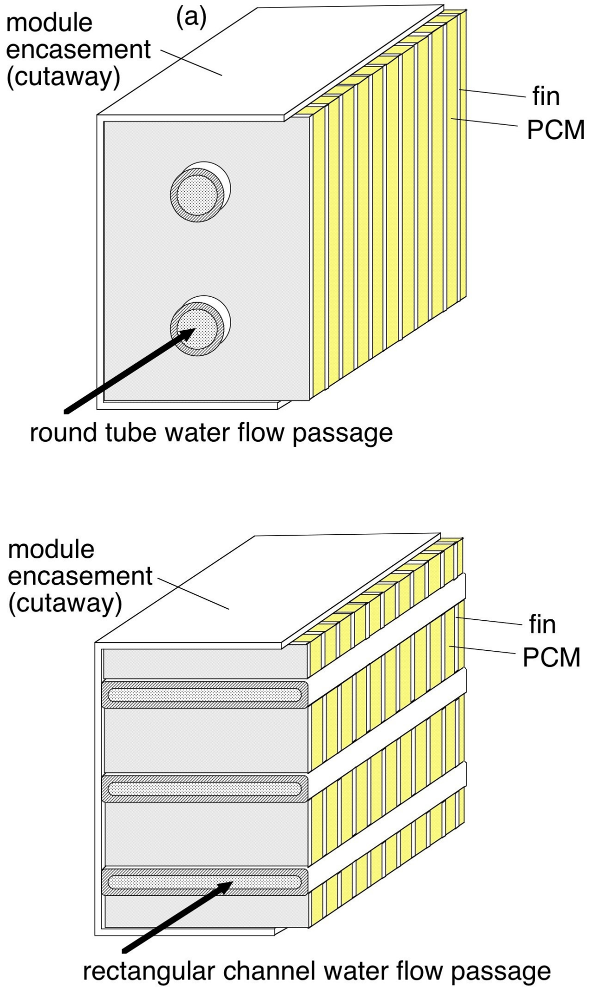

Figure 2.2: Round tube and rectangular channel flow passage designs with fins in PCM.

$U$ varies in the TES unit because the heat transfer that occurs during extraction and charging is a transient process. Spatial variation is typical of most heat exchangers with convective heat transfer coefficients that decrease along the flow channel as the temperature difference between the wall and bulk fluid shrinks. The TES unit differs from a traditional heat exchanger in that $U$ also varies with time because of latent heat transfer. This can be described in terms of its similarity to the Stefan problem. The phase change interface moves thereby changing the heat conduction path, and, could change due to natural convection within the PCM liquid depending on the design.

Despite this key difference between the TES unit and heat exchangers, we can still use similar strategies for determining $U$. Like heat exchangers, we can predict the overall heat transfer coefficient from analytical models or experimental measurements.

## Prediction for a Simple Matrix

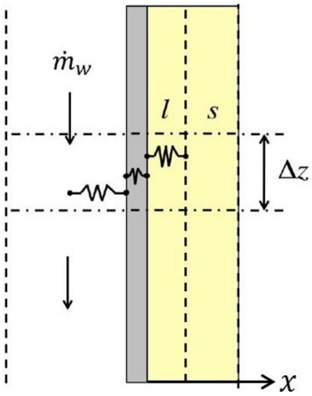

Figure 2.3: Varying thermal resistances in TES device during the extraction process.

As a first cut, we can estimate the overall heat transfer coefficient by summing and inverting thermal resistances [5].

1. calculating the hydraulic diameter, $D_h$, of the flow passage
2. determining the Reynolds number, Re [38]
3. employing the appropriate convective correlation for this flow
4. solving for the convective heat transfer coefficient, $h$
5. summing thermal resistances from the center of the flow passage through the working fluid, plate thickness, and PCM to the melting front (transient resistance) as in Figure 2.3
6. inverting this total resistance into a heat transfer coefficient
7. taking a time average of this transient result

The above prediction of $U$ from thermal resistances can be refined based on theoretical phase change analysis normal to the flow passage. For layers of PCM between rectangular channels, a Stefan-type analysis is used to analyze the variation of $U$ with time for a melting or freezing transient. We formulate and solve a classical two phase problem in a finite slab with a convective boundary condition on one end, and an adiabatic boundary condition on the other [47]. Here we assume that sensible heat transfer is minimal compared to latent heat transfer, enabling us to employ a quasi-steady approximation. The problem starts with solid at its melting temperature and a growing liquid region. We are interested in the temperature distribution in the liquid in order to determine the overall heat transfer coefficient [8]. While the following equations govern the melting process, they are equally valid for freezing by switching $T_l$ and $T_s$. The governing equations for melting are:

$$\frac{\partial^2 T_l}{\partial x^2} = \frac{\rho_e c_{pe}}{k_e}\frac{\partial T_l}{\partial t} = 0 \tag{2.1}$$

$$T_s = T_m \tag{2.2}$$

by the quasi-steady approximation outlined by Lunardini [34] with boundary conditions as follow:

$$-k_e \frac{\partial T_l}{\partial x}\bigg|_{x=0} = h(T\bigg|_{x=0} - T_\infty) \tag{2.3}$$

$$T_l\bigg|_{x=s(t)} = T_s = T_m \tag{2.4}$$

$$k_e \frac{\partial T_l}{\partial x}\bigg|_{x=s(t)} = \rho_e h_{ls}\frac{ds}{dt} \tag{2.5}$$

$$\frac{\partial T_s}{\partial x}\bigg|_{x=L} = 0 \tag{2.6}$$

and the initial condition that

$$T_l\bigg|_{t=0} = T_m \tag{2.7}$$

Solving the governing equations with these boundary and initial conditions leads to the following solution for the temperature field:

$$T_l(z,t) = \frac{T_m - T_w(z)}{\sqrt{\frac{2k_e(T_m - T_w(z))}{\rho_e h_{ls}}t + \left(\frac{k_e}{h}\right)^2}}\left(x + \frac{k_e}{h}\right) + T_w(z) \tag{2.8}$$

From here, the instantaneous heat transfer coefficient in the PCM can be found by dividing the heat flux by the temperature difference between the passage wall and melt front:

$$U_{PCM} = \frac{k_e}{\sqrt{\frac{2k_e(T_m - T_w(z))}{\rho_e h_{ls}}t + \left(\frac{k_e}{h}\right)^2} - \left(\frac{k_e}{h}\right)} \tag{2.9}$$

In Equation 2.9, $U$ is a function of both space and time. While the explicit spatial dependence is not visible, it is encapsulated in the convective heat transfer coefficient, $h$, and the working fluid temperature, $T_w$. We can use a convective correlation to determine a mean $\bar{h}$ for the heat exchanger, but $T_w$ should be treated as a spatially varying field variable.

The overall heat transfer coefficient also must incorporate the heat transfer from the flow passage center line to the passage walls. Thus, the overall heat transfer coefficient, $U$, as a function of position, $z$, and time, $t$, is given as follows:

$$U(z,t) = \frac{1}{\frac{1}{h} + \frac{\sqrt{\frac{2k_e(T_m - T_w(z))}{\rho_e h_{ls}}t + \left(\frac{k_e}{h}\right)^2} - \left(\frac{k_e}{h}\right)}{k_e}} \tag{2.10}$$

The magnitude of $U(z,t)$ depends on the contributions from convective heat transfer on the fluid side as well as conduction through the PCM environment. The mean overall heat transfer coefficient can be determined by taking an average of Equation 2.10 over time after taking into account the spatial variation of $T_w(z)$. This can be done either while solving the governing PDEs or proceeding with an average water temperature, $\bar{T_w}$, substituted for $T_w(z)$.

$$\bar{U} = \frac{\int_0^t U(t')dt'}{t} \tag{2.11}$$

The above procedure simplifies the problem by proceeding with a time-averaged overall heat transfer coefficient that encapsulates the changing position of the solid-liquid interface. These idealizations lead to a conservative estimate for $\bar{U}(\bar{T_w})$ as seen in Figure 2.4. Here, $\bar{U}$ represents an average value for extraction and charging corresponding to the TES heat exchanger geometry specified in Table 2.3.

If we allow $U$ to change to account for the explicit time dependence as well as changing working fluid temperature along the flow passage, $N_{tu}$ will vary in the computational model predicting device effectiveness as in Figure 2.4. This has been incorporated in order to assess the importance of capturing $U(z,t)$ in the solution of the partial differential equations.

Results in Table 2.1 show that $\bar{U}$ is always within 99 % of the instantaneous $U$. We are interested in knowing how different $\bar{U}$ values impact device performance. From Table 2.2, we see that the variation of $\bar{U}$ within 99 % makes $\sim$ 5 % difference in $\varepsilon_{tes}$ (at the lower end) and, thus, the use of the method outlined above for determining $\bar{U}$ is adequate moving forward. That said, more accurate means of determining an average $U$ for more realistic scenarios are needed. This will be developed further in subsequent iterations.

Table 2.1: Comparison of $U$ extrema and average values from results shown in Figure 2.4.

| | | | % Difference |
|---|---|---|---|
| $U_{ext,min}$ | & | $U_{ext,max}$ | 144 |
| $U_{ext,max}$ | & | $\bar{U}(\bar{T_w})$ | 86 |
| $U_{ext,min}$ | & | $\bar{U}(\bar{T_w})$ | 85 |
| $U_{char,min}$ | & | $U_{char,max}$ | 143 |
| $U_{char,max}$ | & | $\bar{U}(\bar{T_w})$ | 99 |
| $U_{char,min}$ | & | $\bar{U}(\bar{T_w})$ | 68 |

Table 2.2: $U$ variation on predicted device performance during extraction and charging.

| | $\bar{U}$ $\left[\frac{\mathrm{W}}{\mathrm{m^2K}}\right]$ | $\varepsilon_{tes,ext}$ | $\varepsilon_{tes,char}$ |
|---|---|---|---|
| 99% higher | 580.00 | .80 | .80 |
| Baseline $\bar{U}(\bar{T_w})$ | 195.92 | .80 | .80 |
| 99% lower | 66.18 | .79 | .76 |

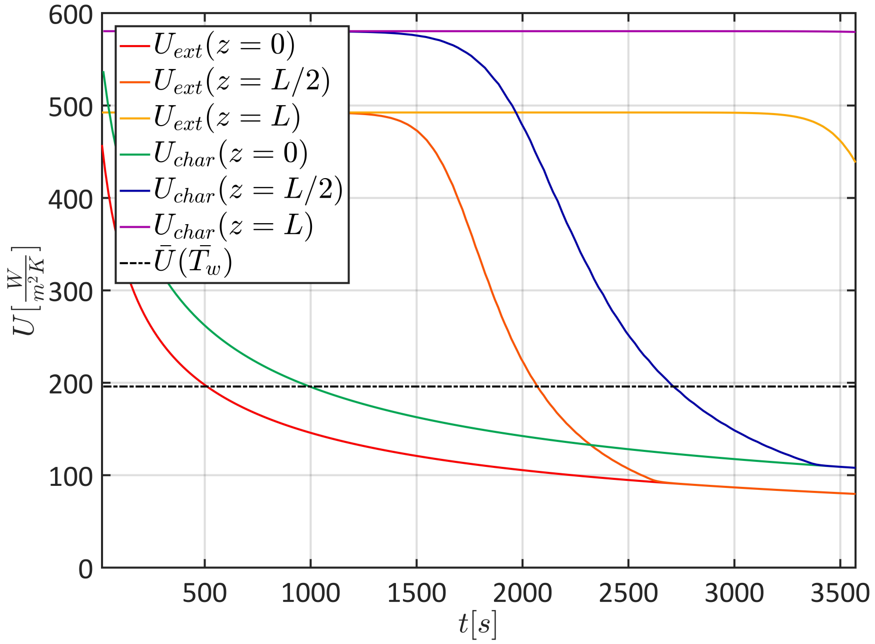

Figure 2.4: Prediction of spatial and temporal variation of $U$ during extraction and charging.

## 2.3 Case Study Example

To provide concreteness, the framework for determining the overall heat transfer coefficient is used to specify a $U$ that can be input into effectiveness modeling of the thermal energy storage and predict device performance. In order to delve into a detailed analysis of the TES unit, operating conditions for the device must first be specified. We prescribe a target effectiveness for the TES as well as desired times for operation. We assume that the extraction process, removing heat from the working fluid and melting the PCM, would occur during a 1 hour period. For our preliminary study, we consider the extraction process begins with the TES completely frozen. The initial temperature of the PCM during extraction, $T_{0,e}$, is assumed to be subcooled below its melting temperature.

We assume that the charging process of refreezing the PCM would occur during a 1 hour period directly following extraction. The initial temperature of the PCM during charging, $T_{0,c}$, is assumed to be equal to the final temperature distribution after extraction $T_{f,e}(z)$. This distribution exists because the working fluid and element temperature vary along the flow passage as heat is transferred between the working fluid and the PCM. Only where latent heat transfer is taking place can we expect the element temperature to be $T_m$. However, during the extraction process, the PCM near the inlet undergoes and completes phase change more quickly than the PCM further downstream. After complete melting, this PCM near the inlet still accepts heat in the form of sensible heat transfer raising its temperature. When the extraction process stops, this distribution remains and there is not enough time for axial conduction to occur along the passage in order to equalize temperature. Thus, $T_{0,c}$ is a function of the axial coordinate, $z$, as reflected in Table 2.3. The working fluid inlet temperatures for extraction and charging must also be defined. These temperatures are the boundary conditions for the TES device. These selected baseline conditions are enumerated in Table 2.3.

For this case study, the thermal storage device is assumed to be a plate-fin heat exchanger with alternating layers of phase change material and rectangular working fluid flow passages on the liquid side. We selected our working fluid and phase change material to achieve specific goals. A 50/50 mixture of ethylene glycol and water is ideal in this system because of its applicability in a wide range of operating temperatures. This working fluid has also been combined with anti-corrosion agents for many years to reduce fouling in heat exchangers. Lithium nitrate trihydrate (LNT) is an ideal candidate for phase change material due to its high energy density. This phase change material also has desirable thermal conductivity and cost. Furthermore, it is chemically non-reactive and stable. The melting temperature of the PCM was taken to be 30°C, which is possible with a specific variation of lithium nitrate trihydrate [42].

For the operating conditions detailed herein, the overall heat transfer coefficient, $U$, in Table 2.3 represents a target case study design of a TES unit based on analytical determinations of $U$ from the previous section. These $U$ values were calculated by following the Stefan type analysis in which the time-dependent nature of the total thermal resistance is captured before being averaged over time for a mean value.

Table 2.3: Input parameters for thermal storage performance calculations with a constant boundary condition.

Device Geometry

| | | |
|---|---|---|
| Working fluid channel height, $H_{wf}$ | 1.9 | mm |
| PCM storage matrix section height, $H_{pcm}$ | 4.7 | mm |
| Channel width, $W$ | 76.2 | mm |
| Channel length, $L$ | 203.2 | mm |
| Thickness of the metal wall and fins, $t_m$ | 0.2 | mm |

Material Properties

| | | |
|---|---|---|
| Density of working fluid, $\rho_w$ | 1050 | kg/m$^3$ |
| Specific heat of working fluid, $c_{p,w}$ | 3308 | J/kgK |
| Dynamic viscosity of working fluid, $\mu_w$ | 0.003 | Ns/m$^2$ |
| Thermal conductivity of working fluid, $k_w$ | 0.434 | W/mK |
| Prandtl number of working fluid, Pr | 22.378 | |
| Density of PCM storage matrix, $\rho_s$ | 1425 | kg/m$^3$ |
| Specific heat of PCM storage matrix, $c_{p,s}$ | 2245 | J/kgK |
| Thermal conductivity of PCM storage matrix, $k_s$ | 0.58 | W/mK |
| Latent heat of fusion of PCM, $h_{ls}$ | 278.14 | kJ/kg |
| PCM melt temperature, $T_m$ | 30 | °C |

Operating Conditions

| | | |
|---|---|---|
| Initial system temperature for extraction, $T_{0,e}$ | 28 | °C |
| Initial system temperature for charging, $T_{0,c}$ | $f(z)$ | °C |
| Working fluid inlet temperature for extraction, $T_{wi,e}$ | 37.4 | °C |
| Working fluid inlet temperature for charging, $T_{wi,c}$ | 26.0 | °C |
| Working fluid mass flow rate for extraction, $\dot{m}_e$ | 1.124 | g/s |
| Working fluid mass flow rate for charging, $\dot{m}_c$ | 1.607 | g/s |
| Overall heat transfer coefficient for extraction, $\bar{U}_e$ | 418 | W/m$^2$K |
| Overall heat transfer coefficient for charging, $\bar{U}_c$ | 367 | W/m$^2$K |

System Performance

| | | |
|---|---|---|
| Storage effectiveness, $\varepsilon_{tes}$ | .85 | |
| TES energy, $E_{tot}$ | 50 | kJ |
| Extraction time, $t_e$ | 3600 | s |
| Charging time, $t_c$ | 3600 | s |

The effectiveness-NTU model analysis predicts that for the high effectiveness designs of interest here, $N_{tu}$ is large ($\sim 30$), and the predicted effectiveness of charging and extraction processes are only weakly affected by changes in $U$. In addition to predicting the performance, the effectiveness-NTU model can also predict the sensitivity of the performance to the accuracy of the $U$ value, and this analysis provides a useful basis for evaluating the appropriateness of methods for determining the value of $U$ used for design analysis.

Table 2.4: Dimensionless input values for thermal storage performance calculations.

| | $N_{tu}$ | $R_{we}$ | $\mathrm{St}_{io}$ | $t^*$ |
|---|---|---|---|---|
| Extraction | 30.80 | 0.38 | 0.16 | 37.57 |
| Charging | 24.56 | 0.38 | 0.16 | 53.72 |

The dimensional parameters listed above are used to calculate the dimensionless variables in Table 2.4. Some variables, including $N_{tu}$, differ for the extraction and charging processes because the mass flow rate and overall heat transfer coefficient differ. Others, such as $R_{we}$ and $St_{io}$ remain consistent. If the dimensionless variables are changed, the simulation will naturally lead to different results.

## Extraction / Melting

During cold extraction, heat is delivered to initially frozen PCM in the storage device. The operation time and mass flow rate through the channel are chosen to give rise to dimensionless parameters that make it possible to achieve a prescribed TES effectiveness. The dimensionless parameter values for extraction from Table 2.4 were input into the three governing partial differential Equations 1.9, 1.10, and 1.11 to determine melt fraction and temperature throughout the element material. Computed solutions of the governing equations were generated using an explicit finite difference scheme with Forward Time and Upwind spatial finite difference representations for derivatives in the equations [26]. Reported performance calculation results are for a time step $\Delta t^*$ of 0.00025 and a spatial mesh $\Delta \hat{z}$ of 0.005. Reducing these by a factor of 5 produced less than 1% change in the computed effectiveness, indicating that the solutions are not dependent on the choices of $\Delta \hat{z}$ and $\Delta t^*$ at this threshold, or that the solution is convergent [32].

For the dimensionless parameter values listed above, the spatial variations of dimensionless working fluid and storage element temperatures, and melt fraction are shown for 3 moments in time in Figure 2.5a. As the transient proceeds, more of the storage raises in temperature towards the inlet working fluid temperature, and an increasing fraction of the PCM is melted. In the first snapshot, the dimensionless working fluid temperature, indicated by the red line, enters the TES at a hot working fluid inlet temperature. As it travels through the device, it rejects heat through the channel walls to the PCM and exits at a lower temperature. The dimensionless element temperature, indicated by the blue line, begins to increase due to interaction with the hot working fluid. The melt fraction indicated by the green line has begun its ascent from a solid towards a liquid state. At a later time, the hot working fluid has heated the element temperature up as well as almost melted the PCM to its dimensionless liquid state of 1.

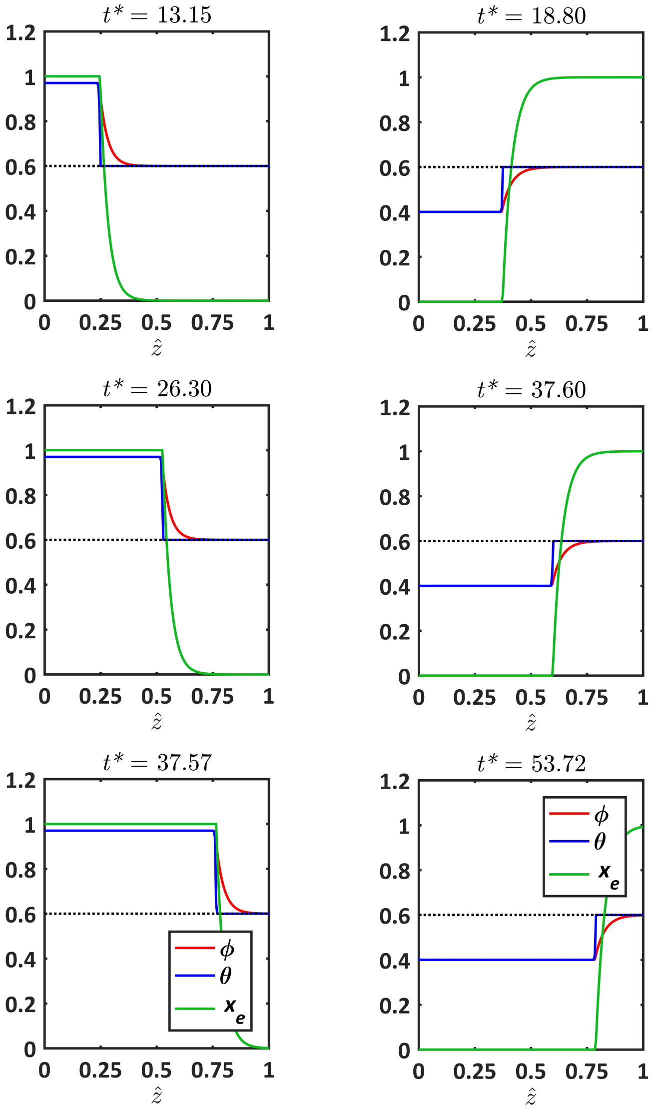

(a) Extraction process (b) Charging process

Figure 2.5: Extraction process dimensionless fluid and element temperature($\phi$, $\theta$) and melt fraction ($x_e$) profiles through space and time with a constant inlet boundary condition.

## Charging / Freezing

During the cold charging operation, the cooling working fluid loop is activated to refreeze the PCM. The set of partial differential Equations 1.9, 1.10, 1.11 are also be solved for charging the TES device. The dimensionless parameter values calculated from the baseline case for charging are listed in Table 2.4.

Figure 2.5b presents three snapshots in time of the cold storage charging process. In the first snapshot, the dimensionless working fluid temperature, indicated by the red line, enters the TES at a cold working fluid inlet temperature. As it travels through the device, it accepts heat through the channel walls from the PCM and exits at a higher temperature. The dimensionless element temperature, indicated by the blue line, begins to decrease due to the cool working fluid. The melt fraction, indicated by the green line, has begun its descent from a saturated liquid towards a solid state. At a later time, the cool working fluid has almost cooled the element temperature down to its desired temperature as well as frozen the PCM towards its dimensionless solid state of 0.

Should we wish to completely re-freeze the PCM, we have several options. The design could be changed or the operating time for the charging process could be increased. An attempt to improve the design would likely center around minimizing the size while improving heat transfer. In order to improve heat transfer, the parameters used to calculate the overall heat transfer coefficient could be adjusted. While there is a myriad of design changes that could be made, the problem can also be addressed in a simpler way: by extending the operation time of the charging process.

## Full Cycle

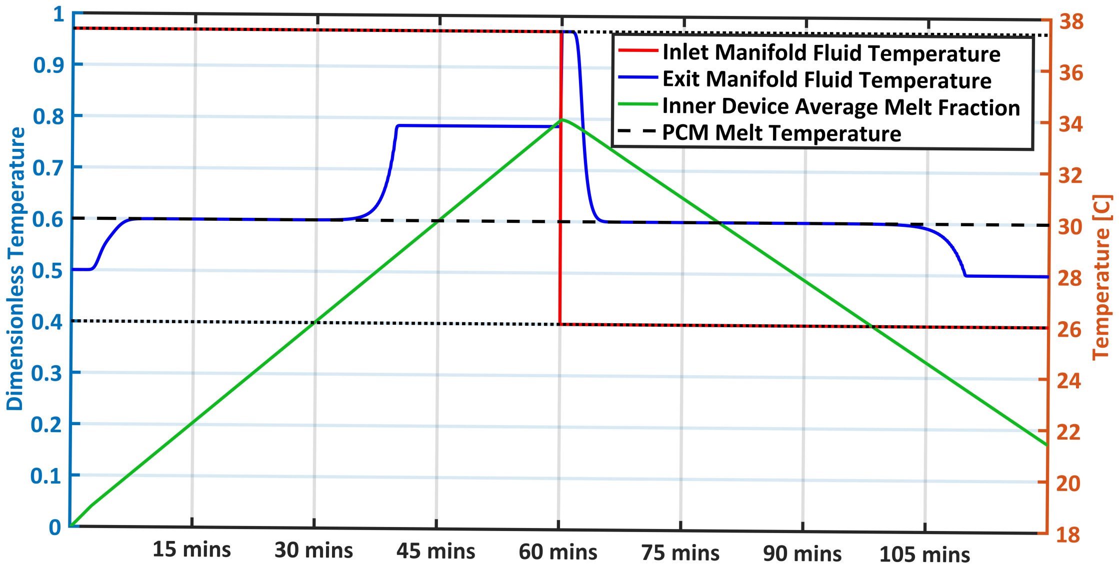

Figure 2.6: Paired extraction and charging of TES with a constant boundary condition.

Moving forward, we are able to fully take into account the cycling of the device. We can visualize the paired extraction and charging processes by looking at the entire cycle as shown in Figure 2.6.

Further cycling of the device should lead to a steady state operation with a more symmetric distribution of average melt fraction through the paired extraction and charging processes. The final charging condition will serve as the initial extraction condition and vice versa. We specify operating conditions so that the device remains in this window, melting and freezing the fraction of PCM equivalent to its effectiveness target.

## 2.4 Preliminary Discussion

The dimensionless effectiveness-NTU analysis framework developed in Chapter 1 can be a useful tool for design of thermal storage units for asynchronous cooling and other applications. However, its successful use requires accurate specification of the overall heat transfer coefficient in the storage matrix.

This investigation suggests that there are two viable approaches to determining appropriate values of the overall heat transfer coefficient. One is to accurately model conduction and convection transport in a unit cell of the matrix based on an an analogous Stefan type melting or freezing process. Another approach is to obtain performance test data for a small prototype unit and determine the overall heat transfer coefficient that yields a best match of the unit performance model with test data. This can be done by determining the performance of the device from experiment and using the numerical framework to iterate through $U$ until matching the experimental solution. As this is likely cumbersome, it seems that the most elegant solution is to improve the mathematical model for calculating $U$.

In this study, various parameters of a TES device are modeled in order to examine an effective design space. Determination of the TES overall heat transfer coefficient is central to this exploration. We determined a varying $U(z,t)$ from the Stefan problem formulation, as well as an time averaged $\bar{U}$ by assuming an average convective heat transfer coefficient, $\bar{h}$, and an average working fluid temperature, $\bar{T_w}$. Comparing these, we were able to show that even with 99 % variation in $\bar{U}$ for a highly effective TES unit, we only see slight changes in performance ($\sim$ 5 %). Thus, results demonstrate that use of $\bar{U}$ in the effectiveness model can provide a useful basis for design, but more accurate means of determining $U$ are needed.

## 2.5 Improving Variable Conductance Model

To do so, we can modify the calculation for overall heat transfer coefficient, $U$, to better account for the change in melt front location. The variable $U$ approach discussed in this chapter thus far relates $U$ to the heat transfer rate, $q$, although we could directly determine $U$ from a re-framed resistor network analogy. The remainder of this chapter aims to provide a method for determining the effects of variable conductance during a phase change process that is ultimately simpler and more readily applied than the similar methods developed elsewhere [22, 48, 31].

## 2.6 Computational Methodologies

### Variable $U$ PDE Solver

In the partial differential equation (PDE) model developed in Chapter 1, the temperature of the unit cell is tracked as an average. In addition, the melt front is not explicitly tracked. Rather, the overall melt fraction of the unit cell is calculated. One can, however, determine the melt front location from the melt fraction and the dimension $L_{pcm,max}$, shown in Figure 2.1.

In defining $N_{tu}$ in Chapter 1, we originally considered a constant value for $U$. Thus far in Chapter 2, we investigated a variable treatment of $U$, accounting for effects of the changing location of the melt front on the heat transfer performance of the system as in Table 2.2. We can build upon the latter by using a more simplified approach to the calculation for $N_{tu}$ via a resistor network analogy to account for the change in melt fraction in the unit cell.

The following will focus on the melting process, and thus utilize the initial conditions corresponding to completely frozen PCM. Note that this scheme is forward in time and the only parameter that propagates information in $\hat{z}$ is dimensionless working fluid temperature $\phi$.

Moving forward, we will refine our calculation for $N_{tu}$ as a function of the position of the melt front in a unit cell due to changes in $U$.

### New Method: Unit Cell Phase Change as a Resistor Network

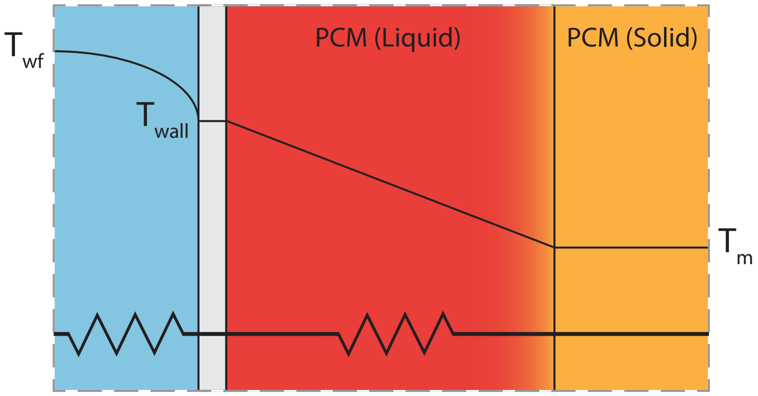

Figure 2.7: Resistance network consisting of thermal resistors in the working fluid and PCM sections where temperature variation, indicated above, drives heat transfer from the flow centerline to the PCM adiabat.

We can use a resistor network analogy, as shown in Fig. 2.7, to capture the effects of a changing melt front location on the heat transfer of the system. Assuming the system is quasi-steady during the phase change process (which is reasonable if $\mathrm{St}_{io} \ll 1$), the heat transfer can be described by:

$$h_{pcm} A_{wall,pcm}(T_{wall} - T_m) = h_{wf} A_{wall,wf}(T_{wf} - T_{wall}) \tag{2.12}$$

To help illustrate the geometry terms, see Fig. 2.8, which provides an example using a round tube geometry for the working fluid to pass through the PCM. The inner wall of the tube, which contacts the working fluid, has surface area $A_{wall,wf}$, while the outer wall, which contacts PCM, has surface area $A_{wall,pcm}$.

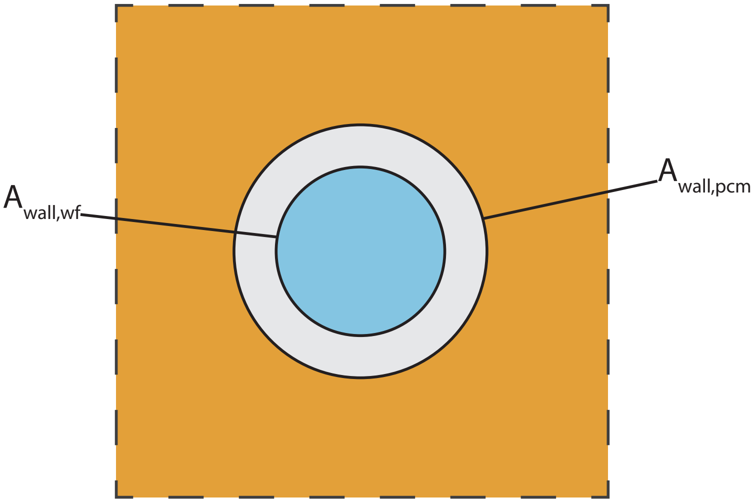

Figure 2.8: Example of round flow channel geometry surrounded by PCM (orange in figure), with flow into or out of page. Here, the wall areas are different.

In Eq. 2.12, $h_{pcm}$ refers to the heat transfer coefficient for the process of transferring heat from the surface defining $A_{wall,pcm}$ to the PCM melt front. Neglecting radiation and natural convection, $h_{pcm} = \frac{k_{pcm}}{x_e L_{pcm,max}}$; in other words, $h_{pcm}$ consists only of a conductive term. Replacing $h_{pcm}$ in Eq. 2.12 and solving for a ratio of temperatures gives:

$$\frac{T_{wall} - T_m}{T_{wf} - T_{wall}} = \frac{h_{wf} L_{pcm,max}}{k_{pcm}} \frac{A_{wall,wf}}{A_{wall,pcm}} x_e \tag{2.13}$$

The overall heat transfer coefficient for such a system is related to the inverse of the sum of thermal resistances:

$$UA = \left[\frac{1}{h_{wf} A_{wall,wf}} + \frac{L_{pcm,max}}{k_{pcm} A_{wall,pcm}} x_e\right]^{-1} \tag{2.14}$$

This can be related to the number of transfer units $N_{tu}$ via the equation $N_{tu} = \frac{UA}{C_{min}}$. Thus:

$$N_{tu} = \frac{h_{wf} A_{wall,wf}}{\dot{m}_w c_{p,w}} \left[ 1 + \frac{h_{wf} L_{pcm,max}}{k_{pcm}} \frac{A_{wall,wf}}{A_{wall,pcm}} x_e \right]^{-1} \tag{2.15}$$

This expression can be more succinctly written with the definition of $N_{tu}$ for the working fluid side and the Biot number $\mathrm{Bi}_{pcm}$ for the PCM side:

$$N_{tu,wf} = \frac{h_{wf} A_{wall,wf}}{\dot{m}_w c_{p,w}} \, , \quad \mathrm{Bi}_{pcm} = \frac{h_{wf} L_{pcm,max}}{k_{pcm}} \tag{2.16}$$

Substituting the above expressions into Eq. 2.15 results in:

$$N_{tu} = N_{tu,wf} \left[ 1 + \mathrm{Bi}_{pcm} \frac{A_{wall,wf}}{A_{wall,pcm}} x_e \right]^{-1} \tag{2.17}$$

For the purposes of varying parameters more easily in the results section, the following coefficient may be defined:

$$Z_{coef} = \mathrm{Bi}_{pcm} \frac{A_{wall,wf}}{A_{wall,pcm}} \tag{2.18}$$

The end result is therefore:

$$N_{tu} = N_{tu,wf} \left[ 1 + Z_{coef} x_e \right]^{-1} \tag{2.19}$$

In order to calculate a value for an "average" $N_{tu}$ approach, the value of $x_e$ is simply set to 0.5 which is representative of an average melt fraction:

$$\overline{N_{tu}} = N_{tu,wf} \left[ 1 + \frac{Z_{coef}}{2} \right]^{-1} \tag{2.20}$$

Equations 2.19 and 2.20 define the primary schemes to be discussed in this paper. Referred to as the "variable $N_{tu}$ method" and "average $N_{tu}$ method," respectively, these methods need to first be validated against established literature before being applied to a TES device. Thus, additional modeling techniques for a unit cell of PCM will be introduced.

## Forward-Time Central-Space Method

An additional numerical method to track the location of a one-dimensional melting problem was developed and used to compare against the results of the variable $N_{tu}$ method for a single unit cell, such that $T_{wf}$ is constant. This approach employs a Forward-Time Central-Space (FTCS) scheme, shown in Figure 2.9, to discretize the unit cell and solve for temperature and melt fraction throughout, rather than lumping melt fraction and temperature into average values per each unit cell as in the variable and average $N_{tu}$ methods.

Defining the direction of melt front propagation through the unit cell as $y$, sensible energy storage occurs when a cell of PCM at position $i\Delta y$ and time $n\Delta t$ is not at its melt temperature, and thus the temperature at the next time step can be found via:

$$T_i^{n+1} = T_i^n + \Delta t \frac{k_{pcm}}{\rho_{pcm} c_{p,pcm}} \frac{T_{i-1}^n - 2T_i^n + T_{i+1}^n}{\Delta y^2} \tag{2.21}$$

$$\text{for } x_{e_i}^n = 0 \text{ or } x_{e_i}^n = 1$$

If Eq. 2.21 would result in the temperature at the next time step $n+1$ to pass the melt temperature, then $T_i^{n+1}$ is set to $T_m$ and latent energy storage begins, as given by:

$$x_{e_i}^{n+1} = x_{e_i}^n + \Delta t \frac{k_{pcm}}{\rho_{pcm} h_{ls}} \frac{T_{i-1}^n - 2T_i^n + T_{i+1}^n}{\Delta y^2} \tag{2.22}$$

$$\text{for } T_i^n = T_m \text{ and } 0 < x_{e_i}^n < 1$$

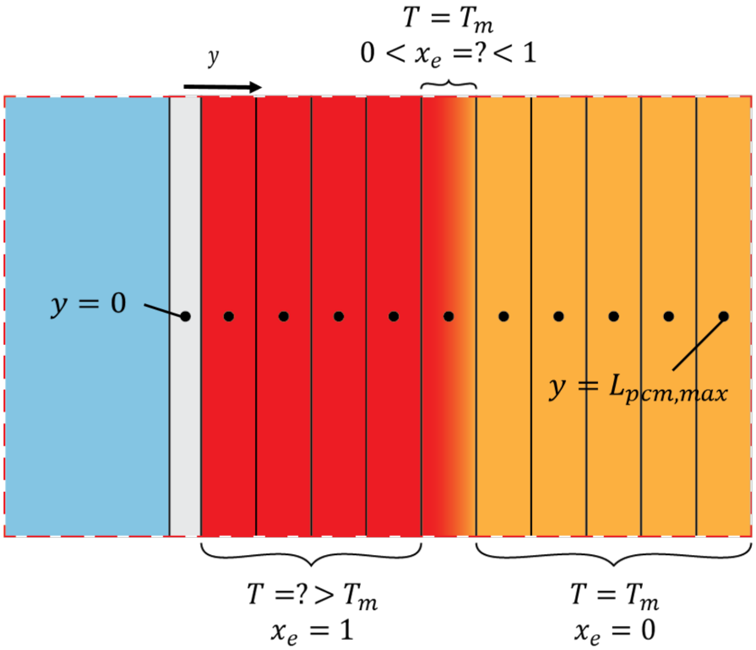

Figure 2.9: Forward Time Central Space method applied to TES unit cell.

For the purposes of comparison to the variable and average $N_{tu}$ methods, a convective boundary condition is used at one end. The other end emulates a semi-infinite condition by setting the length of PCM ($L_{pcm,max}$) such that the melt front location $S < L_{pcm,max}$ for the simulation time considered and enforcing an adiabatic boundary condition at $y = L_{pcm,max}$. Therefore, the boundary conditions are established via:

$$\text{At } \ y = 0: \ \ T_{i=1}^{n+1} = \frac{\frac{k_{pcm}}{h_{wf}\Delta y} T_{i=2}^{n+1} + T_{wf}}{1 + \frac{k_{pcm}}{h_{wf}\Delta y}}$$

$$\text{At } \ y = L_{pcm,max}: \ \ \frac{T_I^{n+1} - T_{I-1}^{n+1}}{\Delta y} = 0 \tag{2.23}$$

where $I$ is the node at $y = L_{pcm,max}$; that is, $I = \frac{L_{pcm,max}}{\Delta y} + 1$.

It is important to note several shortcomings of this method. This method discretizes the PCM as a series of small volumes. When a particular cell of PCM at $i\Delta y$ is changing phase, its temperature is assumed to remain at $T_m$, which will cause a stair step-like appearance in temperature for the cells $0 \leq y < (i-1)\Delta y$.

Additionally, the heat equation is stiff, meaning that certain numerical methods, the FTCS scheme included, are numerically unstable if their step sizes are not carefully selected. For Equation 2.21 to give accurate results, the time step and spatial step must satisfy:

$$\frac{k_{pcm}}{\rho_{pcm} c_{p,pcm}} \frac{\Delta t}{\Delta y^2} \leq \frac{1}{2} \tag{2.24}$$

This is handled here by using a very small time step to solve the equations. One could opt to use the implicit Crank-Nicolson method instead to avoid the risk of instability. This would become especially relevant for computationally intensive problems with large spatial domains and long time scales.

## Methods from Literature

## Stefan Solution: Convective Boundary Condition

As was the case with comparing to the FTCS method, in order to compare the numerical solver to other papers and texts, focus will be on the analysis of a single unit cell of PCM, located at the inlet, such that $T_{wf}$ is a constant, consistent with the inlet boundary condition.

The logic behind the analysis provided in the derivation of the variable $N_{tu}$ method is very similar to that of a simplified Stefan problem, employing a quasi-steady approximation. Such an approximation is valid if the Stefan number for a material undergoing phase change is very low and allows the temperature profile between the wall and the melt front to be approximated as linear. The Stefan condition, which relates the motion of the melt front to a heat flux discontinuity at the liquid–solid interface, can be expressed as:

$$h_{ls} \rho_{pcm} \frac{dS}{dt} = -k_{pcm} \left( \frac{dT}{dy} \right)_S \tag{2.25}$$

Lock et al. provide an analysis for such a Stefan problem [33]. For the case of a melting problem where the solid phase temperature is $T_m$ throughout, as is the assumption for the

Table 2.5: Summary of methodologies used to predict temperature and melt fraction fields.

Numerical Schemes

| **Scheme Description** | **Abbreviated Name** | **Reference** |
|---|---|---|
| PDE Solver, Variable $U$ Approach | Variable $N_{tu}$ Method | Equation 2.15 |
| PDE Solver, Average $U$ Approach | Average $N_{tu}$ Method | Equation 2.20 |
| Finite Difference in Space and Time | FTCS Method | Equations 2.21-2.22 |

Analytical Schemes

| **Scheme Description** | **Abbreviated Name** | **Reference** |
|---|---|---|
| Stefan Solution, Convective Boundary Condition | Stef. Sol., Convection BC | Equation 2.27 |
| Stefan Solution, Prescribed Wall Temperature | Stef. Sol., Wall Temp. BC | Equation 2.28 |

variable and average $N_{tu}$ methods, the authors present the following relation between time and melt front location with a convective boundary condition at the bounding plane:

$$t = \frac{h_{ls}\rho_{pcm}}{2k_{pcm}(T_{wf} - T_m)}\left[S^2 + \frac{2k_{pcm}S}{h_{wf}}\right] \tag{2.26}$$

This expression can be rearranged to determine the melt front location as a function of time:

$$S = \left[\left(\frac{k_{pcm}}{h_{wf}}\right)^2 + \frac{2k_{pcm}(T_{wf} - T_m)}{\rho_{pcm}h_{ls}}t\right]^{1/2} - \frac{k_{pcm}}{h_{wf}} \tag{2.27}$$

Note that for a finite domain, such as the unit cell considered in the paper previously with PCM length $L_{pcm,max}$, the melt front location is equal to $x_e L_{pcm,max}$.

## Stefan Solution: Specified Wall Temperature Boundary Condition

Additionally, one can consider the case of a constant wall temperature at the bounding plane, which is equivalent to $h_{wf} \to \infty$, in which case Eq. 2.27 becomes:

$$S = \sqrt{2\mathrm{St}\alpha_{pcm}t} \tag{2.28}$$

This is in direct agreement with the case of the semi-infinite, quasi-steady Stefan problem with a prescribed wall temperature, as described by Lunardini [34].

The preceding illustrates a simplified approach to solving the Stefan problem for a semi-infinite, one-dimensional section of PCM with a quasi-steady approximation. If the temperature profile is not assumed linear, or generally unknown, the Stefan problem becomes considerably more complicated. There are several approximations that are well-documented but will not be discussed here [34, 35].

### Summary of Computational Methodologies

While the primary focus of this paper is on the partial differential equations outlined in the Variable $U$ PDE Solver section, several other schemes were outlined in this paper and will be used to validate the new model. To clarify the language in the remainder of this paper, Tab. 2.5 describes the abbreviated names of all methods introduced.

## 2.7 Implementation and Results

### System Inputs and Properties

The present paper focuses on the melting process, such that the system begins at the melt temperature with the PCM completely solid ($x_e = 0$). Hot working fluid enters the flow channel, which passes through banks of PCM, melting and superheating the PCM.

The solver is run using values based on information provided for a generic TES device. The PCM used in the system is lithium nitrate trihydrate. The TES device itself is constructed from aluminum 5056. The properties for these materials were volume averaged and the effective properties are listed in Tab. 2.6. Table 2.6 also presents information for the other input parameters, such as the temperature bounds and properties for the working fluid, a 50% mixture of ethylene glycol and water.

An axial view of the TES device considered is provided in Fig. 2.10. The width and height of the flow channels and PCM cavities are drawn to scale. Note, however, that the aluminum TES device frame is not drawn to scale. This geometry helps simplify the analysis greatly as its symmetry allows for only a single channel to be considered to characterize performance. The mass flow rate of the working fluid is simply scaled based on the number of channels in the device. This does not account for the slight differences encountered in the top and bottom due to outer working fluid channels interacting with only one slab of PCM. In addition, computations for each cell follow a simple, one-dimensional calculation. And, because the channels are rectangular, $A_{wall,wf} = A_{wall,pcm}$, helping simplify Eq. 2.15.

### Validation of Numerical Models

In order to check the accuracy of the variable and average $N_{tu}$ methods, the parameters established in Tab. 2.6 were applied to a single unit cell. The results were then compared with the auxiliary methods discussed in the FTCS Method section and the methods from literature. To quantify the agreement between methods, Eq. 2.29 will be used to determine "percent deviation." This equation gives a result ranging from 0 (perfect agreement) to 200 (poor agreement) and is valid for comparing two positive values.

$$d_r = 2\frac{|n_1 - n_2|}{n_1 + n_2}100 \tag{2.29}$$

Table 2.6: Input parameters for thermal storage performance calculations for $N_{tu}$ methods comparison.

Device Geometry

| | | |
|---|---|---|
| Channel length, $L$ | 417 | mm |
| PCM storage matrix section height, $H_{pcm}$ | 6.35 | mm |
| Working fluid channel height, $H_{wf}$ | 1.91 | mm |
| Number of working fluid channels, $N_{wf}$ | 5 | |
| Number of PCM storage matrix sections, $N_{pcm}$ | 4 | |

Material Properties

| | | |
|---|---|---|
| Specific heat of PCM storage matrix, $c_{p,pcm}$ | 1559 | J/kg K |
| Density of PCM storage matrix, $\rho_{pcm}$ | 1679 | $\mathrm{kg/m^3}$ |
| Thermal conductivity of PCM storage matrix, $k_{pcm}$ | 0.814 | W/m K |
| Latent heat of fusion of PCM, $h_{ls}$ | 278.14 | kJ/kg |
| Specific heat of working fluid, $c_{p,w}$ | 3308 | J/kg K |
| Density of working fluid $\rho_w$ | 1050 | $\mathrm{kg/m^3}$ |
| Thermal conductivity of working fluid, $k_w$ | 0.434 | W/m K |
| Dynamic viscosity of working fluid, $\mu_w$ | 2.936e−6 | $\mathrm{N\,s/m^2}$ |
| Prandtl number of working fluid, Pr | 22.4 | |

Operating Conditions

| | | |
|---|---|---|
| Working fluid inlet temperature, $T_{wi}$ | 37.4 | °C |
| PCM melt temperature, $T_m$ | 30.0 | °C |
| Initial system temperature, $T_0$ | 30.0 | °C |
| High system temperature, $T_{high}$ | 37.4 | °C |
| Low system temperature, $T_{low}$ | 30.0 | °C |

System Performance

| | | |
|---|---|---|
| Total volumetric flow rate $\dot{V}_{tot}$ | 1.07 | mL/s |
| Convective heat transfer coefficient, $h_{wf}$ | 525 | $\mathrm{W/m^2\,K}$ |

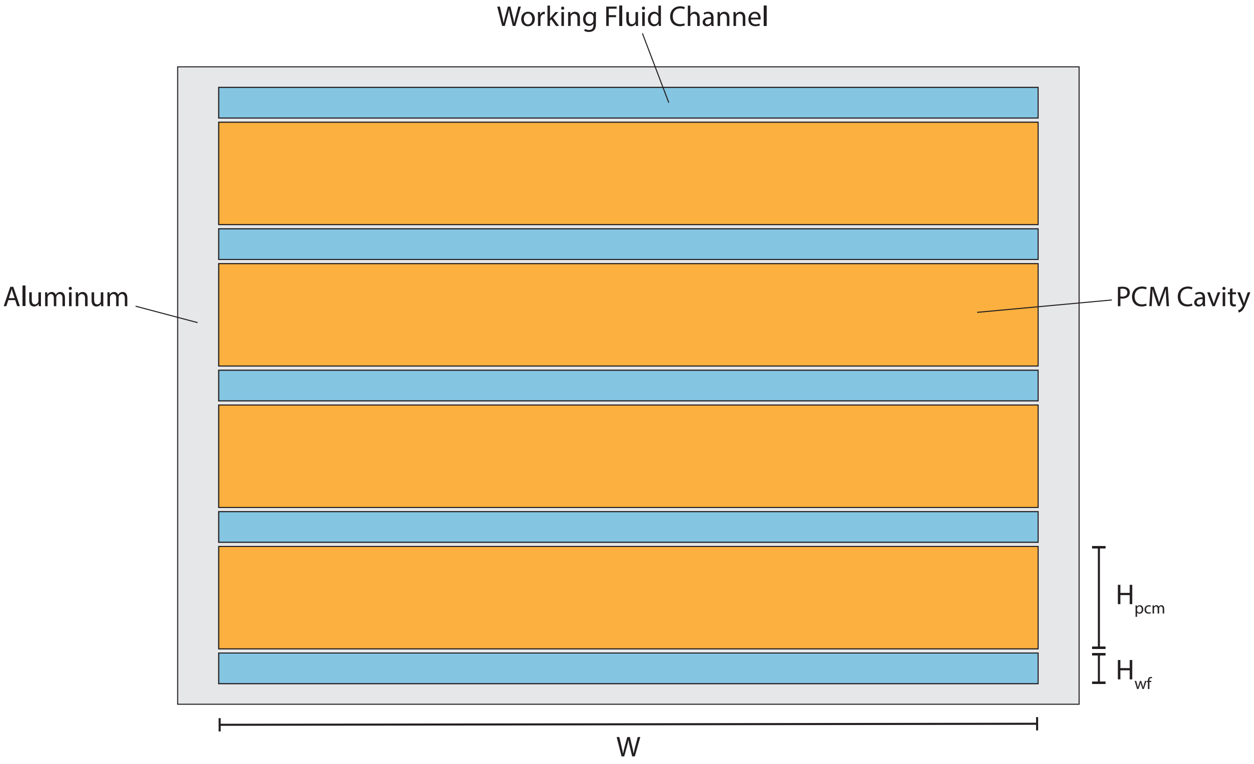

Figure 2.10: Axial view of thermal storage device consisting of working fluid flow channels and PCM storage matrix sections with relevant dimensions labeled.

## Comparison with FTCS Method

To help validate the FTCS scheme as a reasonable benchmark, the results of the simulation were compared with the solution provided in Eq. 2.28 for the Stefan solution with a prescribed wall temperature. Because this solution applies to a prescribed wall temperature boundary condition, the convective heat transfer coefficient in the FTCS model was set to $10^{10}$ W/m$^2$ K, effectively infinity. Figure 2.11 shows very good agreement between the FTCS method and the explicit Stefan solution with a prescribed wall temperature. The percent deviation between the two methods peaks at about 5% and decreases towards 1% as $t$ increases, despite increasing absolute difference between the FTCS method and Stefan solution.

With the FTCS method shown to be in good agreement with Eq. 2.28, the former was then compared with the variable $N_{tu}$ method. For the purposes of implementing a comparison between these methods, the focus of this paper will now shift to a more detailed analysis involving the overall heat transfer coefficient, $U$, used to define Eq. 2.15 and how it relates to the melt fraction. As a reminder, for the case considered in this paper, $A_{wall,wf} = A_{wall,pcm} = A$, and so Eq. 2.14 becomes:

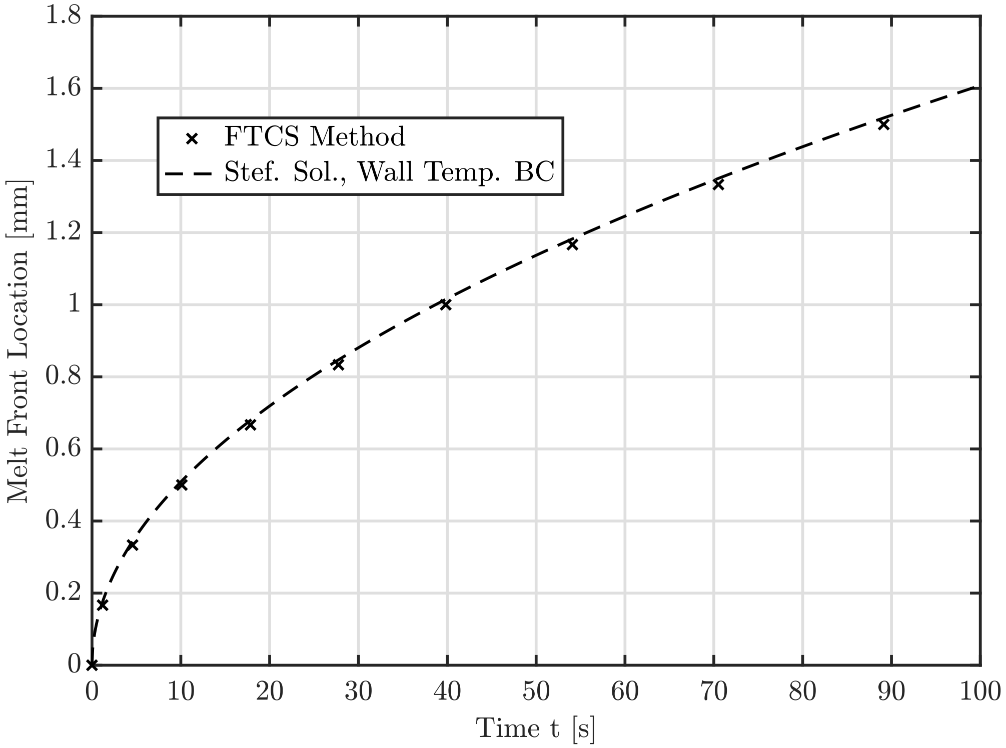

Figure 2.11: Melt front propagation as predicted by the Forward-Time Central-Space finite difference scheme and the Stefan solution for a semi-infinite medium, assuming quasi-steady conditions and a prescribed wall temperature at the bounding plane.

$$U = \left[\frac{1}{h_{wf}} + \frac{L_{pcm,max}}{k_{pcm}} x_e\right]^{-1} \tag{2.30}$$

A dimensionless form of Eq. 2.30 can be defined as $U^* = \frac{UL_{pcm,max}}{k_{pcm}}$, resulting in:

$$U^* = \left[\frac{k_{pcm}}{h_{wf} L_{pcm,max}} + x_e\right]^{-1} \tag{2.31}$$

The overall heat transfer coefficient can be computed from the results from the FTCS scheme. This is achieved by defining the heat flux as the heat at the wall, $q'' = h(T_{wf} - T_{wall})$, and relating it to the general definition of overall heat transfer coefficient, $q'' = U(T_{wf} - T_m)$, and solving for $U$. The FTCS scheme was run using the same input values described in Tab. 2.6. Due to memory constraints, this scheme was simulated for 100 seconds. The results are plotted in Fig. 2.12 and show extremely close agreement, with a peak percent deviation of about 0.011%.

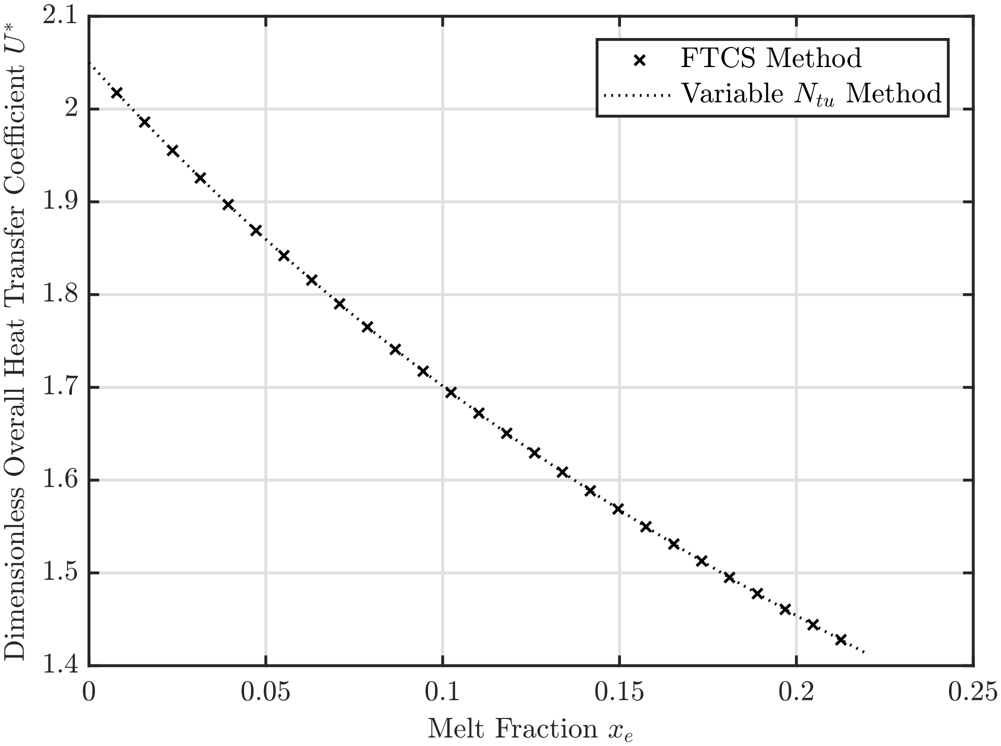

Figure 2.12: Comparison of the dimensionless overall heat transfer coefficient as the melt front propagates through a PCM unit cell calculated via the FTCS method and the variable $N_{tu}$ method.

## Application to a TES Device

The validation has shown that the variable and average $N_{tu}$ schemes are in good agreement with other available methods for a single unit cell of PCM. They will now be applied to a series of unit cells to simulate a TES device channel, such that the water temperature $\phi$ will be changing in $\hat{z}$. The dimensionless parameters $N_{tu,wf}$, $R_{we}$, $\mathrm{St}_{io}$, and $Z_{coef}$ will also be varied to demonstrate the sensitivity of the schemes to these inputs. These values are summarized in Tab. 2.7. The "baseline" case uses the inputs outlined in Tab. 2.6 to calculate the dimensionless parameters. To quantify the agreement between the two methods, three forms of interpreting deviation will be used. Equation 2.29 will be applied to both the overall effectiveness of the TES device for the runtime considered as well as each local point along the flow channel at each time step. The former provides a gauge of overall agreement between the numerical model at a system level, while the latter provides insight on the relative accuracy of the variable and average $N_{tu}$ methods at discrete points. Additionally, Eq. 2.32 will be used to calculate the root-mean-square (RMS) error, accounting for the entire set of points in space and time to check the global discrepancy. It has been converted to a percentage for ease of comparison with the percent deviation method.

$$RMS_e = 100\left[\frac{\sum_{i=1}^{n}(x_{e,var_i} - x_{e,avg_i})^2}{n}\right]^{1/2} \tag{2.32}$$

Table 2.7: Dimensionless input values for thermal storage performance calculations.

| | $N_{tu,wf}$ | $R_{we}$ | $\mathrm{St}_{io}$ | $Z_{coef}$ |
|---|---|---|---|---|
| Baseline | 26.42 | 0.393 | 0.114 | 2.051 |
| Double $N_{tu,wf}$ | 52.84 | 0.393 | 0.114 | 2.051 |
| Half $N_{tu,wf}$ | 13.21 | 0.393 | 0.114 | 2.051 |
| Double $R_{we}$ | 26.42 | 0.785 | 0.114 | 2.051 |
| Half $R_{we}$ | 26.42 | 0.196 | 0.114 | 2.051 |
| Double $\mathrm{St}_{io}$ | 26.42 | 0.393 | 0.228 | 2.051 |
| Half $\mathrm{St}_{io}$ | 26.42 | 0.393 | 0.057 | 2.051 |
| Double $Z_{coef}$ | 26.42 | 0.393 | 0.114 | 4.103 |
| Half $Z_{coef}$ | 26.42 | 0.393 | 0.114 | 1.026 |

## Process Description and Results for Baseline Case

The target effectiveness of the TES device was specified as $\overline{x_e} = 0.900$, meaning that 90.0% of the PCM in the entire device has changed phase. In order to compare the variable and average $N_{tu}$ methods, the following process is used:

1. The variable $N_{tu}$ method is run until the target effectiveness is achieved, ensuring $\overline{x_{e,var}} = 0.900$ for all cases.
2. The results of the variable $N_{tu}$ method are stored, including the corresponding runtime $t^*$.
3. The average $N_{tu}$ method is run until time $t^*$.
4. The results of the average $N_{tu}$ method are stored, including the corresponding effectiveness $\overline{x_{e,avg}}$.

Thus the overall effectiveness of the variable and average $N_{tu}$ method is compared for a value of $t^*$ that ensures an effectiveness of 0.900 in the variable $N_{tu}$ case.

For the baseline case, with a simulation runtime of $t^* = 57.5$, the average $N_{tu}$ method generated an overall effectiveness of 0.895, for a percent deviation of 0.574% compared to the variable $N_{tu}$ method. Considering the overall performance of the system, both methods are in very good agreement. However, there is still some discrepancy in local values. To help compare the results, the local melt fraction of the average method was subtracted from the

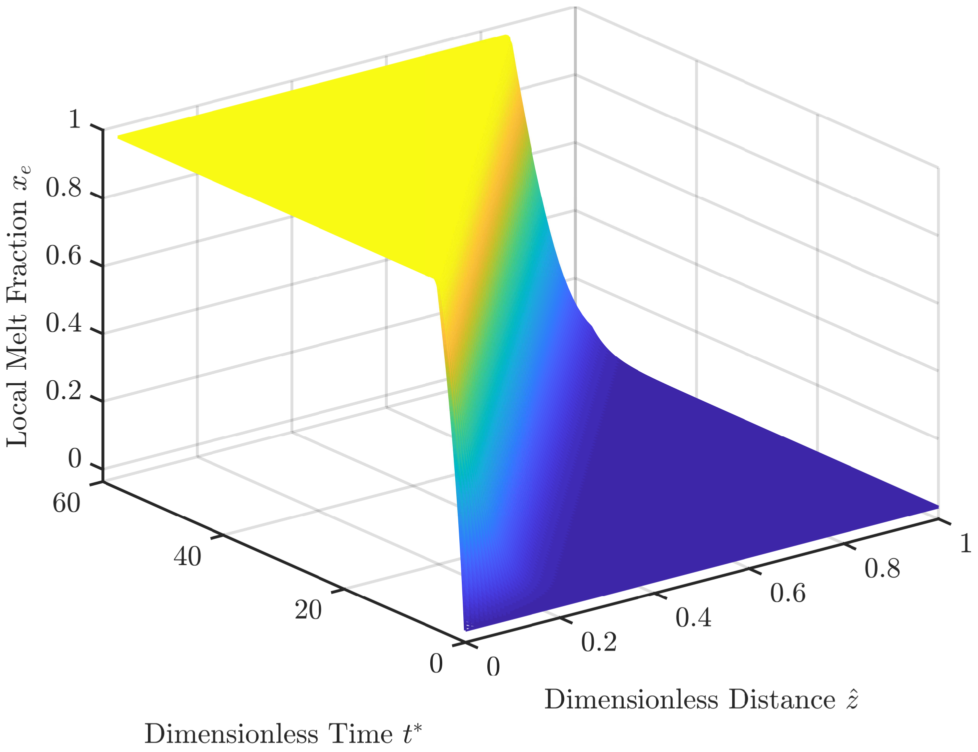

Figure 2.13: Local melt fraction, $x_e$, results of the variable $N_{tu}$ model.

variable method to produce a third plot showing the absolute difference, presented in Fig. 2.15.

Figure 2.15 shows that for the baseline case, the absolute difference in melt fraction between the average and variable $N_{tu}$ methods never exceeds 0.2. However, if analysis at these local values is to be done, this difference may be troublesome and the more precise variable $N_{tu}$ model may be preferable, as the local percent deviation as defined by Eq. 2.29 can be as high as 113%. This can be attributed to the fact that this difference is calculated for a very brief time period and small spatial domain, resulting in high potential for deviation. The RMS error over the entire process is 2.90%. Despite high local percent deviation, the overall discrepancy between the two methods is quite low when considering the full channel length and phase change process. Unless high local accuracy is desired, both methods produce good results for the target effectiveness considered.

## Sensitivity Analysis and Summary of Percent Deviation

Using the same process outlined for the baseline case, several combinations of input parameters were tested as outlined in Tab. 2.7. Each of these test cases produced the same general trends, as summarized in Tab. 2.8. More specifically, each test case produced a peak local percent deviation that was nearly always over 100% (the halved $Z_{coef}$ case was about 80%

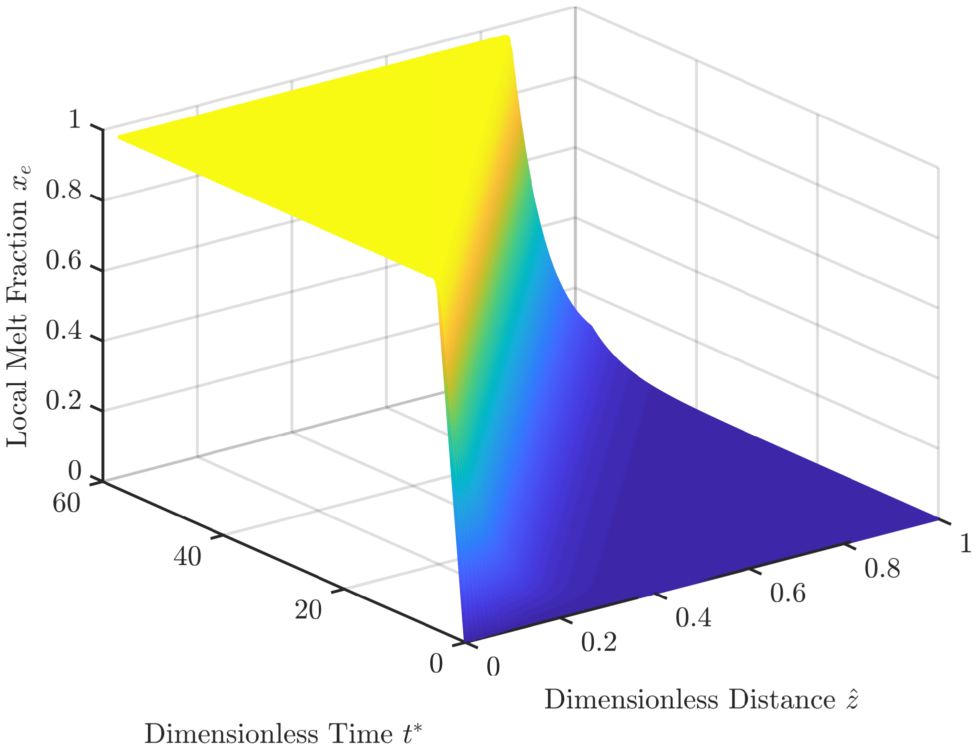

Figure 2.14: Local melt fraction, $x_e$, results of the average $N_{tu}$ model for $\overline{N_{tu}} = 13.0$.

off, at worst). However, each test case had very good global agreement. This suggests that when comparing the variable and average $N_{tu}$ methods, the latter is typically a very good predictor of overall system performance. If the local characteristics are important to the user, then the more accurate variable $N_{tu}$ method should be implemented. Additionally, as these dimensionless parameters are driven by PCM and working fluid selection, as well as TES device geometry, the methods outlined here are very flexible and can be applied to a wide range of TES solutions.

Table 2.8: Summary of sensitivity of variable and average $N_{tu}$ results to changes in dimensionless parameters.

| | Runtime $t^*$ | $\overline{N_{tu}}$ | $\overline{x_{eavg}}$ | % Deviation, TES Effectiveness | Max Local % Deviation | Global % $RMS_e$ |
|---|---|---|---|---|---|---|
| Baseline | 57.5 | 13.0 | 0.895 | 0.574 | 113 | 2.90 |
| 2 $N_{tu,wf}$ | 57.4 | 26.1 | 0.899 | 0.110 | 111 | 2.10 |
| ½ $N_{tu,wf}$ | 58.4 | 6.52 | 0.888 | 1.382 | 115 | 3.85 |
| 2 $R_{we}$ | 29.2 | 13.0 | 0.895 | 0.552 | 113 | 2.90 |
| ½ $R_{we}$ | 114 | 13.0 | 0.895 | 0.582 | 113 | 2.92 |
| 2 $\mathrm{St}_{io}$ | 30.2 | 13.0 | 0.895 | 0.570 | 113 | 2.94 |
| ½ $\mathrm{St}_{io}$ | 112 | 13.0 | 0.895 | 0.577 | 114 | 2.91 |
| 2 $Z_{coef}$ | 57.6 | 8.66 | 0.888 | 1.351 | 140 | 4.64 |
| ½ $Z_{coef}$ | 57.4 | 17.5 | 0.898 | 0.231 | 80.5 | 1.70 |

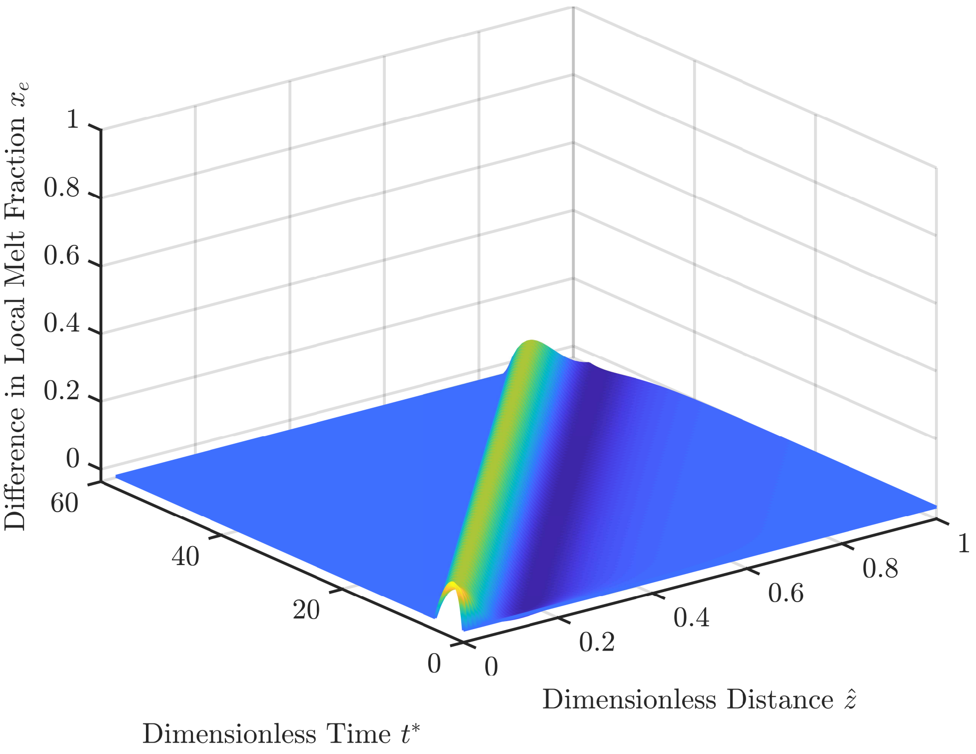

Figure 2.15: Difference in local $x_e$ between variable and average computation methods. The solver is run for both approaches, and the value for $x_e$ based on the average method is subtracted from the variable method.

## 2.8 Conclusions

This chapter has outlined successive iterations to account for a variable overall conductance $UA$ based on a resistor network analogy. When applied to a single unit cell, the variable $N_{tu}$ method's computation for dimensionless overall heat transfer coefficient $U^*$ agreed within 0.011% with an FTCS method that more precisely captures the location of a melt front during a phase change process. Additionally, the variable $N_{tu}$ method agreed very well with general Stefan solutions using quasi-steady approximations with a maximum percent deviation of less than 4%. The variable $N_{tu}$ method agreed with these schemes for determining the time to fully melt a unit cell of PCM within 1%. Applying the variable and average $N_{tu}$ methods to a TES device has demonstrated that the two methods are in good overall agreement globally with a percent deviation of overall TES effectiveness less than 0.6% and RMS error of about 2.90%, though certain points along the flow channel during the transient can have very high percent deviation, typically around 113%, though this would be over a very small time and spatial domain. Thus the variable conductance model would be advisable if local accuracy is desirable. In the case that an overall solution is desired, such as the case of determining the melt time for a TES device, either the variable or average $N_{tu}$ method would suffice.

Finally, it has been shown that the trends are largely independent of values of $N_{tu,wf}$, $R_{we}$, $\mathrm{St}_{io}$, and $Z_{coef}$, with the primary impact being on the time predicted to melt the system of PCM from changes in $R_{we}$ and St. Because these parameters are related to the design of the TES device, this shows that the methods presented in this paper can be readily applied to a wide range of device configurations.

# Chapter 3

# Subsystem Model

## 3.1 Introduction

This paper summarizes the derivation and solution of the governing equations for the energy input and extraction processes in a thermal storage device interacting with a heat exchanger that facilitates this input or extraction. Earlier analyses of phase change thermal storage performance have generally modeled specific details of heat transfer in the storage unit structure with constant boundary conditions, thereby neglecting interaction within a subsystem (e.g. [43, 11, 25]). More recent explorations of PCM thermal storage have included evaluation of PCM materials (e.g. [44, 39]) and efforts to model associate transport processes (e.g. [48, 24, 6]).

Shamsundar and Srinivasan [43] look at a three-dimensional shell and tube configuration both analytically and numerically (via finite difference) in which the working fluid temperature changes axially as heat is transferred from the PCM. To generate effectiveness charts for the TES, the two authors compare the mean frozen fraction to that of the frozen fraction at the inlet for varying sizes, layouts, and Biot numbers. They indicate that the approach could be applied to estimating effectiveness for varying flow rates or inlet temperatures but that the accuracy would be sacrificed.

El-Dessouky and Al-Juwayhel [11] use a second law analysis to characterize the TES by entropy generation numbers. While the authors analyze an entire transient melt/freeze cycle, the PCM remains at the melt temperature throughout. Their case study validates the prediction that more effective TES devices should have higher Reynolds number flows, large heat transfer area, and a greater inlet temperature difference between the working fluid and PCM. Once again, these authors do not investigate beyond constant inlet temperatures.

Ismail and Goncalves [25] explore a two-dimensional model of a tube immersed in PCM. Like our analysis here, they write the energy equation in enthalpy form and couple the change of enthalpy in the PCM with that of the working fluid. Defining an appropriate control volume, the authors employ a finite difference scheme to characterize how the TES melt fraction, NTU, and effectiveness are dependent on the geometry, Biot and Stefan numbers, and working fluid inlet temperature. As the papers before, these authors apply a constant inlet boundary condition without discussing the heat exchanger that might supply this.

Tay, Belusko, and Bruno [48] present a one-dimensional simplified NTU-effectiveness analysis for a shell and tube heat exchanger. The authors find that this approach is valid provided that there is a high heat transfer area. They use thermal resistances to describe the heat transfer from the fluid core through the PCM. This simplified analysis is unlike ours in many ways, including those mentioned above as well as in the way we determine $U$.

Earlier analyses of phase change thermal storage performance have generally modeled specific details of heat transfer in the storage unit structure with constant boundary conditions, thereby neglecting interaction within a subsystem. For example, M. M. Alkilani et. al conducted a theoretical investigation of output air temperature of an indoor heater which utilizes a PCM heat exchanger [3]. In this model, the PCM was used to store solar heat from throughout the day. After the sun set and cooler temperatures were experienced indoors, the cooler ambient air from inside could be directed through the PCM heat exchanger to warm up and flow back into the room to provide heating. This model implemented only a constant input air temperature to the PCM heat exchanger, which was provided by the ambient air temperature from inside the room desired to be heated, thereby neglecting the inevitable changes in the room's, and therefore input air's, temperature. Of the few analyses that have considered a variable inlet air temperature, such as the one produced by S. M. Vakilaltojjar and W. Saman, a simple system consisting only of a PCM heat exchanger was examined, whereas the system considered in this paper includes an external heat exchanger which governs the temperature of the working fluid within the PCM heat exchanger [52].

Most recently, several papers have explored natural convection in three dimensional phase change cells. Bondareva and Sheremet [6] include both momentum and energy equations in the PCM to account for natural convection as well as conduction. The authors use a constant temperature energy input for the melting process and solve for the three-dimensional velocity and temperature fields within the cell to determine the solid-liquid interface location and, thus, the melt fraction with time. This is different from our paper, despite a similar non-dimensionalization technique resulting in some overlap in dimensionless groups. The 2017 paper by Hu, Li, Shu, and Niu [24] also examines natural convection, though these authors employ a three-dimensional lattice Boltzmann model as well as a particle velocity model in order to resolve the temperature field, find the phase interface, and calculate the melt fraction. These authors begin with an enthalpy based heat equation and keep track of the velocities within the PCM to account for natural convection. Their dimensionless groups are similar to the previous paper and they perform numerical parametric studies by varying one of these.

To summarize, many papers mentioned here have applied NTU-effectiveness type modeling to TES units. These papers have tended to non-dimensionalize the governing equations and then employ one of two approaches to evaluate device performance: using working fluid temperature to quantify effectiveness or comparing the local melt fraction to the inlet melt fraction of the device. In this paper, our method of quantifying effectiveness is not significantly different from prior work, but our temporally and spatially varying multi-scale modeling approach, depicted in Fig. 3.1, is. This is novel because it facilitates exploring the relationship between two key dimensionless parameters, $t^*$ and $N_{tu}$, within the context of a subsystem that models realistic operating conditions for a TES.

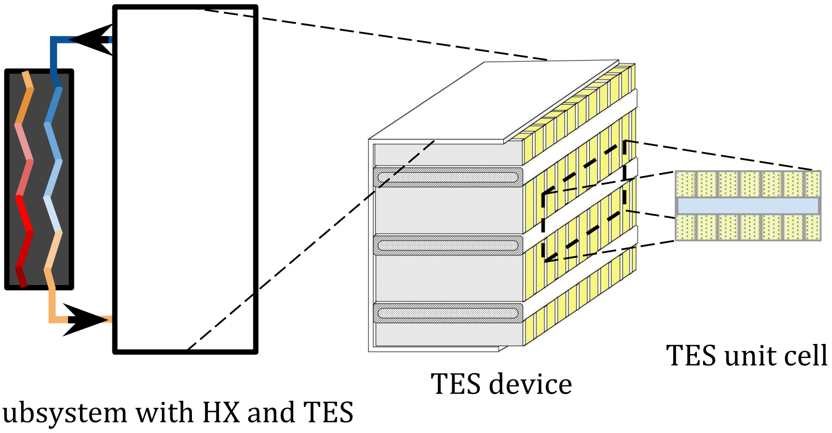

Figure 3.1: Schematic depicting multi-scale nature of problem ranging from the subsystem including the external heat exchanger to the TES device to the unit cell differential element (containing fins, PCM, and flow passage).

While one paper in this literature review discusses the possibility of varying inlet temperature and another examines a simplified cycle, these papers do not analyze a TES device with transient boundary conditions and spatially varying initial conditions for the processes within the cycle. Furthermore, these papers consider the unit cell to the device level scale, but do not examine this within the context of a subsystem that is responsible for delivery of heat to or from the TES. By incorporating a macroscopic lens and considering the subsystem heat exchanger, we can specify exactly how this technology could fit into and improve a power or refrigeration cycle.

We begin at the TES unit cell and model the local heat transfer between the fluid and the PCM using a mean overall heat transfer coefficient $U$. This is similar to analysis of standard heat exchangers, though here, $U$ must be averaged both spatially and temporally. Once the unit cell has been sufficiently analyzed, we move to the device level to solve the governing equations. These are cast in dimensionless form to establish a non-dimensional framework for analysis of the efficiency of the thermal energy input, energy storage, and energy retrieval processes as well as repeated cycling of the TES device. The framework is similar in some ways to the effectiveness-NTU methodology for analyzing heat exchanger performance, but is constructed to capture the inherent transience of these processes. This transience arises not only due to the time-varying nature of phase change but also due to a spatially and temporally varying working fluid temperature within the device. To capture these physics, we analyze a subsystem composed of the TES as well as a coupled heat exchanger that provides the time-varying working fluid inlet boundary condition for the extraction and charging processes. With thermodynamic effectiveness modeling in place for the entire subsystem, the TES unit can be designed to accommodate a variety of heating and cooling applications that would benefit from heat rejection load shifting.

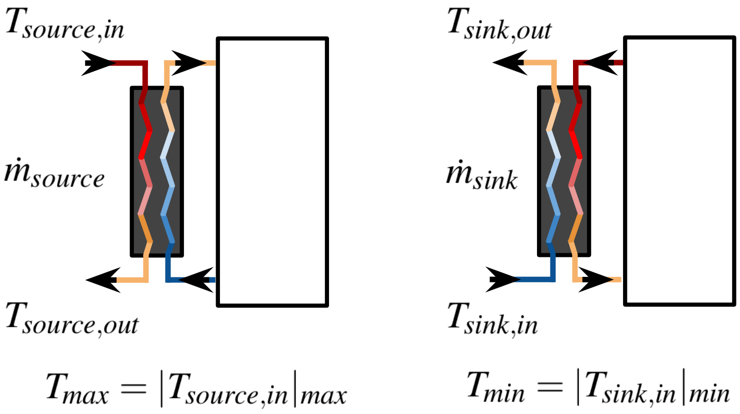

Figure 3.2: TES coupled with an external heat exchanger for cold extraction (left) and cold charging (right).

Figure 3.2 depicts a thermal energy storage device paired with an external heat exchanger, one connected in open loop to a heat source, and the other to a heat sink. A thermal energy storage device is connected via a closed loop that circulates through the heat exchanger. To visualize how this works, we can consider a simple cycle. Ideally, we would like to begin with a completely frozen device. To achieve this, we send a cold working fluid ($\dot{m}_{sink} > 0$) from a sink ($T_{sink,in}$) through the heat exchanger to cool a counterflowing fluid entering the thermal energy storage unit. Provided that the temperature of the fluid entering the TES device is less than the melt temperature, $T_m$, the PCM will undergo freezing. At a later time after a quiescent storage period ($\dot{m}_{closed} = 0$), a hot working fluid ($\dot{m}_{source} > 0$) from a source ($T_{source,in}$) can be chilled by sending it through the heat exchanger, delivering heat to the closed loop fluid entering the thermal storage unit. This warm working fluid will reject heat to the cold storage matrix, provided its temperature is greater than $T_m$, thereby melting the PCM and chilling the closed-loop working fluid. This will chill the open-loop working fluid ($T_{source,out}$) which can be used to augment cooling in various applications. With the subsystem described above, the heat exchanger could be connected to a Rankine cycle or air conditioning condenser in order to precool the open loop fluid and reduce the temperature at which steam or another refrigerant is condensed. At a later time, when the temperature difference with ambient is more favorable, the energy collected from precooling could be released as heat via the same heat exchanger. In short, the idea is to use cold storage to decrease the low system temperature of the power or refrigeration cycle (by heat rejection load shifting) without burning fuel or wasting water.

## 3.2 Analysis Framework

### Coupled Heat Exchanger Energy Balance

For the following analysis, we will use the well established effectiveness-NTU method which posits that, for any given heat exchanger [5]:

$$(\dot{m}c_p)(\Delta T) = C_{min}(T_{hot,in} - T_{cold,in})\varepsilon_{hx} \tag{3.1}$$

With this equation, as well as the device modeling established in Chapter 1, we can examine the subsystem consisting of the TES as well as external heat exchanger.

### Heat Exchanger During Extraction

Conservation Equation(s):

$$\dot{Q}_{source} = (\dot{m}c_p)_{source}(T_{source,in} - T_{source,out}) \tag{3.2}$$

$$\dot{Q}_{source} = (\dot{m}c_p)_{ext}(T_{ext,out} - T_{ext,in}) \tag{3.3}$$

Performance Equation(s):

$$\dot{Q}_{source} = C_{min}(T_{source,in} - T_{ext,in})\varepsilon_{source} \tag{3.4}$$

Transport Equation(s):

$$\dot{m}_{source} = \frac{\dot{Q}_{cond}}{c_{p,source}(T_{cond} - T_{source,out})\varepsilon_{cond}} \tag{3.5}$$

For most relevant applications of this subsystem, the chilled open loop fluid exiting the heat exchanger would be used to condense a working fluid (e.g. steam, refrigerant) in a power or refrigeration cycle. Assuming that the goal of our subsystem is to precool a condenser, we begin by specifying the heat transfer rate in the condenser, $\dot{Q}_{cond}$, to solve for the open loop mass flow rate through the heat exchanger during extraction, as in Eqn. 3.5. To solve this, we will have to begin by estimating $T_{source,out}$, our target for the open loop fluid exiting the heat exchanger. If we solve Eqn. 3.4 for $T_{ext,in}$ we find that

$$T_{ext,in} = T_{source,in} - \frac{\dot{Q}_{source}}{C_{min}\varepsilon_{source}} \tag{3.6}$$

where $C_{min}$ is either $(\dot{m}c_p)_{source}$ or $(\dot{m}c_p)_{ext}$. We can solve Eqns. 3.3 and 3.4 for the unknown temperature, $T_{ext,out}$ but must specify whether $C_{min}$ is associated with the open loop or closed loop fluid.

$$T_{ext,out} = \varepsilon_{so}\frac{C_{min}}{(\dot{m}c_p)_{ext}}T_{so,in} + \left(1 - \varepsilon_{so}\frac{C_{min}}{(\dot{m}c_p)_{ext}}\right)T_{ext,in} \tag{3.7}$$

It is hard to predict ahead of time which fluid will be associated with $C_{min}$ as $\dot{m}_e$ is unknown. We need another functional relationship to establish a value for this flow rate. To do that, we solve the governing TES partial differential equations while iterating through $\dot{m}_e$ until the desired $\varepsilon_{tes}$ is achieved. The only other unknown in the PDEs is $U$ which is derived analytically from a resistance network analogy in Chapter 2.

## TES Device Within Subsystem

The total energy stored in the TES device can be determined in two ways. First, purely looking at the energy the PCM is capable of receiving or rejecting through latent heat transfer,

$$E_{cap} = \rho_{pcm} \nu' L h_{ls} \varepsilon_{tes} \tag{3.8}$$

The total energy stored must not exceed the energy capacity, $E_{cap}$, determined by the TES design. If the time required for the extraction or charging process is specified, knowledge of the heat transfer rate in the source heat exchanger enables us to compute the maximum amount of energy we can transfer to the TES device for a proposed operation time:

$$E_{tot} = \int_0^{t_e} \dot{Q}(t) dt \approx \dot{Q}_{source} t_e \tag{3.9}$$

As the goal is to eventually reject all of this as heat during asynchronous cooling, we can calculate the heat transfer rate in the sink heat exchanger as well:

$$\dot{Q}_{sink} = \int_0^{t_c} \frac{dE}{dt} \approx \frac{E_{tot}}{t_c} \tag{3.10}$$

This equation, in integral form, is challenging to solve for a time-varying heat transfer rate within the sink heat exchanger.

## Heat Exchanger during Charging

Conservation Equation(s):

$$\dot{Q}_{sink} = (\dot{m} c_p)_{sink} (T_{sink,out} - T_{sink,in}) \tag{3.11}$$

$$\dot{Q}_{sink} = (\dot{m} c_p)_{char} (T_{char,in} - T_{char,out}) \tag{3.12}$$

Performance Equation(s):

$$\dot{Q}_{sink} = C_{min} (T_{char,in} - T_{sink,in}) \varepsilon_{sink} \tag{3.13}$$

Transport Equation(s):

$$\dot{m}_{sink} = \frac{\dot{Q}_{sink}}{c_{p,sink}(T_{sink,out} - T_{sink,in})} \tag{3.14}$$

These relations have several unknowns, including $\dot{m}_c$, $\dot{m}_{sink}$, $T_{char,in}$, $T_{char,out}$, $T_{sink,out}$, and which fluid will have $C_{min}$. For the charging process, we can confidently assume that $C_{min}$ is associated with the closed loop fluid $(\dot{m}c_p)_{char}$ such that the $\Delta T$ will be greater within the TES and better drive the heat transfer necessary to refreeze the PCM. With this assumption, we can proceed by solving Eqn. 3.13 for $T_{char,in}$ such that

$$T_{char,in} = \frac{\dot{Q}_{sink}}{\varepsilon_{sink} C_{min}} + T_{sink,in} \tag{3.15}$$

We have justified the assumption that $C_{min} = (\dot{m}c_p)_{char}$ but $\dot{m}_c$ remains unknown. Here, we can take the approach discussed previously to solve the governing TES PDEs while iterating through flow rates until $\varepsilon_{tes}$ is achieved. In this way, we can define $\dot{m}_c$. In order to solve for $T_{char,in}$, we must approximate $\dot{Q}_{sink}$. To do this we will employ Eqn. (3.10) and divide the total energy stored in the TES by the charging process operation time to determine an average $\dot{Q}_{sink}$. $T_{char,out}$ can be found from the conservation equation in terms of an average $\dot{Q}_{sink}$ or from equating the conservation Eqn. 3.12 and performance Eqn. 3.13 and solving for $T_{char,out}$

$$T_{ch,out} = \varepsilon_{si} \frac{C_{min}}{(\dot{m}c_p)_{ch}} T_{si,in} + \left(1 - \varepsilon_{si} \frac{C_{min}}{(\dot{m}c_p)_{ch}}\right) T_{ch,in} \tag{3.16}$$

The last remaining unknowns are $T_{sink,out}$ and $\dot{m}_{sink}$, but it quickly becomes evident that we have no other relation to use in order to define values for either of these variables. In order to proceed, we will do as we did before and specify $T_{sink,out}$. This is more arbitrary than specifying $T_{source,out}$ as a desired temperature for the condenser inlet.

In specifying $T_{sink,out}$, we have several necessary conditions we have to meet. First, we must ensure that whatever choice of $T_{sink,out}$, $(\dot{m}c_p)_{sink}$ should remain greater than $(\dot{m}c_p)_{char}$. We can think about our temperature constraints from a conservative, simplified perspective

$$\Delta T_{sink,min} = T_m - \max(T_{sink,in}) \tag{3.17}$$

For the heat exchanger to function as desired throughout the charging process, the open loop fluid temperature difference, $(T_{sink,out} - T_{sink,in})$ must be less than $\Delta T$ at all times. This is guaranteed to be the case if $(T_{sink,out} - T_{sink,in})$ is less than $\Delta T_{sink,min}$. Furthermore, we can assert that the following inequality should hold:

$$T_{sink,in} < T_{char,out} < T_{sink,out} < T_{char,in} \tag{3.18}$$

We can use any guess for $T_{sink,out}$ to set $\dot{m}_{sink}$ so long as these requirements are met.

With relations in place for heat transfer rates, temperatures, and mass flow rates in the coupled heat exchanger and TES, we can proceed with a non-dimensional formulation for the subsystem.

## Subsystem Governing Equations

Conservation Equation(s):

$$\phi_{closed,out} - \phi_{closed,in} = \frac{\dot{Q}_{hx}}{(\dot{m}c_p)_{closed}(T_{max} - T_{min})} \tag{3.19}$$

Performance Equation(s):

$$\varepsilon_{hx}(\phi_{open,in} - \phi_{closed,in}) = \frac{\dot{Q}_{hx}}{C_{min}(T_{max} - T_{min})} \tag{3.20}$$

The dimensionless formulation established for the thermal energy storage device uses high and low system temperatures to non-dimensionalize both the working fluid and element temperatures. We can also use this for the external heat exchanger during transient operation. In a realistic device, external temperatures would fluctuate throughout the day. These are input into the subsystem model as $T_{open,in}$ in order to determine temperatures in the external heat exchanger, including the inlet boundary conditions to the TES device, $T_{closed,out}$. This is no different than the analysis done for the source and sink heat exchanger above except that it is generalized to be applicable to either. $T_{closed,out}$ can be subsequently non-dimensionalized to serve as $\phi_{bc} = \phi_{cl,out}$:

$$\phi_{cl,out} = \frac{C_{min}}{(\dot{m}c_p)_{cl}}\varepsilon_{hx}\phi_{op,in} + \left(1 - \frac{C_{min}}{(\dot{m}c_p)_{cl}}\varepsilon_{hx}\right)\phi_{cl,in} \tag{3.21}$$

Equation (3.21) is applicable to either heat exchanger and serves as a transient boundary condition for the inlet to the TES if $T_{open,in}$ is a function of time. Alternatively, we could start with a non-dimensional form and combine Eqns. 3.19 and 3.20 and solve for $\varepsilon_{hx}$:

$$\varepsilon_{hx} = \frac{(\dot{m}c_p)_{closed}}{C_{min}}\left(\frac{\phi_{closed,out} - \phi_{closed,in}}{\phi_{open,in} - \phi_{closed,in}}\right) \tag{3.22}$$

By similar heat exchanger analysis, the effectiveness of the TES can be written as

$$\varepsilon_{tes} = \frac{\phi_{closed,out} - \phi_{closed,in}}{\phi_{closed,out} - \theta_m} \tag{3.23}$$

Here, the problem of specifying $C_{min}$ is averted by only having one fluid flowing through the TES. Equation 3.23 is applicable if the device is primarily undergoing latent heat transfer, as is the case for low Stefan number designs of interest here. These are of interest because the subsystem is intended for operation in a typical daytime ambient temperature range, which might encompass a maximum temperature difference of 20°C, containing the fusion temperature somewhere between. As is shown in the case study example, this relatively small temperature difference renders the Stefan number much less than one which is appropriate for such TES subsystems. Equation 3.23 can be solved for $\phi_{closed,in}$:

$$\phi_{closed,in} = (1 - \varepsilon_{tes})\phi_{closed,out} + \varepsilon_{tes}\theta_m \tag{3.24}$$

This result can be substituted into Eqn. (3.21) and $\phi_{closed,out}$ can be found:

$$\phi_{cl,out} = \frac{\varepsilon_{hx}\phi_{op,in}C_{min} + ((\dot{m}c_p)_{cl} - \varepsilon_{hx}C_{min})\varepsilon_{tes}\theta_m}{\varepsilon_{hx}C_{min} - \varepsilon_{hx}\varepsilon_{tes}C_{min} + \varepsilon_{tes}(\dot{m}c_p)_{cl}} \tag{3.25}$$

As above in Eqn. 3.21, $\phi_{bc} = \phi_{closed,out}$. Here, in Eqn. 3.25, the boundary condition takes a very different form and incorporates information about the TES. Knowing which form to use comes down to the numerical scheme employed as well as an understanding of the assumptions in place. Equation 3.21 requires knowledge of both $\phi_{open,in}$ and $\phi_{closed,in}$, the fluid temperature exiting the TES device. This equation makes sense to use with finite difference schemes in which the temperatures are defined throughout the device at all time steps. Conversely, Eqn. 3.25 requires knowledge of $\phi_{open,in}$ and $\theta_m$, both of which are inputs to the programming. While this is simpler to use numerically, it should be employed with caution; this equation is only applicable during latent heat transfer and cannot be used if the PCM near the inlet is not at its melt temperature.

## 3.3 Case Study Example

To provide concreteness, the effectiveness modeling of the thermal energy storage will be used to predict device performance as is done in the literature [37, 14, 17]. Our case study considers a TES unit with a nominal capacity of 1.5 TJ, which would be about the right size to provide asynchronous cooling for a 100 MW power plant [9]. In order to delve into a detailed analysis of the TES unit, operating conditions for the device must first be specified. We prescribe a target effectiveness for the TES as well as desired times for operation. We assume that the extraction process, removing heat from the working fluid and melting the PCM, would occur during a 10 hour period. For our preliminary study, we consider the extraction process begins with the TES completely frozen. The initial temperature of the PCM during extraction, $T_{0,e}$, is assumed to be at the melting temperature.

We assume that the charging process of refreezing the PCM would occur during a 9 hour period following a 3 hour period of storage. The initial temperature of the PCM during charging, $T_{0,c}$, is close to the final temperature distribution after extraction $T_{f,e}(z)$, but slightly shifted due to thermal equilibration during storage. This distribution exists because the working fluid and element temperature vary along the flow passage as heat is transferred between the working fluid and the PCM. Only where latent heat transfer is taking place can we expect the element temperature to be $T_m$.

However, during the extraction process, the PCM near the inlet undergoes and completes phase change more quickly than the PCM further downstream. After complete melting, this PCM near the inlet still accepts heat in the form of sensible heat transfer raising its temperature.

Table 3.1: Input parameters for thermal storage performance calculations with a time varying boundary condition.

Device Geometry

| | | |
|---|---|---|
| Wetted perimeter of flow passage, $s_w$ | 47.1 | mm |
| Cross sectional area of flow passage, $A_c$ | 44.9 | mm$^2$ |
| Storage matrix volume per unit flow length, $\nu'$ | 99.6 | mm$^2$ |
| Channel length, $L$ | 407 | mm |

Operating Conditions

| | | |
|---|---|---|
| Initial extraction temperature, $T_{0,e}$ | 30 | °C |
| Initial charging temperature, $T_{0,c}$ | $f(z)$ | °C |
| Hot working fluid inlet temp., $T_{wi,e}$ | $f(t)$ | °C |
| Cold working fluid inlet temp., $T_{wi,c}$ | $f(t)$ | °C |
| Extraction mass flow rate, $\dot{m}_e$ | 2990 | kg/s |
| Charging mass flow rate, $\dot{m}_c$ | 1975 | kg/s |

System Performance

| | | |
|---|---|---|
| Minimum storage effectiveness, $\varepsilon_{tes}$ | .95 | |
| TES nominal capacity, $E_{tot}$ | 1.5 | TJ |
| Extraction time, $t_e$ | 36000 | s |
| Charging time, $t_c$ | 32400 | s |

When the extraction process stops, energy is stored in the device until a more favorable temperature difference with ambient can be achieved. During storage, the same set of governing equations are solved, with the mass flow rate set to zero, eliminating the first order advection term from the working fluid equation. The temperature and melt fraction distributions change slightly due to the driving normal temperature gradient between the PCM matrix and working fluid. As thermal diffusivities of both the PCM ($\sim 10^{-5}$m$^2$/s) and working fluid ($\sim 10^{-7}$m$^2$/s) are quite small, and the storage time is relatively brief, axial conduction along the passage is neglected as in the governing partial differential equations. If axial conduction were included, the thermal diffusivities of the working fluid and the PCM matrix would serve as coefficients to their respective second order temperature diffusion terms. Considering the larger of these, it seems that the relevant time scale for axial conduction in the PCM matrix is something like $L^2/\alpha$ ($\sim$ 16500 s). This is roughly double the storage time considered here ($\sim$ 7200 − 10800 s). If the materials in the TES unit have higher thermal diffusivities, this modeling framework could be modified to include the effects of axial conduction. Retaining the original set of governing equations for storage, $T_{0,c}$ will be a function of the axial coordinate, $z$, as reflected in Table 3.1. The working fluid inlet temperatures for extraction and charging must also be defined. These temperatures are the boundary conditions for the TES device. These selected baseline conditions are enumerated in Table 3.1.

Table 3.2: Dimensionless input values for thermal storage performance calculations.

| | $N_{tu}$ | $R_{we}$ | $\mathrm{St}_{io}$ | $t^*$ |
|---|---|---|---|---|
| Extraction | 36.84 | 0.47 | 0.13 | 58.99 |
| Charging | 37.81 | 0.47 | 0.13 | 34.66 |

For this case study, the thermal storage device is assumed to be a plate-fin heat exchanger with alternating layers of phase change material and rectangular working fluid flow passages on the liquid side. A 50/50 mixture of ethylene glycol and water is ideal in this system because of its applicability in a wide range of operating temperatures. This working fluid has also been combined with anti-corrosion agents for many years to reduce fouling in heat exchangers. Lithium nitrate trihydrate (LNT) is an ideal candidate for phase change material due to its high energy density. This PCM also has desirable thermal conductivity and cost. Furthermore, it is chemically non-reactive and stable. The melting temperature of the PCM was taken to be 30°C, which is possible with a specific variation of LNT [42]. Heat transfer into the PCM can be enhanced using metal structures; effective thermal properties of the matrix containing LNT and aluminum fins are used in the model.

Dimensional parameters for the case study are used to calculate the dimensionless variables in Table 3.2. Some variables, including $N_{tu}$, differ for the extraction and charging processes because the mass flow rate and overall heat transfer coefficient differ. Others, such as $R_{we}$ and $\mathrm{St_{io}}$ remain consistent. If the dimensionless variables are changed, the simulation will naturally lead to different results, as explained in the parametric study of Chapter 1 and test cases of Chapter 2.

## Extraction / Melting

During cold extraction, heat is delivered to initially frozen PCM in the storage device. The operation time and mass flow rate through the channel are chosen to give rise to dimensionless parameters that make it possible to achieve a prescribed TES effectiveness. The dimensionless parameter values for extraction from Table 3.2 were input into the three governing partial differential Eqns. (1.9) -(1.11) to determine melt fraction and temperature throughout the element material.

For the dimensionless parameter values listed in Table 3.2, the spatial variations of dimensionless working fluid and storage element temperatures, and melt fraction are shown for 3 moments in time in Fig. 3.3a. As the transient proceeds, more of the storage raises in temperature towards the inlet working fluid temperature, and an increasing fraction of the

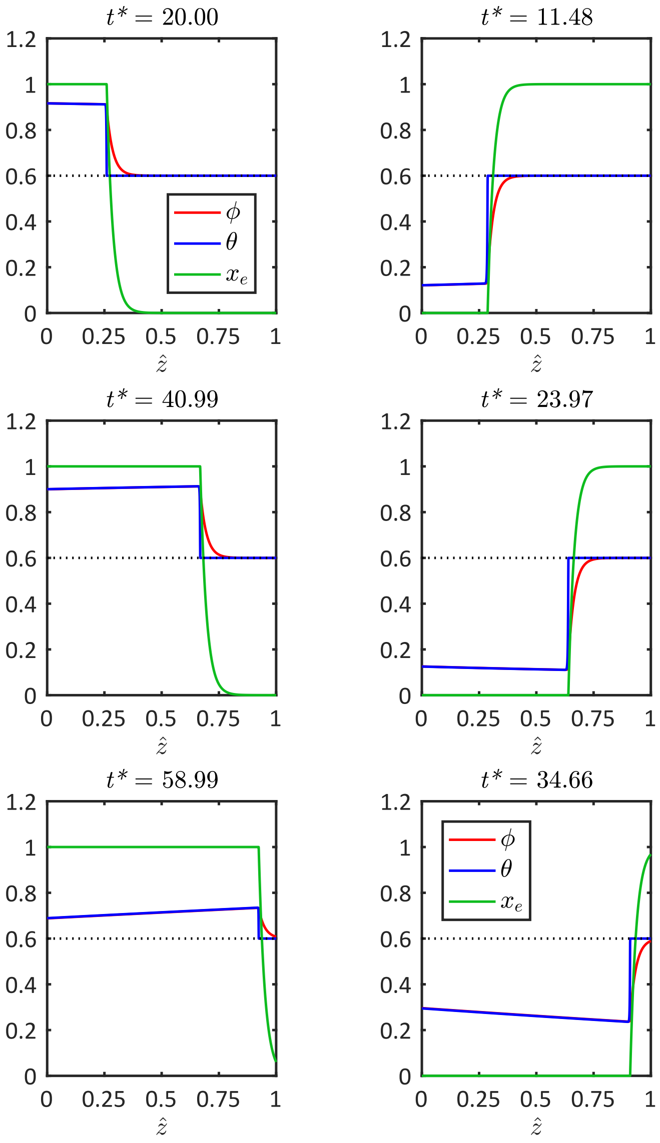

(a) Extraction process (b) Charging process

Figure 3.3: Dimensionless fluid and element temperature($\phi$, $\theta$) and melt fraction ($x_e$) profiles through space and time with case study parameters from Table 3.2.

PCM is melted. In the first snapshot, the dimensionless working fluid temperature, indicated by the red line, enters the TES at a hot working fluid inlet temperature. As it travels through the device, it rejects heat through the channel walls to the PCM and exits at a lower temperature. The dimensionless element temperature, indicated by the blue line, begins to increase due to the hot working fluid. The melt fraction indicated by the green line has begun its ascent from a solid towards a liquid state. At a later time, the hot working fluid has heated the element temperature up as well as almost melted the PCM to its dimensionless liquid state of 1.

## Charging / Freezing

During the cold charging operation, the cooling working fluid loop is activated to refreeze the PCM. The set of partial differential Eqns. (1.9) - (1.11) are also solved for charging the TES device. The dimensionless parameter values calculated from the baseline case for charging are listed in Table 3.2.

Figure 3.3b presents three snapshots in time of the cold storage charging process. In the first snapshot, the dimensionless working fluid temperature, indicated by the red line, enters the TES at a cold working fluid inlet temperature. As it travels through the device, it accepts heat through the channel walls from the PCM and exits at a higher temperature. The dimensionless element temperature, indicated by the blue line, begins to decrease due to the cool working fluid. The melt fraction, indicated by the green line, has begun its descent from a saturated liquid towards a solid state. At a later time, the cool working fluid has almost cooled the element temperature down as well as frozen the PCM towards its dimensionless solid state of 0.

## Subsystem Full Cycle

Moving forward, we are able to fully take into account the cycling of the device. We can visualize the paired extraction and charging processes by looking at the entire cycle as shown in Fig. 3.4.

Figure 3.4, depicting the 24 hour cycle schematic, has a lot of information to digest. First, we can look at the top left box - extraction (1). Here, hot ambient air passes through a heat exchanger referred to as the precooler which cools air by transferring heat to a closed loop working fluid. This closed loop working fluid flows through the TES, transfers heat to the PCM matrix, and re-emerges to continue cooling the flowing air. This cooled dry air is subsequently used to condense steam in the condensate manifold. The precooling/extraction process continues for the desired duration specified by plant operators, transferring heat to melt the amount of PCM prescribed by the TES effectiveness. After this period of extraction, we move into the next process indicated by the top right box: storage (2). During this time, no fluid flows through the TES device. Instead, the device thermally equilibrates such that the fluid and adjacent PCM eventually achieve the same temperature. If this temperature equilibration causes the PCM to reach its melting point, it will undergo further melting as

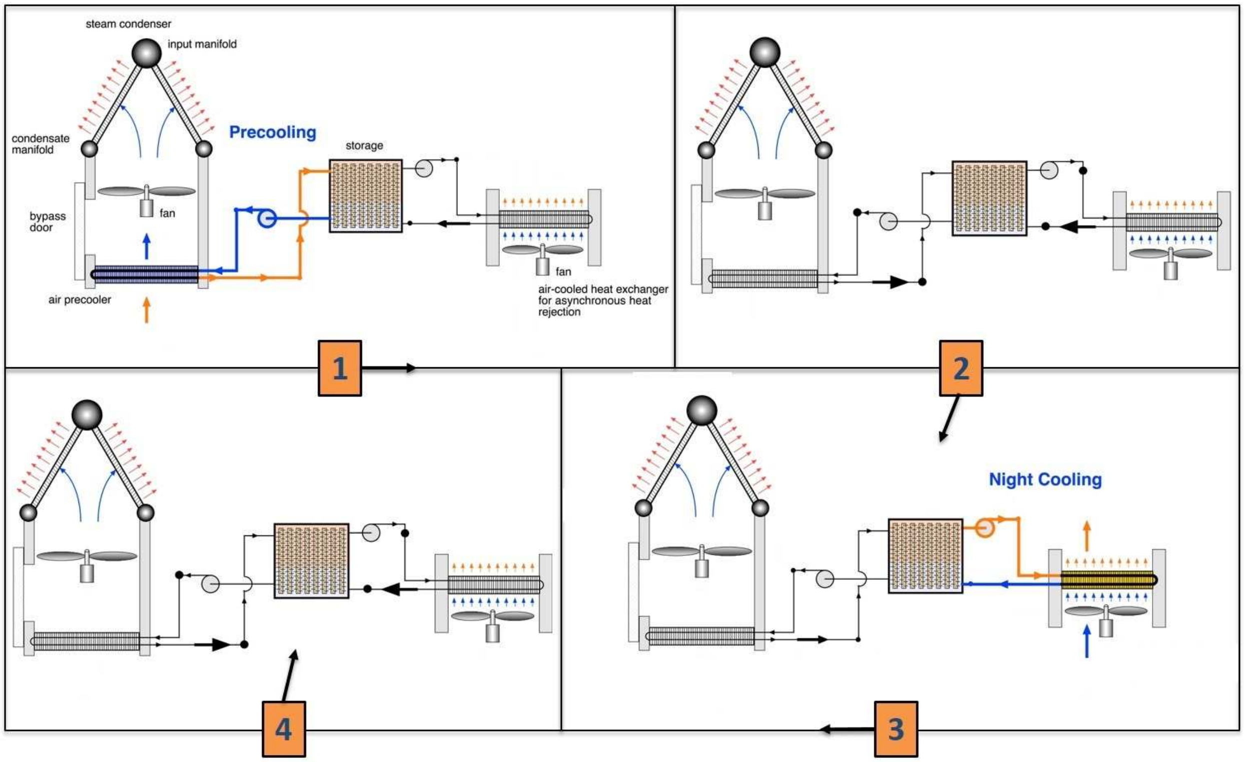

Figure 3.4: Cycle consisting of precooling, storage, night cooling, and storage once more.

dictated by the driving temperature difference. After this period of storage and equilibration, the PCM in the TES device needs to be frozen again for future use in precooling. To accomplish this, we move into the charging process, depicted in the bottom right box (3). At this time, the sink heat exchanger is employed in order to transfer heat from the PCM matrix within the thermal storage to the atmosphere. A cool open loop fluid passes through the sink heat exchanger, removing heat from the closed loop fluid. This chilled fluid enters the TES device, and, because it flows through at a lower temperature than $T_m$, enables the PCM to begin freezing. This closed loop fluid exits the TES warmer than when it enters, but is subsequently rechilled by the open loop fluid in the night cooler. This process continues for a specified amount of time, which should be enough to return the TES to its desired starting point, or melt fraction distribution, for later precooling to take place. Before that happens, the device undergoes another period of storage, shown in the bottom left (4). Once again, the device thermally equilibrates and is ready to recommence the cycle.

Further cycling of the device should lead to a steady state operation with a more symmetric distribution of average melt fraction through the paired extraction and charging processes. The final charging condition will serve as the initial extraction condition after storage and vice versa. We specify operating conditions so that the device remains in this window, melting and freezing the fraction of PCM according to its effectiveness target.

For the applications of interest discussed in the introduction, we are interested in device modeling that accounts for the time-varying temperatures and boundary conditions encountered in real systems. In order to understand what happens during this asynchronous cooling cycle, we can look at Fig. 3.5. This figure contains the relevant results obtained by solving the TES device and subsystem governing equations.

The open loop working fluid (air) inlet temperatures were approximated as parabolic in nature, reflecting the variation we might see during a typical day. The open loop air exit temperatures were not specified. Instead, we solve the heat exchanger performance equation for $T_{open,out}$:

$$T_{op,out} = T_{op,in}\left(1 - \frac{C_{min}}{(\dot{m}c_p)_{op}}\varepsilon_{hx}\right) + T_{cl,in}\frac{C_{min}}{(\dot{m}c_p)_{op}}\varepsilon_{hx} \tag{3.26}$$

where $T_{open,in}$ is known, $T_{closed,in}$ is calculated from the TES PDEs, $\dot{m}_{open}$ is determined from an average $\dot{Q}_{hx}$, and $\dot{m}_{closed}$ is found via iteration for a prescribed effectiveness. If $C_{min}$ is $(\dot{m}c_p)_{closed}$ then the computation for $\dot{m}_{open}$ requires knowledge of $T_{open,out}$ as in Eqn. (3.5). To calculate an appropriate constant flowrate, $\dot{m}_{open}$, we initially approximate $T_{open,out}$ and finally solve for it here.

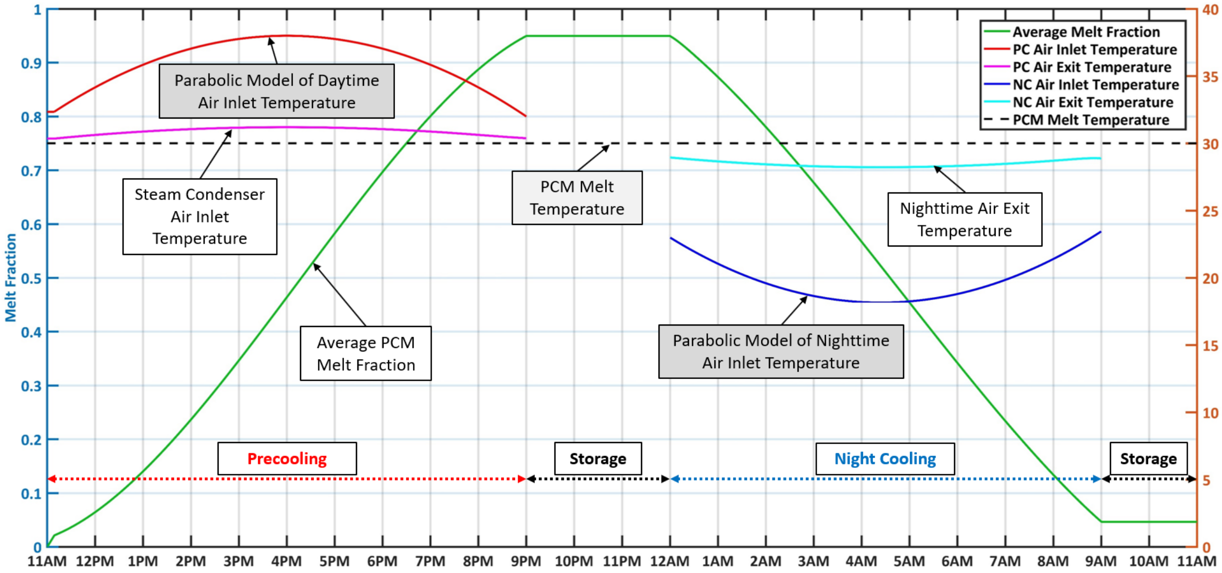

Figure 3.5: 24 hour cycling of a 1.5 TJ TES device and subsystem with case study parameters from Tables 3.1 and 3.2.

We find that the air temperatures depicted in Fig. 3.5 satisfy the requirement that they are higher than $T_m$ during extraction and lower than $T_m$ during charging. This ensures that the heat transfer occurs in the appropriate direction for both processes - melting the PCM during the day and freezing the PCM over night. This is reflected by the green line showing a spatially averaged melt fraction throughout the entire 24 hour cycle.

Most importantly, this figure highlights the usefulness of thermal energy storage for these applications. Load shifting, storing energy during the day and subsequently rejecting it at night, takes advantage of favorable temperature differences that are a function of a time-varying ambient temperature. Furthermore, the lower air inlet temperature to the steam condenser improves the Rankine cycle efficiency, which is highly beneficial both financially and environmentally. The specific improvement will be investigated more thoroughly in the remainder of Chapter 3.

## 3.4 Preliminary Discussion

The dimensionless effectiveness-NTU analysis framework developed here for the thermal storage and coupled heat exchanger can be a useful tool for design optimization of the TES unit and the associated subsystems for asynchronous cooling and other thermal storage applications involving transient storage and retrieval processes.

In order to accomplish heat rejection load shifting, we examined the TES device in the context of a subsystem, paired to a heat exchanger that is used to input and later reject energy from the TES. In the case study examined in this paper, we demonstrated that the model has the capability to predict performance for time-varying working fluid inlet temperature to the heat exchanger and thus the TES. Unlike earlier models, the time-varying inlet temperature case is significantly more complicated because it introduces time-varying boundary conditions for the differential equations in the model. Our numerical approach enables us to handle this challenge well. The computational framework, described in depth in this paper, can serve as a valuable tool to model and optimize time-varying thermal energy storage subsystems for a multitude of power and refrigeration applications.

## 3.5 Optimizing TES Subsystem Design

The remainder of this chapter is devoted to realist application of a subsystem model with heat exchangers to freeze the thermal storage at night when air temperatures are low, and to precool the air flow for a power plant air-cooled condenser during peak daytime air temperatures. The subsystem model is computationally linked to a model of a real Rankine cycle power plant performance to predict how much additional power the plant could generate as a result of the asynchronous cooling augmentation provided by this subsystem.

This model of a 24-hour cycle operation of a TES subsystem connected to a Rankine cycle power plant will incorporate real-world temperature data. Furthermore, we will explore optimization of the TES subsystem and the financial payback period associated with use of such technology. This analysis facilitates exploring a subsystem that models realistic operating conditions for a TES.

The proposed TES device that is exhibited in the model utilized by this paper operates in the following way. The TES device can be used to gather energy during the day, store it, and then reject it asynchronously (at night) rather than continuously throughout the day as is standard in many applications. This is particularly useful for many reasons. First, asynchronous cooling removes the need for peak load production, which is typically more expensive both financially and environmentally. Second, temperature differences are greater at night when ambient air is cooler, rendering heat transfer more thermodynamically efficient from a simple Carnot standpoint.

The four process (extraction, storage, charging, and storage) comprising the full cycle occur consecutively with operatiuon times dictated by the ambient temperature. Storage is strategically designed to occur when the inlet air temperature is very close to the melting temperature of the PCM ($T_m \pm 0.8°\text{C}$), as little to no advantage would be gained from running the TES system during this time. If desired, the bypass door could be opened throughout storage to allow air directly from the surrounding environment to cool the steam condenser.

## 3.6 Implementation and Results

To explore a subsystem that models realistic operating conditions for a TES, a moderate plant size of 50 MW was chosen as a starting point to model. The PCM utilized in this analysis by the described model is lithium nitrate trihydrate ($LiNO_3{\cdot}3H_2O$). This material is a reliable salt hydrate with almost no subcooling effect or observed phase segregation during thermocycling in tests involving small mass and large mass samples. The only potential setback is the cost compared to other inorganic PCM options; however, based on volumetric storage ability, lithium nitrate trihydrate is one of the best PCMs to consider. Some important properties of this material are its melting/freezing temperature of 30°C and its latent heat of fusion of 278.14 kJ/kg. The volume of the TES, used as a metric in this paper, is calculated by finding the required number of flow channels to determine the total frontal area ($n_{chan} * A_c + (n_{chan} - 1) * \nu'$) and multiplying that quantity by the length of the flow passage ($L$). This volume includes both the PCM matrix and the flow passages in the TES, with geometry in Table 3.1.

A specific water-scarce location with need to utilize water conservation techniques was also selected to provide an area in which the TES would be beneficial. In this case, Las Vegas, Nevada is the chosen location because it lies in a desert region less than 50 miles away from the Walter Higgins Generating Station, a powerplant that currently utilizes air cooling techniques and could benefit from the TES precooling system discussed in this paper.

With Las Vegas chosen as the region of interest and the modeling techniques determined, hourly weather data from January 2013 through December 2017 was obtained from the Las Vegas Henderson Airport Weather Station (WBAN 53127) through use of the Local Climatological Data Tool on the NOAA website. Because the precooling process is most necessary when the outside air temperature is hottest, July and August were selected as the months that would be further analyzed. The hourly temperature data from 2013 to 2017 for July and August are plotted in Figures 3.6 and 3.7, respectively. Looking at the average hourly temperatures over the years, it can be seen that July has a peak temperature of nearly 37°C, and August has a peak temperature of nearly 35°C.

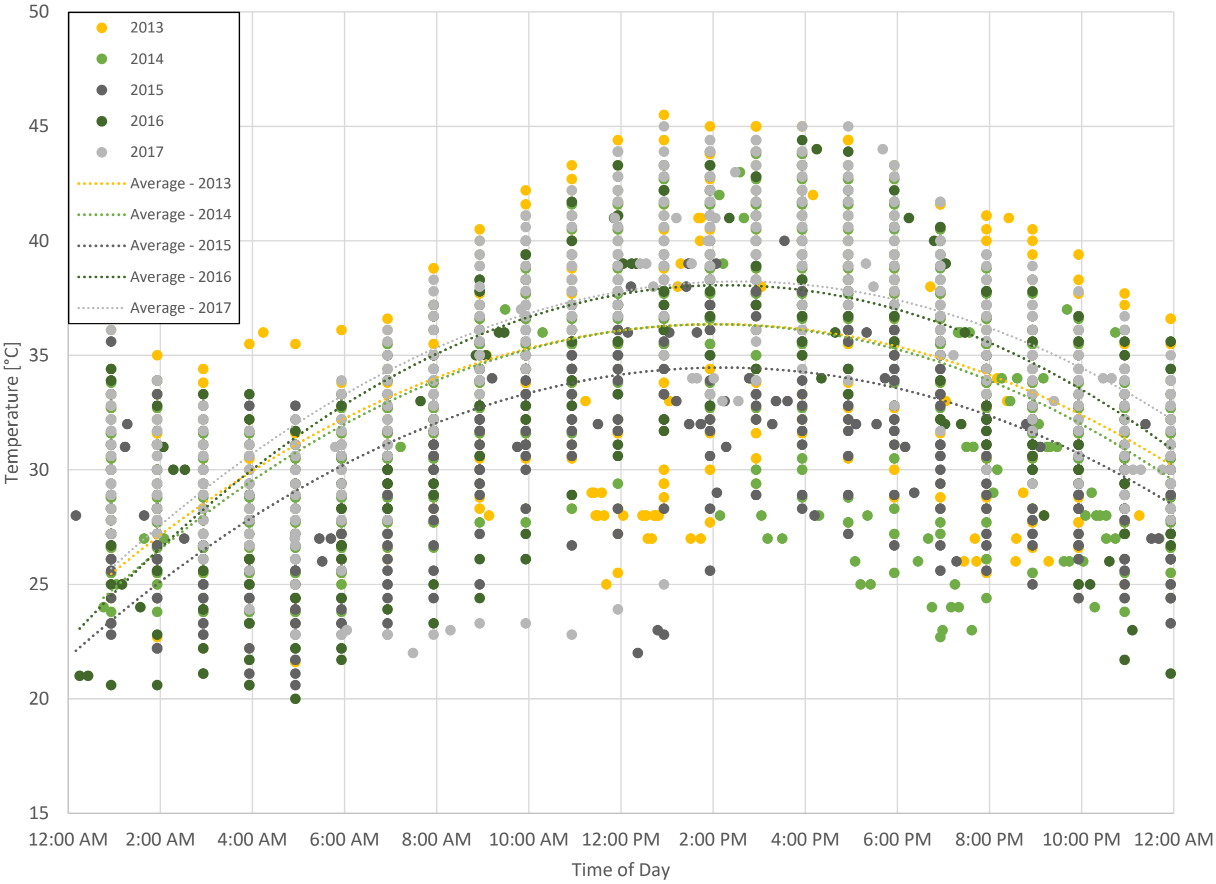

Figure 3.6: Hourly temperature data for July in Las Vegas, NV from 2013 to 2017.

These peak temperatures put the month of July as the best candidate to analyze for the precooling process. However, another factor to consider is also the minimum temperature achieved throughout the day and how that relates to the selected PCM melt temperature of 30°C. There is a concern that the ambient nighttime temperature might not dip below the melt temperature of the PCM, which would impede recharging of the TES device. Therefore, environments that are more likely to reach sufficiently low temperatures at night are selected for analysis in this paper. In practice, the TES would include a control system to regulate its operation based on daily weather data and future weather predictions. Such a control system would be able to manage which days it would be optimal to have the TES in use.

Reviewing the average hourly temperature curves of days in July and August, it was observed that the average daily minimum temperature in July is only about 3°C below the PCM melt temperature, but the average daily minimum temperature in August is about 6°C

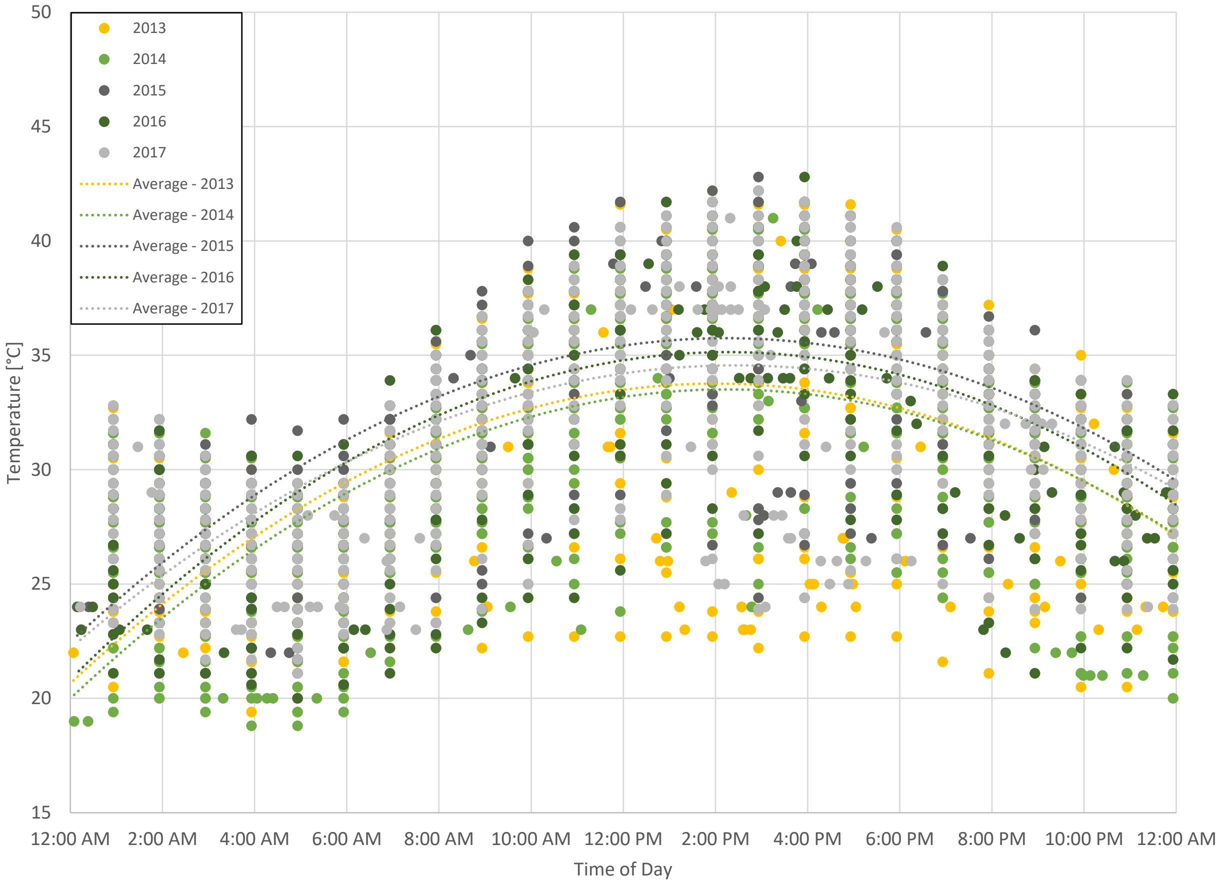

Figure 3.7: Hourly temperature data for August in Las Vegas, NV from 2013 to 2017.

below the PCM melt temperature. Therefore, August was selected as the month to analyze in the model for the precooling process.

The average hourly temperatures for the month of August must be imported into the model. To facilitate this, an approximate temperature curve for an average 24-hour period in August was generated using a polynomial fit, as shown in Figure 3.8. Reviewing this temperature curve, it was determined that, based on the selected PCM melt temperature of 30°C, extraction could be implemented for a maximum of 12 hours. Using this extraction time as a starting point, the model was adjusted to contain enough PCM to be fully utilized throughout the entire extraction period, with the flow rate per channel in the TES adjusted such that the extraction and charging processes would both reach 95% effectiveness, which corresponds to 95% of the PCM melting and freezing, respectively.

After adjusting parameters, the August temperature curve was input into the model. With this ambient temperature data and PCM melt temperature, the appropriate amount of PCM can be determined. For 12 hours of extraction, the PCM was nearly fully melted and refrozen throughout the day. Results show that, during extraction, the precooling process decreases the air inlet temperature into the steam condenser by about 6°C, which greatly improves the ability of the plant to efficiently generate energy.

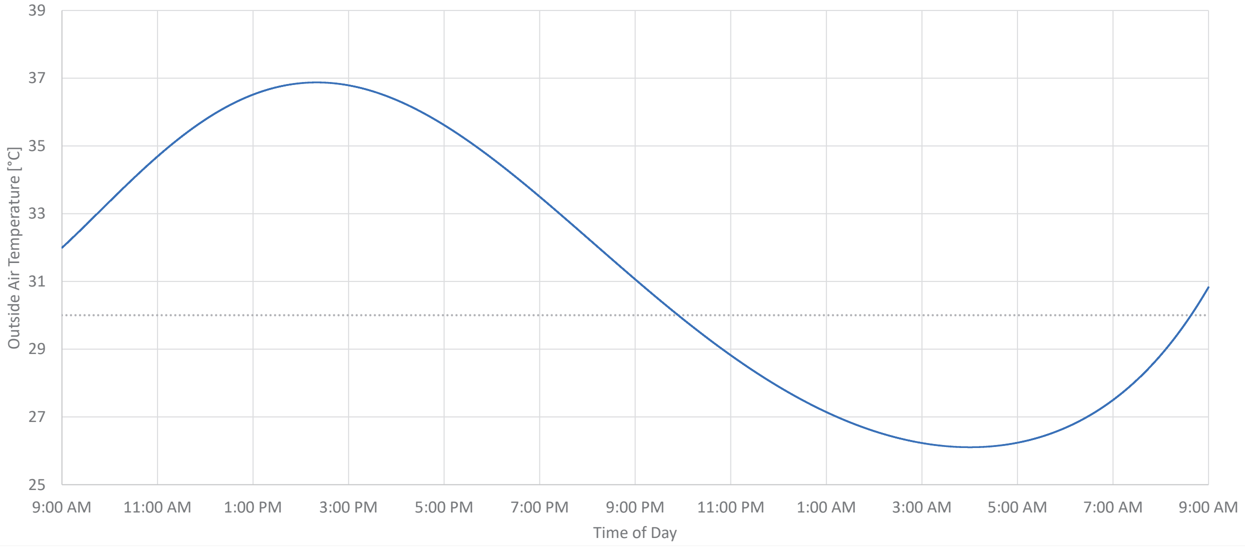

Figure 3.8: Polynomial fit of outside air temperature on average August day in Las Vegas.

The gains achieved through this decrease in condenser inlet air temperature over the 12-hour extraction period can be calculated by using the following equations. First, the efficiency of the Rankine cycle of the power plant is calculated,

$$\eta_{Rankine} = \eta_{Carnot}(1 - \frac{T_{source,out}}{T_{boiler}}) \tag{3.27}$$

where $T_{boiler}$ is the boiler temperature, which in this case was set to 362.4°C and $T_{source,out}$ is the time varying air exit temperature from the heat exchanger which serves as the inlet to the steam condenser. Next the power output is calculated,

$$\dot{W} = \dot{Q}\frac{\eta_{Rankine}}{(1 - \eta_{Rankine})} \tag{3.28}$$

Subsequently, the energy produced over the extraction period is calculated.

$$E_{ext} = \int_0^{t_e} \dot{W} dt \tag{3.29}$$

Next, the energy produced over the day, $E_{day}$, is:

$$E_{day} = \int_0^{24 \text{ hours}} \dot{W} dt \tag{3.30}$$

Following these calculations, the gain in energy over the extraction period, $\Delta E_{ext}$, is calculated,

$$\Delta E_{ext} = E_{ext} - E_{else} \tag{3.31}$$

where $E_{else}$ is the energy that would be produced over the extraction period if the process had taken place without precooling. Finally, the percent gain in energy production over the extraction period, $\% \uparrow E_{ext}$, and the percent gain in energy production over the day, $\% \uparrow E_{day}$, are calculated.

$$\% \uparrow E_{ext} = \frac{\Delta E_{ext}}{E_{else}} \quad ; \quad \% \uparrow E_{day} = \frac{\Delta E_{ext}}{E_{else} + E_{day}} \tag{3.32}$$

Using Equation 3.32, it is found that the 6°C temperature difference increases the kWh produced during the extraction period by 1.70%, and it is calculated that the temperature difference increases the kWh produced throughout the entire day by 0.85%. These percentages correspond to a production gain of 10.4 MWh, as calculated with Equation 3.29.

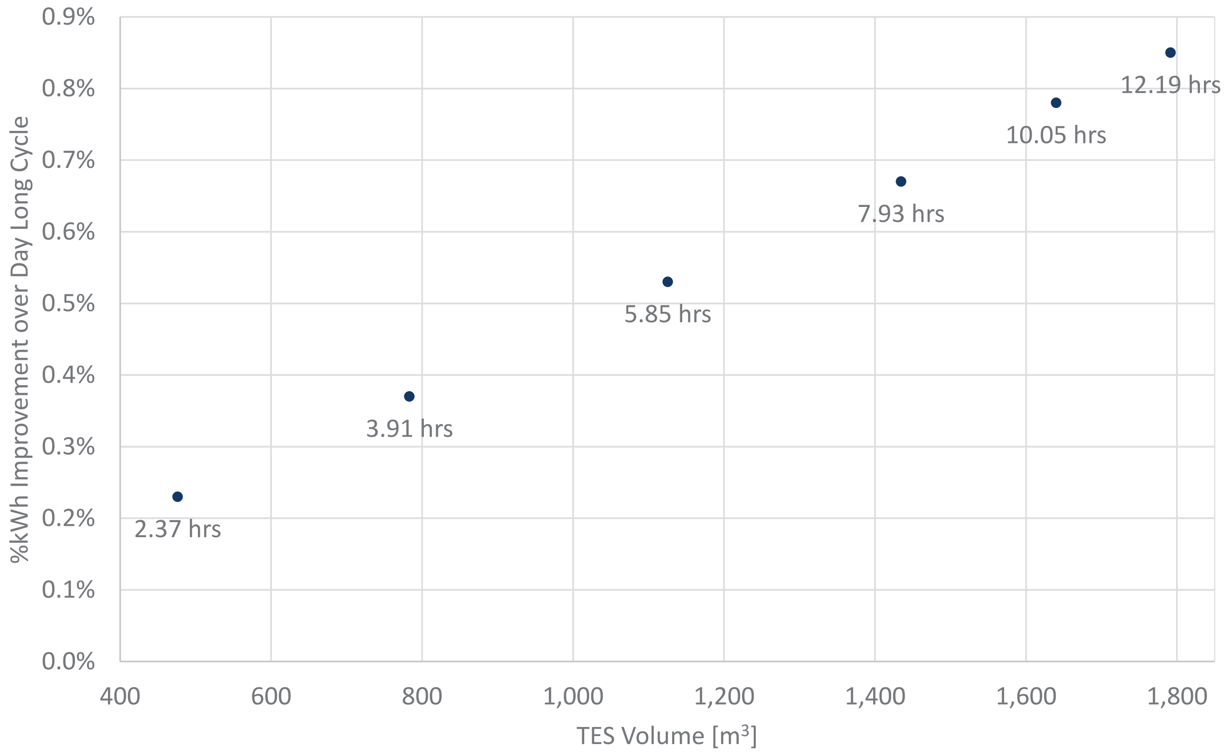

Figure 3.9: %kWh gained over day for different extraction times vs. TES volume for PCM melting temperature of $T_m = 30°\text{C}$ in Las Vegas for average August day.

While this is a substantial amount of energy gain, the goal of the precooling process is to increase the efficiency of energy production by as wide a margin as possible. With this goal in mind, several different extraction times were tested to see if energy production could be further improved. To ensure that the PCM was being fully utilized throughout these extraction periods, the number of channels in the TES as well as the flow rate per channel were adjusted such that the extraction and charging processes would reach 95% effectiveness. Figure 3.9 shows the relationship between the percent increase in kWh over the extraction period and the volume of the TES. This data shows a very clear relationship in which the percent kWh gained over the day increases as the volume of the TES, and therefore the length of extraction, increases.

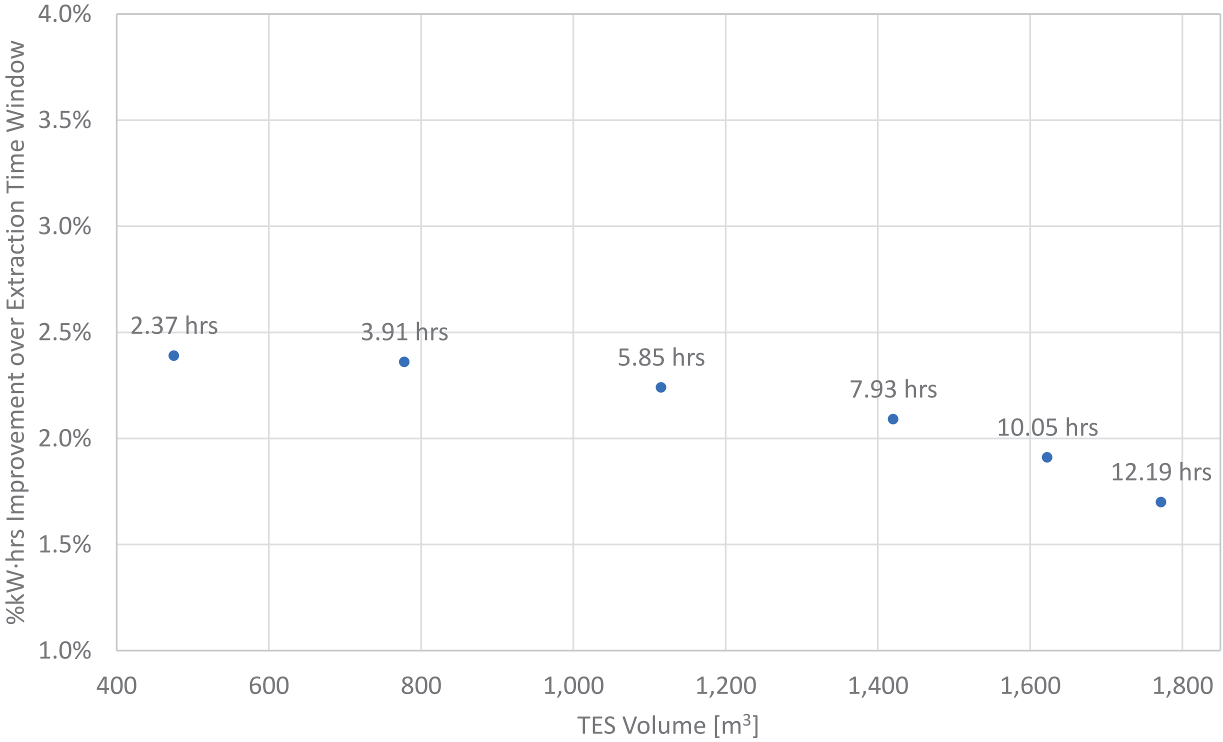

Figure 3.10: %kWh gained over extraction time for different extraction times vs. TES volume for PCM melting temperature of $T_m = 30°\text{C}$ in Las Vegas for average August day.

Figure 3.10 shows the relationship between the percent increase in kWh over the extraction period and the volume of the TES. This data shows a relationship in which the percent kWh gained over the extraction period decreases as the volume of the TES, and therefore the length of extraction, increases.

The two relationships in Figures 3.9 and 3.10 are directly at odds with one another. The trend in Figure 3.9 suggests that the TES volume should be maximized in order to increase the overall gain of kWh produced, and Figure 3.10 suggests that the TES volume should be minimized in order to increase the overall efficiency of the precooling process. To balance these two parameters, the percent kWh gained over the extraction period and the percent kWh gained over the day were both normalized by their respective maximums and plotted versus the TES volume, as shown in Figure 3.11.

The trend in Figure 3.11 shows that the percent increase in kWh gained over the extraction period and the percent kWh gained over the day can be balanced out, and where they cross should determine the optimum TES volume, which is in this case is found to be about 1500 $m^3$. Obtaining the optimum TES volume also allows for the determination of the optimum extraction time.

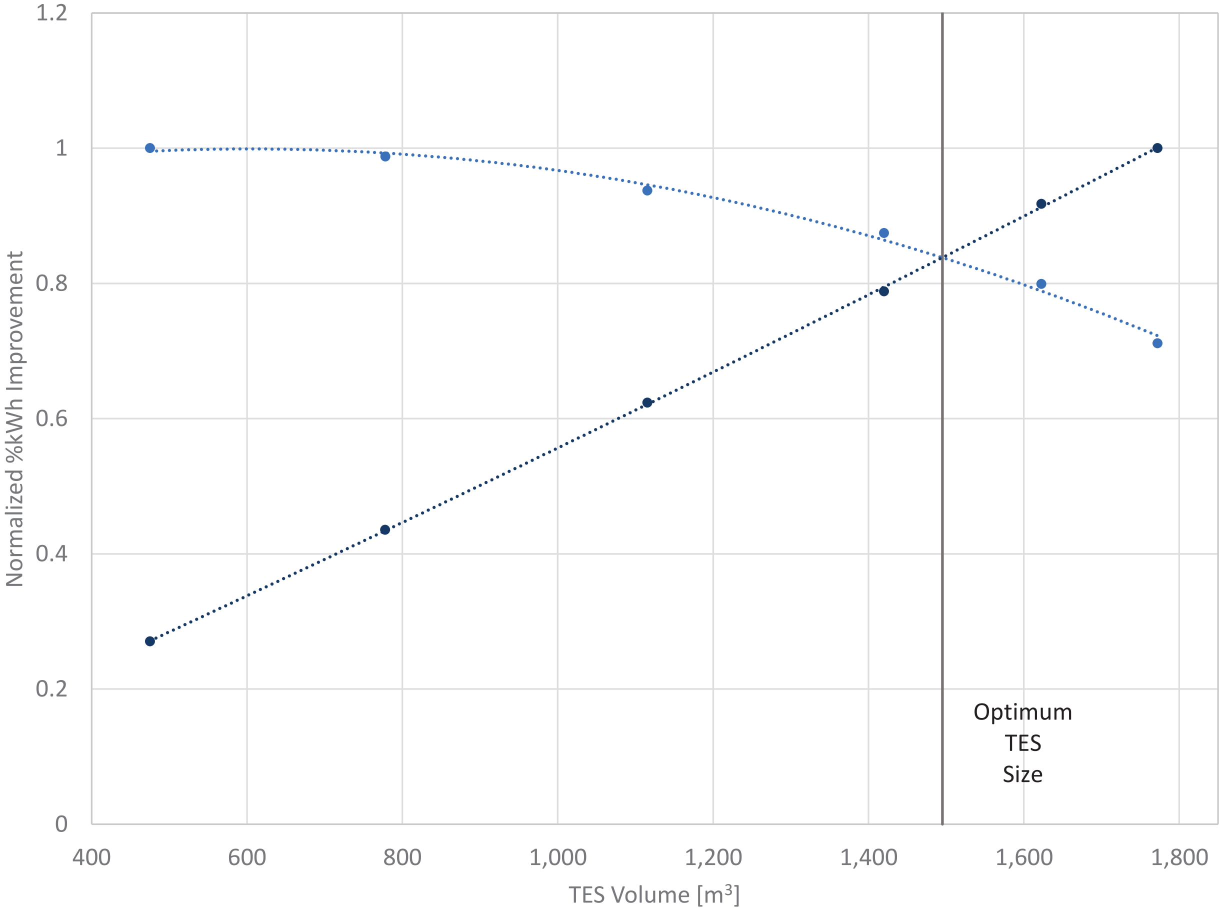

Figure 3.11: %kWh gained over extraction period and %kWh gained over day both normalized by their respective maximums vs. TES volume for PCM melting temperature of $T_m = 30°C$ in Las Vegas for average August day.

With the provided parameters of a PCM melt temperature of 30°C and an average daily August temperature curve from Las Vegas, it was found that the optimum extraction time for the precooling process with these parameters was approximately 8.68 hours.

After adjusting the parameters of the TES volume and its corresponding extraction time within the model, the August temperature curve from Las Vegas was input into the model. Once again, it is observed that the melt fraction curve shows that the PCM is nearly fully melted and refrozen throughout the day. During this shorter extraction window, the precooling process decreased the inlet air temperature to the steam condenser by about 6°C. This decrease in air temperature over the 8.68-hour extraction period increases the kWh produced during that time by 2.06% and increases the kWh produced throughout the entire day by 0.73%. These percentages correspond to a production gain of 9.0 MWh.

While the 2.06% gain of kWh over the extraction window is a significant increase in energy production during that time, the 0.73% gain of kWh over the day could be increased further. To achieve this goal, different melt temperatures were explored. Figure 3.12 shows the trends between percent kWh gained over the extraction period versus the TES volume for different PCM melt temperatures. These trends show that as the melt temperature is decreased, the same volume of the TES and same extraction time can lead to greater amounts of kWh gained over the extraction period.

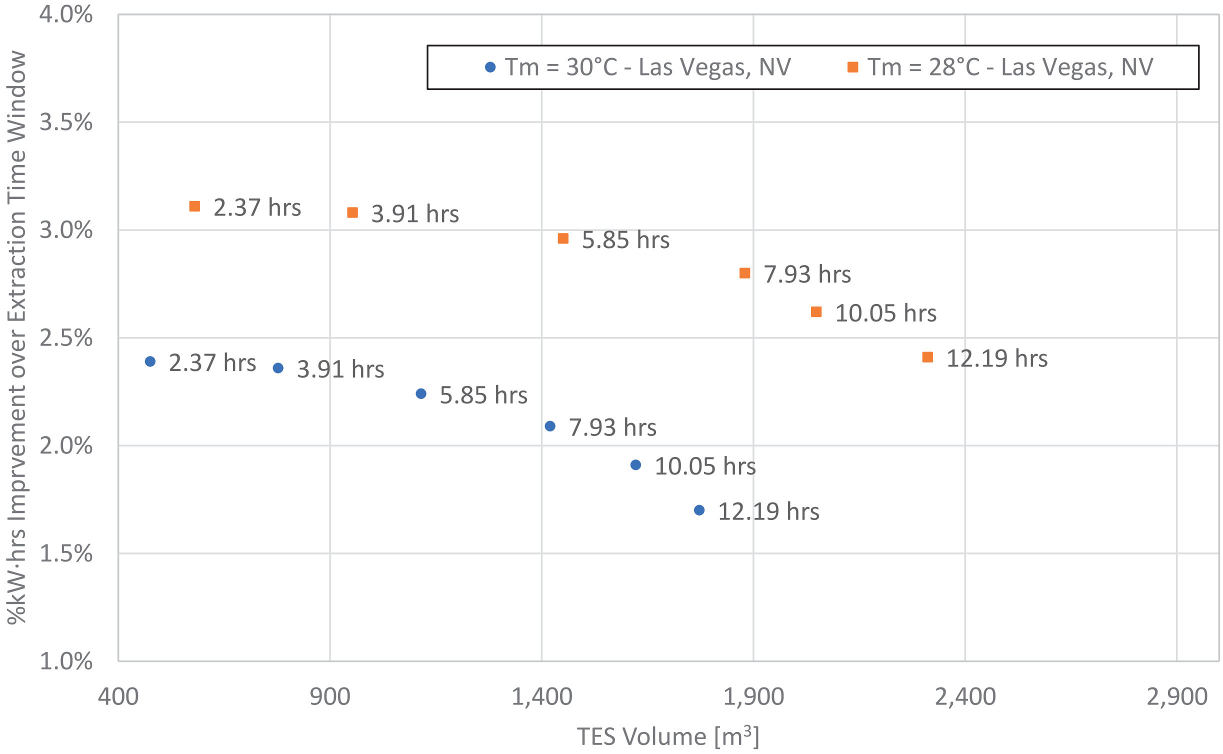

Figure 3.12: %kWh gained over extraction time for different extraction times vs. TES volume for two PCM melting temperatures in Las Vegas for average August day.

During the collection of this data, the model was once again adjusted to ensure that the PCM was being fully utilized throughout these extraction periods. To accomplish this full utilization, the amount of PCM as well as the flow rate per channel in the TES were adjusted such that the extraction and charging processes would reach 95% effectiveness. However, it was found that as the melt temperature was pushed lower and lower, the charging process could no longer support a 95% effectiveness due to the minimum temperatures not achieving low enough values for a long enough time to substantially refreeze the PCM. It was therefore

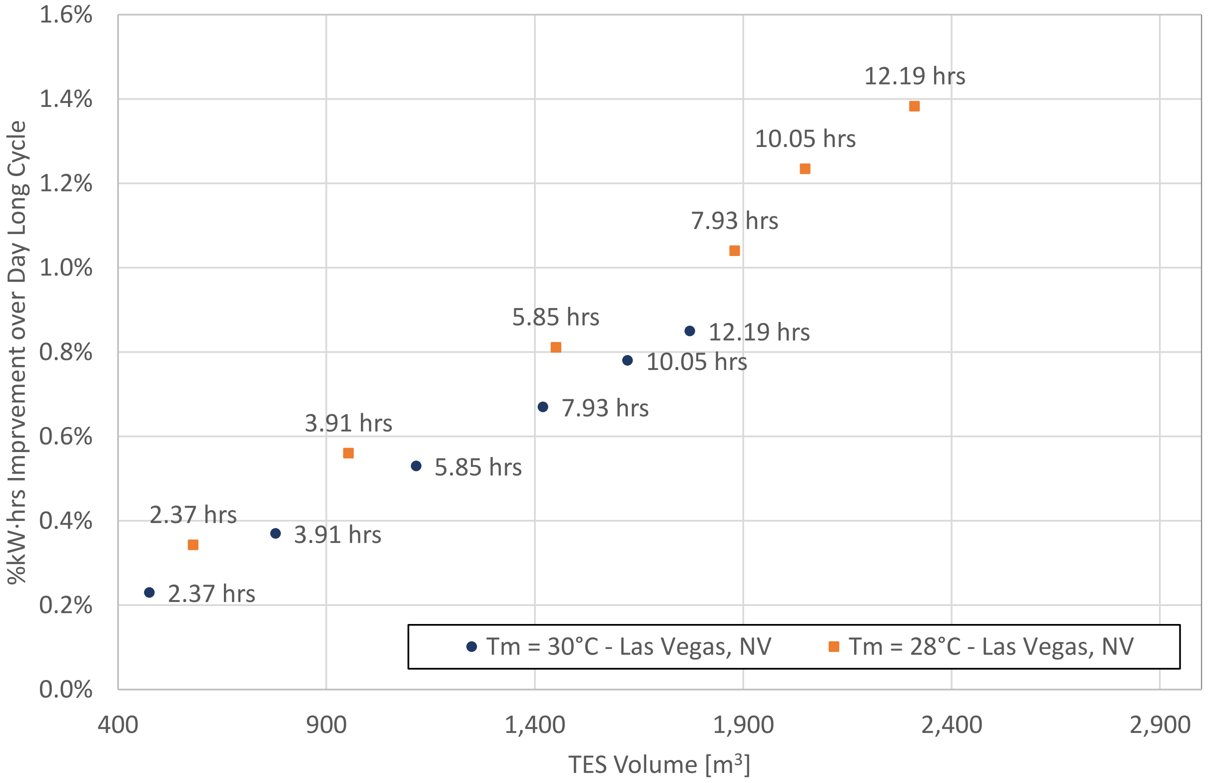

Figure 3.13: %kWh gained over day for different extraction times vs. TES volume for two PCM melting temperatures in Las Vegas for average August day.

determined that simply lowering the PCM melt temperature would not be enough to increase the gain in kWh production; the minimum temperature achieved throughout the day would have to be adjusted as well. This indicates that other locations should be considered, as was done in a related study [15].

## Financial Implications

Performing a cost analysis on the TES investment with optimized parameters, the savings achieved by the implementation of such a system as well as the payback time can be estimated. Project collaborators have estimated the cost of the TES to be \$15.19 per MJ of storage available. Using the model to calculate the total storage provided, we found that, for the optimized conditions, the Las Vegas TES would have a capacity of 814,410 MJ of storage. Using this value, we estimate that the initial capital investment of the TES in Las Vegas would be \$12.4 million.

For Las Vegas, the Southern Nevada Residential Single Family program could charge a premium rate of \$0.44 per kWh of electricity. Multiplying this pricing rate with the previously calculated optimized production gains in kWh per day for Las Vegas, it is calculated that the TES would provide revenue of ∼ \$4000 per day. Therefore, it would take approximately 28 years to pay back the initial capital investment of \$12.4 million for the TES in Las Vegas. This payback time estimation assumes that the TES is in use daily with consistent efficiency during the summer months of June through September. We expect all of the excess profit resulting from the implementation of the TES system is used as the only source of payment and account for continuously compounding interest at a rate of 10%. There would, of course, also be additional costs associated with heat exchanger and pump investments that would be required to support the TES system. These are not included here. It is also noted that the electricity cost estimation is limited to residential applications; however, similar estimations can be performed for commercial applications with comparable conclusions.

### Environmental Implications

The motivation behind the described modeling is the high usage of water at power plants. Traditionally, steam produced by thermo-electric power plants is cooled by passing it over an array of pipes filled with cold water, thereby caushing the steam to condense. This process is highly water intensive and uses between 730 and 830 gal/MWh [49]. Not only is this cooling method impractical in areas where water conservation is an issue, but it also causes irreparable damage to many rivers and reservoirs. To replace this process with a more sustainable one, the research described in this dissertation aims to show proof of concept air cooling technology using phase change thermal storage that could potentially reduce water usage at power plants. There is no plan in place to make this technology a reality in full scale power plants at this time. If this technology could be implemented in power plants worldwide, it could make a dramatic impact on water conservation efforts and facilitate the restoration of water sources for cities around the world.

## 3.7 Conclusions

The goal of this study was to use a model of TES in conjunction with a subsystem that utilizes cold storage to precool the air flow for a power plant air-cooled condenser during peak daytime air temperatures. This model was used to explore the parametric effects of changing PCM melt temperature and the energy storage and extraction control settings for the system. The subsystem model was also computationally linked to a model of Rankine cycle power plant performance to predict how much additional power the plant could generate as a result of the asynchronous cooling augmentation provided by this subsystem.

With this multi-scale modeling, the performance of the TES unit was examined within the context of a larger subsystem to illustrate how a high efficiency, optimized design target could be established for specified operating conditions. By adjusting the flow rate within the fluid flow passages and the volume of the TES to achieve specified melting of the PCM during a set extraction time, the percent increases in kWh over the extraction period and day were calculated for various extraction times. The percentage increase in kWh over the extraction period ranged from 1.75% to 3.75%, and the percentage increase in kWh over a day ranged from 0.25% to 1.35%. Variance in these percentages depend on location, daytime high and nighttime low temperatures, and extraction time.

Peak power output enhancements were observed to occur when the system operated in the extraction phase during limited hours near the peak temperatures experienced throughout a day, while total kWh enhancements were shown to increase as the extraction period increased.

Obtaining the optimal amount of PCM for both the percent kWh increase over the extraction period and the percent kWh increase over a day, the results suggest that for a full-sized power plant with a nominal capacity of 50 MW, the kWh output of the plant can be increased by up to 3.25% during the heat input/cold extraction period and up to 1.18% over a 24 hour period, depending on parameter choices. For these optimized conditions, cost analyses were performed, and it was estimated that the TES system has the potential to provide additional revenue of up to $\sim$ $4000 per day for Las Vegas. With initial investments for the PCM and TES structures adding up to $12.4 million in Las Vegas, the payback period was estimated to be 27 years.

Results obtained to date are not fully optimized, and the results suggest that with further adjustments in system parameters, weather data input, and control strategies, the predicted enhancement of the power output can be increased above the results in the initial performance predictions reported here.

# Chapter 4

# Model Validation

## 4.1 Introduction

A number of earlier investigations have developed modeling methods for thermal storage [43, 4, 25, 12, 7, 3, 48]. Earlier analyses of phase change thermal storage have generally modeled specific details of heat transfer in the storage unit structure. Most are either strictly analytical, numerical, or experimental. Alkilani et. al conducted a theoretical investigation of output air temperature of an indoor heater which utilizes a PCM heat exchanger [3]. Tay et. al used an $\varepsilon$-NTU method to generate an analytical solution to track latent heat transfer in a thermal storage device [48]. Ismail and Goncalves explored a two-dimensional model of a tube immersed in PCM [25]. By defining an appropriate control volume, the authors employ a finite difference scheme to characterize how the TES melt fraction, number of transfer units (NTU), and effectiveness are dependent on various parameters. Others combine analysis with computational research techniques, though few have experimental data available with which to validate their work. Shamsundar et. al look at a three-dimensional shell and tube configuration both analytically and numerically (via finite difference) in which the working fluid temperature changes axially as heat is transferred from the PCM [43]. As is clear from these examples, there is a need for experimental comparison that validates the many closed form solutions as well as computational results that researchers have generated.

The methodology and results that are presented in this paper are built upon a larger body of work I have helped to build over the last several years [21, 22, 50, 23, 15]. The first of these contains the derivation of a non-dimensional framework developed in order to analyze thermal energy storage technology with details reproduced in Chapter 1 [21]. From there, efforts were focused on quantifying the space and time varying conductance inherent in the transient melting and freezing processes of latent thermal storage as described in Chapter 2. That work was used to justify the use of an average conductance in future modeling; the effectiveness of high performance devices is not sensitive to variations in conductance [22]. Additional work has been done since then to determine a simpler relation for average conductance as a function of the melt fraction [50]. In tandem, the TES device was examined in the context of a larger subsystem, consisting of external heat exchangers used to input and reject heat to and from the storage. This problem, outlined in Chapter 3, was mathematically challenging by introducing spatially varying initial conditions (due to the nature of cyclic melting and freezing processes) as well as a transient boundary condition (for the varying working fluid temperature from the heat exchangers) [23]. The system equations derived in this paper were applied to model the performance of a power plant using TES for asynchronous cooling of a Rankine cycle steam condenser [15]. This paper demonstrated the economic viability of thermal storage. All that remains is to validate the numerical framework used in these previous explorations.

In earlier studies, there is little to no experimental data with which to validate numerical models. The culmination of previous work provides a great basis for comparison with experimental testing of a TES device. Thus, the primary objective of this chapter is to compare the results of numerical simulations to experimental data collected by project collaborators.

## 4.2 Computational Methodology

### Numerical Framework

In order to solve the differential equations numerically, we use a first order accurate finite difference approximation, employing the upwind and forward Euler discretization methods respectively. The temperature and melt fraction fields in the storage matrix are determined using these equations. This working fluid temperature, $\phi$, is dictated by:

$$\phi_j^{n+1} = \phi_j^n + \Delta t^* \Big[ N_{tu}(\theta_j^n - \phi_j^n) \Big] - \frac{\Delta t^*}{\Delta \hat{z}} \Big[ \phi_j^n - \phi_{j-1}^n \Big] \tag{4.1}$$

This equation is first order in time and space, necessitating a boundary and an initial condition. The working fluid exchanges heat with phase change material in the storage matrix which undergoes both sensible and latent heat transfer depending on the temperature of each discrete node. Sensible energy storage occurs when a cell containing PCM at position $j\Delta\hat{z}$ and time $n\Delta t^*$ is not at its melt temperature, $\theta_m$. The storage matrix temperature at the next time step can be determined via:

$$\theta_j^{n+1} = \theta_j^n + \Delta t^* \Big[ N_{tu} R_{we} (\phi_j^n - \theta_j^n) \Big] \quad ; \quad x_{e,j}^{n+1} = x_{e,j}^n \tag{4.2}$$

for $\theta_j^n \neq \theta_m$ and $x_{e,j}^n = 0$ or $x_{e,j}^n = 1$.

If Eqn. 4.2 would result in the temperature at the next time step, $n+1$, to pass the melt temperature, then $\theta_j^{n+1}$ is set to $\theta_m$ and latent energy storage begins, with change in melt fraction calculated from Eqn. 4.3:

$$x_{e,j}^{n+1} = x_{e,j}^n + \Delta t^* \Big[ N_{tu} R_{we} \mathrm{St}_{\mathrm{io}} (\phi_j^n - \theta_j^n) \Big] \quad ; \quad \theta_j^{n+1} = \theta_j^n \tag{4.3}$$

for $\theta_j^n = \theta_m$ and $0 < x_{e,j}^n < 1$.

The equations governing the storage matrix temperature and melt fraction are first order in time but have no spatial derivative. As such, only one boundary condition is required to solve these coupled first order differential equations. In $\hat{z}$:

$$\text{At } \ \hat{z} = 0 : \ \ \phi^{n}_{j=1} = \phi_{wi}(t^*) \tag{4.4}$$

$$\text{for } t^* > 0.$$

Initial conditions on temperatures, $\phi$ and $\theta$, and melt fraction, $x_e$, are also required for the entire domain. These can represent any distribution desired as in Eqn. 4.5:

$$\text{At } \ t^* = 0 : \ \ \phi^{n=1}_{j} = \phi_0(\hat{z}) \ , \ \theta^{n=1}_{j} = \theta_0(\hat{z}) \ , \ x^{n=1}_{e,j} = x_{e,0}(\hat{z}) \tag{4.5}$$

$$\text{for } 0 \leq \hat{z} \leq 1.$$

These initial and boundary conditions can be spatially uniform and temporally steady. To capture physical complexity, the initial conditions can be modified to match the end and beginning of subsequent processes; the boundary condition can be adjusted to capture time-varying conditions as demonstrated in Chapter 3. The temperature and melt fraction fields should be resolved spatially and temporally until the melting or freezing process end time, $t^*_{end}$, is reached. In order to determine device performance at $t^*_{end}$, we evaluate device effectiveness, $\varepsilon_{tes}$, described in Chapter 1.

## 4.3 Analytical Validation at Short Times via Closed Form Solution

We consider solution of the TES performance equations for a TES unit starting uniformly at temperature $T_0 = T_e = T_w = T_m$ and initial melt fraction $x_e = x_{e,0}$. The equations will be non-dimensionalized with $T_{min} = \min(T_0, T_{wi})$ and $T_{max} = \max(T_0, T_{wi})$ substituted into the previous definition for $\theta$, $\phi$, and $\mathrm{St_{io}}$. Because of the initial conditions, $\theta = \theta_m = 0$ everywhere and at all times of interest here, modifying the differential equation for $\phi$ to:

$$\frac{d\phi}{d\hat{z}} = -N_{tu}\phi \tag{4.6}$$

Note that before the transient starts, $\phi = \theta_m = 0$ everywhere. During the first residence time ($t \leq t_{res}$ or $t^* \leq 1$), a wavelike step change in $\phi$ propagates downstream. We can integrate the above differential equation from the inlet to the local $z$ location of interest noting that the definition of $\phi$ dictates that $\phi = 1$ at $\hat{z} = 0$. Integration of the equation leads to

$$\phi = e^{-N_{tu}\hat{z}} \tag{4.7}$$

This is the solution for $\phi$ for all times beyond the step-change front passage (as long as $\theta = \theta_m = 0$ everywhere). During the transient, each segment will only begin transferring heat and changing the melt fraction after the front passes when $t^* \geq \hat{z}$.

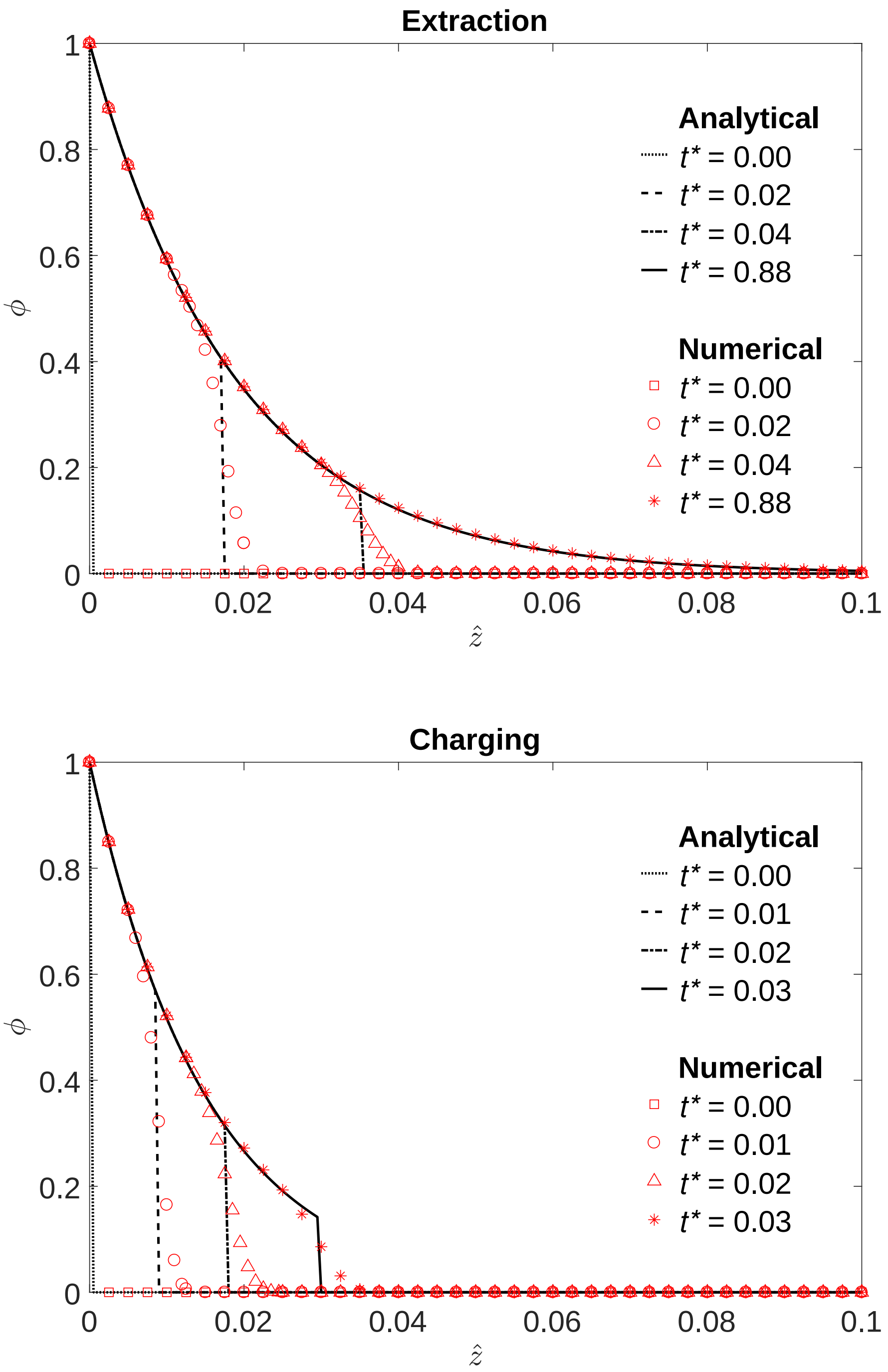

Figure 4.1: Comparison of analytical and numerical $\phi$ during extraction and charging ($N_{tu} = 52.88$, $R_{we} = 0.47$, $\mathrm{St}_{\mathrm{io}} = 0.05$).

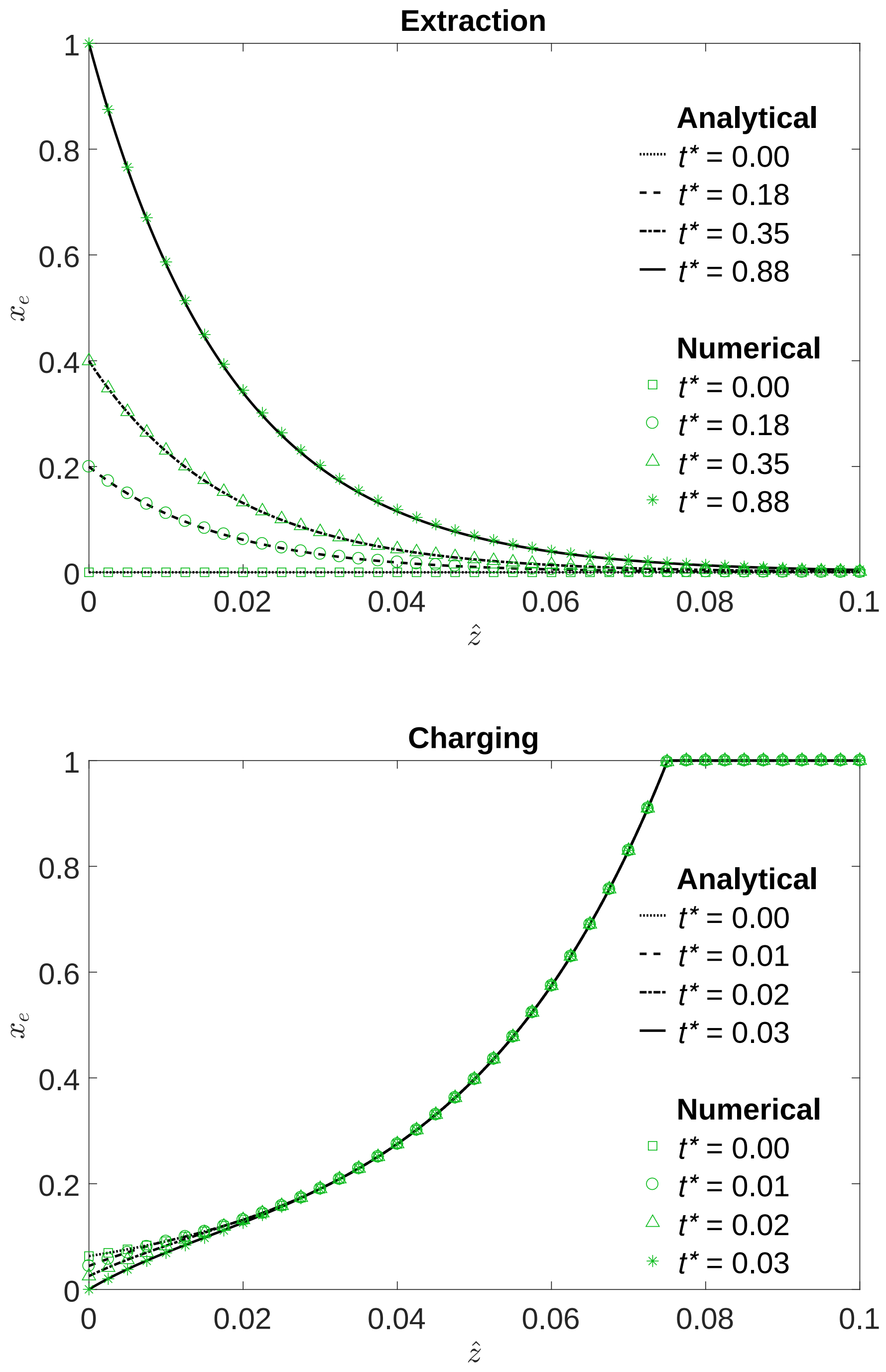

Figure 4.2: Comparison of analytical and numerical $x_e$ during extraction ($N_{tu} = 52.88$, $R_{we} = 0.47$, $\mathrm{St}_{\mathrm{io}} = 0.05$).

For these conditions, the energy balance equation for the PCM matrix reduces to

$$\frac{\partial x_e}{\partial t^*} = \pm N_{tu} R_{we} St_{io} \phi \tag{4.8}$$

where (+) applies to extraction and (-) applies to charging. This sign convention is used to properly account for the increasing or decreasing PCM melt fraction over time.

Substituting for $\phi$ using Eqn. 4.7 and integrating this equation with respect to time using the initial condition of $x_e = x_{e,0}$ at a given $\hat{z}$ location for time $t^* = \hat{z}$ yields

$$x_e - x_{e,0} = \pm N_{tu} R_{we} \mathrm{St_{io}} (t^* - \hat{z}) e^{-N_{tu}\hat{z}} \tag{4.9}$$

Thus, for this either process, the solutions are:

$$\phi = 0 \quad ; \quad x_e = x_{e,0} \tag{4.10}$$

before the step change front passes ($t^* < \hat{z}$) and

$$\phi = e^{-N_{tu}\hat{z}} \quad ; \quad x_e = x_{e,0} \pm N_{tu} R_{we} St_{io} (t^* - \hat{z}) e^{-N_{tu}\hat{z}} \tag{4.11}$$

after the step change front passes ($t^* \geq \hat{z}$). For the melting transient, these solutions are valid until $x_e = 1$ at the inlet location, $\hat{z} = 0$. Setting $x_e = 1$ and $\hat{z} = 0$ and solving for $t^*$ yields the $t^*$ value $t^*_{end}$ at which the validity of the model ends for extraction.

$$t^*_{end} = \frac{1 - x_{e,0}}{N_{tu} R_{we} St_{io}} \tag{4.12}$$

For the freezing transient, the heat flow is in the opposite direction (from the PCM to the fluid). During charging, these solutions are valid until $x_e = 0$ at the inlet location, $\hat{z} = 0$. Setting $x_e = 0$ and $\hat{z} = 0$ and solving for $t^*$ yields the $t^*$ value $t^*_{end}$ at which the validity of the model ends.

$$t^*_{end} = \frac{x_{e,0}}{N_{tu} R_{we} St_{io}} \tag{4.13}$$

For these short times of interest, we can compare the analytical and computational solutions in order to validate the numerical methods employed in this paper.

The working fluid temperature, $\phi$, is fairly consistent between the numerical (approximated) and analytical (exact) solution as seen in Fig. 4.1. The two differ in treatment of the step change front. The exact solution exhibits a vertical drop in temperature, as the information from upstream has not yet reached the location downstream. The numerical scheme cannot handle such discontinuities and smears the solution around the shock. This is purely an artifact of the numerics and can be improved by using a finer grid, or employing a different numerical scheme while solving the differential equations.

Error analysis, provided in Figure 4.3, shows that the difference between the numerical and analytical values scales approximately with spatial step size, $h$, which is consistent with the first-order numerical methods used for this problem.

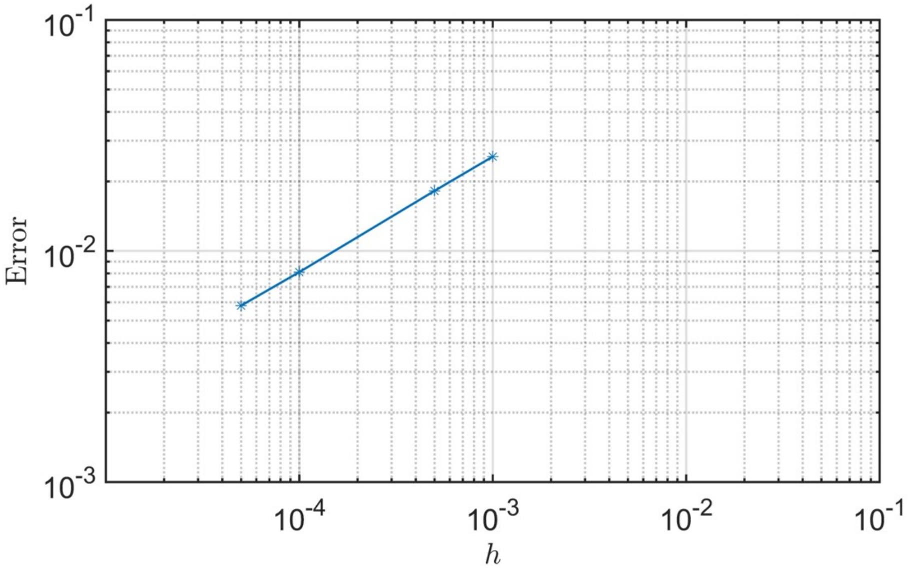

Figure 4.3: Comparison of numerical result to analytical solution for $x_e$; slope is $\sim$ 1.17.

$$||x_{e,numerical}(\hat{z}) - x_{e,analytical}(\hat{z})||_2 \sim h \tag{4.14}$$

It should be noted that the order of time step size, $k$, is on the order of the smallest spatial step, $h_{min}$, for stability. Specifically, the homogeneous form of Equation 4.1, without the $N_{tu}(\theta - \phi)$ source term, satisfies the Courant-Friedrichs-Lewy (CFL) condition that:

$$\frac{\Delta t^*}{\Delta \hat{z}} \leq 1 \tag{4.15}$$

Despite the error introduced in $\phi$ while attempting to capture the physics of the step change front, the solution of $x_e$ is compelling. As evidenced by Fig. 4.2, the numerical and analytical solutions are almost indistinguishable from each other. This comparison with the closed form analytical solution provides necessary validation of our numerical method as well as understanding of the physics governing the TES device performance.

## 4.4 Experiment Design

The remainder of this paper is dedicated to applying the methodology and numerical framework described above to a 100 kJ TES device. A compact heat exchanger (CHX) was fabricated and assembled by a commercial vendor (Allcomp Inc.) and subsequently filled with a phase change material. The working fluid, i.e. the heat transfer fluid (HTF), was used to melt and solidify the PCM in repeated thermal cycles involving complete solidification and incomplete melting; this technique is called the "cold finger" approach. The TES has an offset fin configuration on the working fluid side and aluminum porous fins in the storage matrix. The device has five flow channels for HTF flow and four hermetically sealed channels with encapsulated PCM. Experimental testing of this prototype was performed at Texas A&M. In previous chapters, device geometry, material properties, and operating conditions were summarized in a single table as input parameters. Here, each of these will be described in greater detail to emphasize the experimental design.

## Device Geometry

The TES prototype consists of stacked rectangular sections, alternating between flow passages and storage matrix sections. The unit was fabricated using mature fin forming and vacuum brazing processes. The liquid-side heat transfer surface is a 3003 aluminum offset fin, while the PCM-side utilizes a high density plain fin formed from 5056-O aluminum wire mesh. The TES HX core is comprised of four PCM cavities that are sandwiched between five liquid cooling passages. Header caps were bonded to the TES HX core to support cyclic testing. Note that assembly of a unit for mass production would employ a more robust joining technique such as welding.

The HTF region of the TES had an offset fin density of 22 fins per inch, selected due to its high surface area. The PCM channels are brazed with aluminum foam which can be thought of as porous fin. These porous fins were formed by folding an aluminum wire based sheet. The purpose of the aluminum foam is to enhance the effective thermal conductivity of PCM.

The design is somewhat anisotropic, with outer working fluid channels only interacting with one PCM cavity each, as illustrated in Figure 4.4. This results in different charging and discharging rates in the center PCM channels than the top and bottom PCM channels. To mitigate the impact of this in the model, the bulk working fluid temperature at the inlet and the outlet is chosen as the variable for comparison.

Specific details of the design are summarized in Table 4.1. Of particular interest is the void fraction which greatly impacts the effective properties that form the dimensionless parameters in the governing equations [2].

## Thermophysical Properties

There are four types of phase change materials that might be used in this type of application: organic paraffins, organic non-paraffins, inorganic salt hydrates, and inorganic metal eutectics [30]. Organic paraffins have a high latent heat of fusion but are derived from petroleum. Organic non-paraffins are not derived from petroleum but tend to be very expensive. Inorganic salt hydrates are very cheap but but unfortunately are unstable over repeated cycling. All of the above suffer from low thermal conductivity which makes the process of inputting or removing energy from the PCM more difficult. This can be remedied with an inorganic metal eutectic which has excellent thermal conductivity but a lower latent heat of fusion than other materials. When selecting an appropriate PCM among these, affordability is

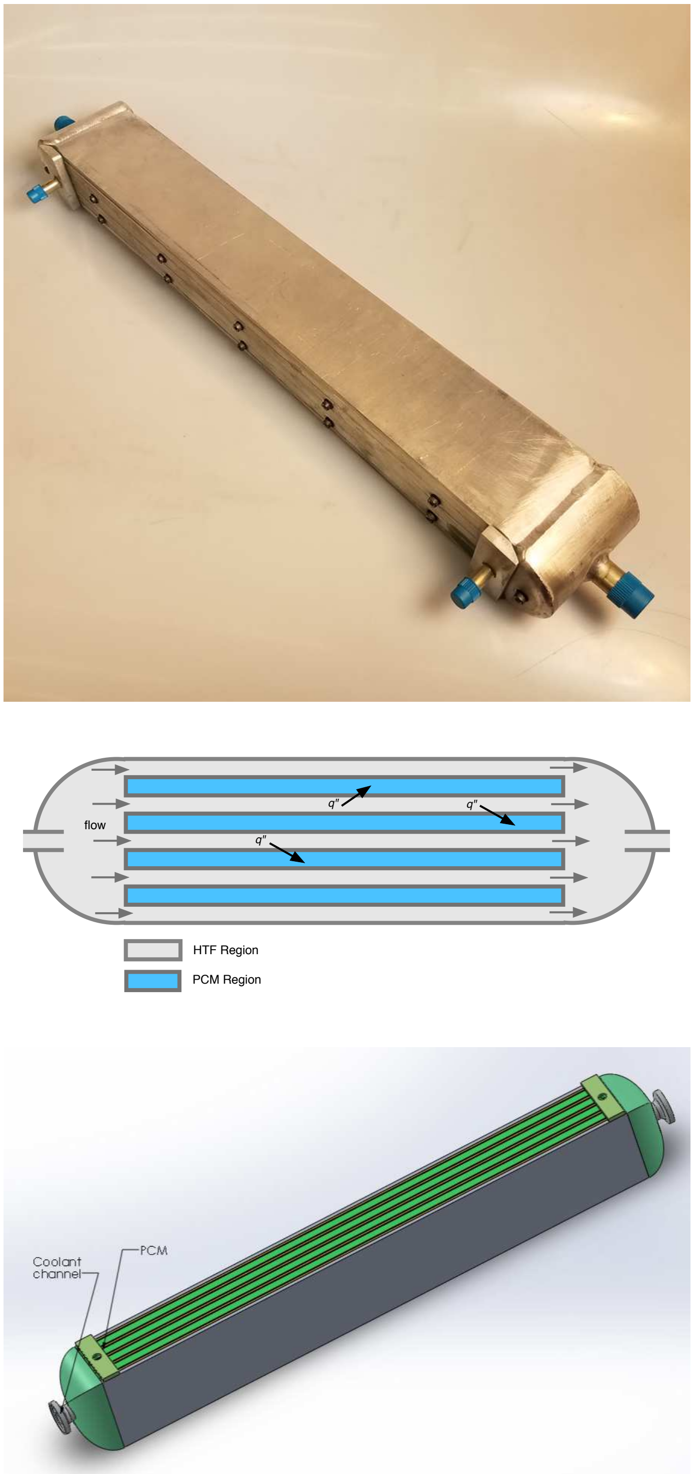

Figure 4.4: Photograph, schematic (not to scale) illustrating heat flux (q″) from hot HTF region into PCM region during melting process, and CAD drawing of TES device.

Table 4.1: Geometry specifications for prototype thermal storage performance calculations.

Device Geometry

| | | |
|---|---|---|
| Length of TES device, $L$ | 0.407 | m |
| Wetted perimeter of flow passage, $s_w$ | $9.42 * 10^{-2}$ | m |
| Cross sectional area of flow passage, $A_c$ | $8.97 * 10^{-5}$ | $\mathrm{m}^2$ |
| Matrix volume per unit flow length, $\nu'$ | $1.99 * 10^{-4}$ | $\mathrm{m}^2$ |
| Number of working fluid channels, $N_{wf}$ | 5 | |
| Number of PCM storage matrix sections, $N_{pcm}$ | 4 | |
| Void fraction in storage matrix, $\varepsilon_s$ | 0.729 | |

highly important. With all of these factors in mind, the material chosen for the prototype was lithium nitrate trihydrate, a salt hydrate that has been optimized to better handle transient cycling [42]. Anhydrous lithium nitrate salt powders were procured commercially from Beantown Chemical with purity $> 99\%$. Thermophysical properties are shown in Table 4.2.

The amount of PCM inserted into the TES was 474 grams. The latent heat of LNT was measured in this study to be 278 kJ/kg using the T-History method [29]. Thus, the theoretical energy storage capacity of the device was rated to be 130 kJ which differs slightly from the rated capacity of 100 kJ.

Other properties that are not solely associated with latent heat transfer can be adjusted by adding a metal mesh to the storage matrix. As the thermal conductivity of lithium nitrate trihydate is quite low, a metal matrix structure is required to effectively conduct heat through the storage matrix. Any high conductivity material would be suited for this application, but the low cost of aluminum makes it ideal for this technology. Material properties are shown in Table 4.2. Note that the phase change material melt temperature, $T_m$, experimentally deviates from the single reported value due to the subcooling or superheating required to initiate phase change.

Aluminum is an cheap option that is chemically compatible with the PCM. Metal pathways are ideal for spreading the thermal energy away from the channel wall towards the melt front [51, 18]. They enhance the effective properties (conductivity, density, specific heat) of the storage matrix which are calculated according to:

$$\bar{p} = p_m(1 - \varepsilon_s) + p_{pcm}\varepsilon_s \tag{4.16}$$

The thermophysical properties of the working fluid are also necessary in order to solve the governing equations. The experiments were conducted with pure de-ionized water. Its properties were taken at the inlet temperatures for extraction and for charging respectively. The ranges in Table 4.2 reflect the values associated with the cold and hot fluid inlet temperatures.

Table 4.2: Material specifications for prototype thermal storage performance calculations.

Material Properties (LNT)

| | | |
|---|---|---|
| thermal conductivity, $k_{pcm}$ | 0.584 | W/mK |
| density, $\rho_{pcm}$ | 1500 | kg/m$^3$ |
| specific heat, $c_{p,pcm}$ | 2910 | J/kgK |
| latent heat of fusion, $h_{ls}$ | 278 | kJ/kg |
| melting temperature, $T_m$ | 30 | °C |

Material Properties (Al 5056)

| | | |
|---|---|---|
| thermal conductivity, $k_m$ | 117 | W/mK |
| density, $\rho_m$ | 2640 | kg/m$^3$ |
| specific heat, $c_{p,m}$ | 910 | J/kgK |

Material Properties (Effective)

| | | |
|---|---|---|
| effective thermal conductivity, $k_e$ | 32.1 | W/mK |
| effective density, $\rho_e$ | 1810 | kg/m$^3$ |
| effective specific heat, $c_{p,e}$ | 2370 | J/kgK |

Material Properties (Water)

| | | |
|---|---|---|
| thermal conductivity, $k_w$ | 0.608 - 0.623 | W/mK |
| density, $\rho_w$ | 994 - 997 | kg/m$^3$ |
| specific heat, $c_{p,w}$ | 4090 - 4130 | J/kgK |

## Experimental Apparatus and Procedure

The melt front and freeze front of the PCM in the top and center channels were monitored by embedding thermocouples at predefined locations. The predefined locations correspond to 10%, 30%, 50%, 70%, and 90% melt fractions along the axial directions as illustrated in Figure 4.5. The temperature of the HTF was measured at the inlet and outlet plenum of the compact heat exchanger.

Two different HTF flow configurations were explored during solidification and melting to study the efficacy of cold finger techniques. Cold finger techniques involve thermal cycling protocols with complete solidification and incomplete melting of the PCM samples under consideration. The incomplete melting protocols enable a residue of PCM crystals to remain in the PCM sample that act as nucleators by promoting nucleation. Prior studies have shown that having an un-melted portion of the PCM, like residue crystals, provides better efficacy

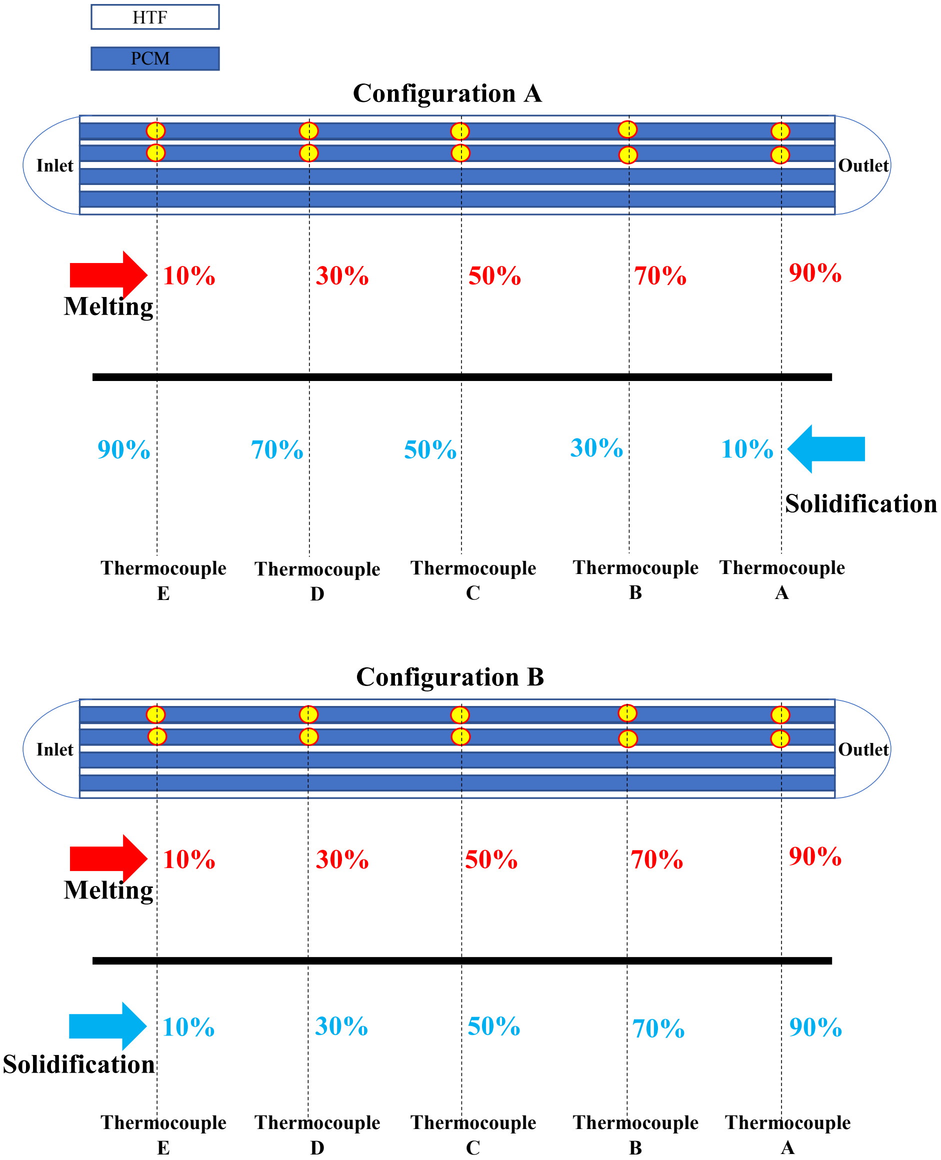

Figure 4.5: Schematic showing the location of thermocouples inserted in the TES for two different flow configurations.

for promoting nucleation than that of heterogeneous additives for the same purpose. The result is that freezing can initiate with subcooling less than 1 °C.

To realize the full effectiveness of the cold finger techniques, the experiments were designed for the flow of HTF in to the CHX to be bi-directional. In configuration A, the flow of HTF during melting is from left to right, whereas during solidification the flow of HTF was reversed to flow from right to left such that it flows in the opposite direction during charging and discharging. In configuration B, the flow of HTF during melting and solidification is from left to right such that it flows in the same direction during charging and discharging. For the complete melting and freezing tests, the flow direction matched configuation B, with both HTF flows in the same direction as shown in Fig. 4.5. For coldfinger, configuration A and B were both tested.

The cold finger experiments were designed for the melting to proceed until 90% of the total latent heat (i.e., the total energy storage capacity) was utilized, thus allowing about 10% of the remaining PCM to be un-melted and remain in solid phase as dispersed crystals or unused energy storage capacity. Thus, storage capacity is sacrificed marginally to enable more reliable operation by enhancing the efficacy of the residual un-melted crystals of the PCM to initiate the nucleation and subsequent propagation of the solidification front in the melted phase of the PCM. The variation in flow direction was manipulated with three-way valves with different valve configuration for melting and solidification.

The top PCM channel was used as the reference for monitoring the propagation of the melting front. The PCM charging and discharging temperature conditions were achieved using two different water baths. The hot water bath was maintained slightly above phase transition temperature at 35°C using a chiller unit and the cold water bath was maintained at a temperature below phase transition temperature at 25°C. The two water baths with chiller units were purchased from Cole-Parmer (Model: Polystat cooling/heating circulating baths, 2C15). Data was collected to indicate when 90% of the PCM was melted by hot HTF pumped into the TES from the hot water bath. At that point, the valves were switched to pumping of cooling HTF from the cold water bath to begin freezing the PCM. At this switch point, the PCM matrix section temperature recorded by the thermocouple at the 90% melt fraction location of top channel reached 30.5 °C. This allowed for maximization of the storage capacity and enabled the implementation of the cold finger technique.

The thermocouples utilized in the temperature measurements were K-Type (1/16" diameter) with hydro-thermic sheathed tips (Sheathing Material: SS 316, and Manufacturer: Temprel, Ohio). The tip of the thermocouple is located centrally along the width of the heat exchanger (1.5" from the edge). The thermocouples were calibrated in a water bath from 10 °C to 40 °C at an interval of 0.5 °C using an NIST standard thermometer. Its least count is ± 0.25 °C with calibration uncertainty of 0.8%, meaning that the most precise value that can be measured is to the quarter degree. After calibration, the uncertainty of the thermocouples was determined to be ±0.25 °C to ±0.35 °C.

A high-speed data acquisition (DAQ) system was used for recording the temperature measured by the thermocouples. The DAQ consists of an NI SCXI 1000 Chassis and an NI SCXI-1303 board. The temperature measurements were performed at 1 Hz frequency. The least count accuracy of DAQ system was 0.003 °C; therefore, the uncertainty from the DAQ can be considered negligible. Simultaneously, the voltage measurement from the flow meter was acquired using an NI USB 9162 DAQ at 1 HZ frequency. The HTF volumetric flow rate in the system was measured by an Omega FLR 1000 series flow meter (S/N 10981) which was calibrated for 0.2 L/min to 2 L/min (purchased from OMEGA).

The thermal performance of the TES was analyzed by varying (a) the flow rate of the HTF during charging and discharging, and (b) the inlet temperature of the HTF during charging and discharging. The volumetric flowrate was varied between 3 and 5 gallons per hour and the HTF inlet temperatures tested during melting were 33 °C, 35 °C, and 37.4 °C. Similarly, during solidification, the HTF inlet temperature was varied between 20 °C and 25 °C. The design condition for the compact heat exchanger was 3 gallons per hour with inlet temperature of 37.4 °C during melting (discharging) and 25 °C during freezing (charging). The experiments were repeated two times with and without insulation to ensuring repeatability of the experiments. The insulated and un-insulated cases allowed for comparison of parasitic heat loss to the environment during the melting and solidification process.

The experimental steps are listed as follows:

1. Initially solidify PCM with HTF at cold inlet temperature.
2. Close the cold HTF control valve and turn valves to direct the hot HTF.
3. Open the hot HTF control valve and melt to the 90% mass fraction of un-melted PCM.
4. Close the hot HTF flow control valve and turn valves to direct the cold HTF.
5. Completely solidify the PCM.
6. Repeat steps (2) through (5) above for ensuring repeatability and for varying HTF mass flowrate and inlet temperature.

The temperature difference of the HTF between inlet and outlet was computed as follows:

$$\Delta T_{HTF} = T_{outlet} - T_{inlet} \tag{4.17}$$

where $T_{outlet}$ is the HTF temperature measured at the outlet port of the heat exchanger and $T_{inlet}$ is the inlet temperature measured at the inlet port of the heat exchanger. The measurement uncertainty of the $\Delta T_{HTF}$ was estimated by using the following equation:

$$u_{\Delta T} = \left[ \left( \frac{\partial \Delta T_{HTF}}{\partial T_{outlet}} \right)^2 (u_{T_{out}})^2 + \left( \frac{\partial \Delta T_{HTF}}{\partial T_{inlet}} \right)^2 (u_{T_{in}})^2 \right]^{1/2} \tag{4.18}$$

where $u$ is the statistical uncertainty for each variable. The calibrated uncertainty of thermocouples was determined to be ± 0.35 °C between 10 °C and 40 °C. The nominal value for the measurement uncertainty for $\Delta T_{HTF}$ is therefore estimated to be ± 0.49 °C. The experimental effectiveness ($\varepsilon_{exp}$) of the TES was determined using the following equation:

$$\varepsilon_{exp} = \frac{T_{inlet} - T_{outlet}}{T_{inlet} - T_{PCM}} \tag{4.19}$$

where $T_{PCM}$ is the local temperature of the of the PCM. The thermal storage capacity of the heat exchanger at any instant was calculated by using Equation 4.20, based on the measurements of the HTF temperature values and mass flow rates:

$$E = m_w c_{p,w} \Delta T_{HTF} \tag{4.20}$$

where $m_w$ is the total mass flow over a short duration of the experiment and $c_{p,w}$ is the specific heat capacity of the HTF. The cumulative values of the instantaneous thermal energy storage can be used to estimate the total energy storage capacity of the TES for either the charging or discharging portion of the cycle. The instantaneous power, $P$, for the TES was calculated as follows:

$$P = \dot{m}_w c_{p,w} \Delta T_{HTF} \tag{4.21}$$

where $\dot{m}_w$ is the mass flow rate at any instant. The instantaneous power can be integrated over a specified time period and divided by the total time period in order to obtain the average power over the chosen time period. The experimental Stefan number ($\mathrm{St}_{exp}$) at any instant can be estimated using the following equation:

$$\mathrm{St}_{exp} = \frac{\text{(Sensible Heat)}}{\text{(Latent Heat)}} = \frac{c_{p,w} \Delta T_{HTF}}{h_{ls}} \tag{4.22}$$

where $h_{ls}$ is the latent heat of fusion of the phase change material.

## Model Transport Parameters

The total flow rates for extraction and charging were provided with TAMU experimental data. Due to a 4.3 % uncertainty reported in flow rate measurements, a slightly lower flow rate was input into the numerical model to account for any hydrodynamic losses. The total mass flow rate is assumed to be distributed equally among the 5 flow passages in the device.

Table 4.3: Operation specifications for prototype thermal storage performance calculations.

Operating Conditions

| | | |
|---|---|---|
| Mass flow rate for extraction, $\dot{m}_e$ | $3.44 * 10^{-3}$ | kg/s |
| Mass flow rate for charging, $\dot{m}_c$ | $3.56 * 10^{-3}$ | kg/s |
| Inlet temperature for extraction, $T_{wi,e}$ | 36 | °C |
| Inlet temperature for charging, $T_{wi,c}$ | 26 | °C |
| Extraction overall heat transfer coefficient, $\bar{U}_{e,1}$ | 2990 | $W/m^2K$ |
| Charging overall heat transfer coefficient, $\bar{U}_{c,1}$ | 2880 | $W/m^2K$ |
| Extraction overall heat transfer coefficient, $\bar{U}_{e,2}$ | 2980 | $W/m^2K$ |
| Charging overall heat transfer coefficient, $\bar{U}_{c,2}$ | 2930 | $W/m^2K$ |

The mass flow rates in the table correspond to 3 gallons per hour for de-ionized water at the average inlet temperatures shown. The working fluid in all tests came in at a relatively constant inlet temperature after being ramped up or down to that, respectively. The properties of the working fluid were assumed to be constant throughout a given process and determined based on the average water inlet temperature.

## Calculating Conductance

With the device geometry, thermophysical properties, and transport parameters specified, a convective heat transfer coefficient can be determined via correlation. The flow passages consist of offset fins, giving a Colburn-j type relation:

$$\begin{gathered} j = .6522 * \mathrm{Re}^{-.5403}\left(\frac{s}{h_f}\right)^{-.1541}\left(\frac{t_f}{l_f}\right)^{.1499}\left(\frac{t_f}{s}\right)^{-.0678} \\ \left(1 + 5.269 * 10^{-5}\mathrm{Re}^{1.340}\left(\frac{s}{h_f}\right)^{.504}\left(\frac{t_f}{l_f}\right)^{.456}\left(\frac{t_f}{s}\right)^{-1.055}\right)^{-.1} \end{gathered} \tag{4.23}$$

where Re is the Reynolds number of the flow, $s$ is the spacing between fins, $h_f$ is the height of the fins, $t_f$ is the thickness of the fins, and $l_f$ is the length of the fins.

The Colburn-j factor is used to calculate the Stanton number, which is subsequently used to calculate the Nusselt number, and from there, solve for the convective heat transfer coefficient, $h$:

$$\begin{aligned} \mathrm{St} &= \frac{j}{\mathrm{Pr}^{2/3}} \\ \mathrm{Nu} &= \mathrm{StRePr} \\ h &= \frac{k_w \mathrm{Nu}}{D_h} \end{aligned} \tag{4.24}$$

With $h$, the overall heat transfer coefficient, $U$, can be found based on methods from Chapter 2. The more elegant of these results will be used, namely that the overall heat transfer coefficient, $U$, can be found from the device geometry ($A_t$, $A_w$, $H_{pcm}$), thermophysical properties ($k_s$), convective coefficient, $h$, and the melt fraction, $x_e$, which is a function of position in the device as well as time:

$$U_e = \left[\frac{1}{h(A_t/A_w)} + \frac{H_{pcm}}{2k_s}x_e\right]^{-1} \tag{4.25}$$

where $A_t/A_w = (\eta_{\mathrm{fin}} h_f + s)/(s + t_f)$ including the offset fin efficiency, $\eta_{\mathrm{fin}}$, and height of the storage matrix sections, $H_{pcm}$.

A key finding from both studies of conductance was that an average $U$ could be used in place of a spatially and temporally varying one. To be sure that this was also the case for the prototype experiments, we applied a quasi-steady treatment of the variation of $U$ with $x_e$ and compared our results to constant conductance. As the conductance is quite high, we see no measurable difference in the fluid outlet temperature predicted. Thus, an average conductance is suitable for modelling the TES. In order to average Eqn. 4.25, we integrate over the range of $x_e$ encountered during the melting process.

$$\bar{U}_e = \frac{1}{x_{e,f}} \int_{x_{e,i}=0}^{x_{e,f}=1} \left[ \frac{1}{h(A_t/A_w)} + \frac{H_{pcm}}{2k_e} x_e \right]^{-1} dx_e \tag{4.26}$$

After integrating over melt fraction and normalizing by the final value, we find that:

$$\bar{U}_e = \frac{2k_e}{H_{pcm}} \ln \left[ 1 + \frac{H_{pcm}}{2k_e} h(A_t/A_w) \right] \tag{4.27}$$

This gives a value for $\bar{U}_e$ that falls between the convective heat transfer coefficient ($h$) and the steady state value reached at the end of melting that $U$ asymptotes to when the PCM melt front reaches the adiabat between flow passages. The key term in the variable $U$ expression, $x_e$, can be interpreted as a proxy for the growing distance between the channel wall and the melt front. This term is the dominant thermal resistance in the problem due to the high efficiency of the working fluid side heat transfer. By extrapolating this simple model to freezing, we predict the values given in Table 4.3 for TES conductance.

Table 4.4: Dimensionless input values for thermal storage performance calculations.

| | $N_{tu}$ | $R_{we}$ | $\mathrm{St}_{\mathrm{io}}$ |
|---|---|---|---|
| Run 1 Extraction | 32.4 | 0.534 | 0.234 |
| Run 1 Charging | 31.2 | 0.541 | 0.234 |
| Run 2 Extraction | 32.5 | 0.534 | 0.234 |
| Run 2 Charging | 30.4 | 0.541 | 0.234 |

This average overall heat transfer coefficient is subsequently used to calculate $N_{tu}$, the number of transfer units, required to solve the non-dimensionalized set of equations that comprise the numerical framework. The complete set of parameters in the three governing equations would be non-dimensionalized giving the values in Table 4.4.

## 4.5 Results and Discussion

Table 4.4 enables us to proceed with the solution of the differential Eqns. 4.1, 4.2, and 4.3 with boundary condition given by Eqn. 4.4 and initial conditions from Eqn. 4.5. This provides spatially and temporally resolved temperature and melt fraction fields.

Table 4.5: Time to complete melting and freezing processes for experimental run 1.

System Performance

| | | |
|---|---|---|
| Experimental melting completed: | 27.0 | min |
| Numerical melting completed: | 25.8 | min |
| Percent difference | **4.42** | % |
| Experimental freezing completed: | 85.2 | min |
| Numerical freezing completed: | 76.5 | min |
| Percent difference | **10.7** | % |

Four experimental tests were conducted at TAMU. Two of these consisted of complete melting and freezing while the others examined incomplete melting followed by freezing. This was done in an effort to combat the poor nucleation rates that resulted once the entire PCM domain was liquid. While all four tests are important, those with complete melting and freezing are most relevant for comparison to the numerical model. The metric used to determine whether or not the numerics effectively captures the physics is the process end time (e.g. time to melt, time to freeze). For Run 1, the completion times summarized in Table 4.5 were observed.

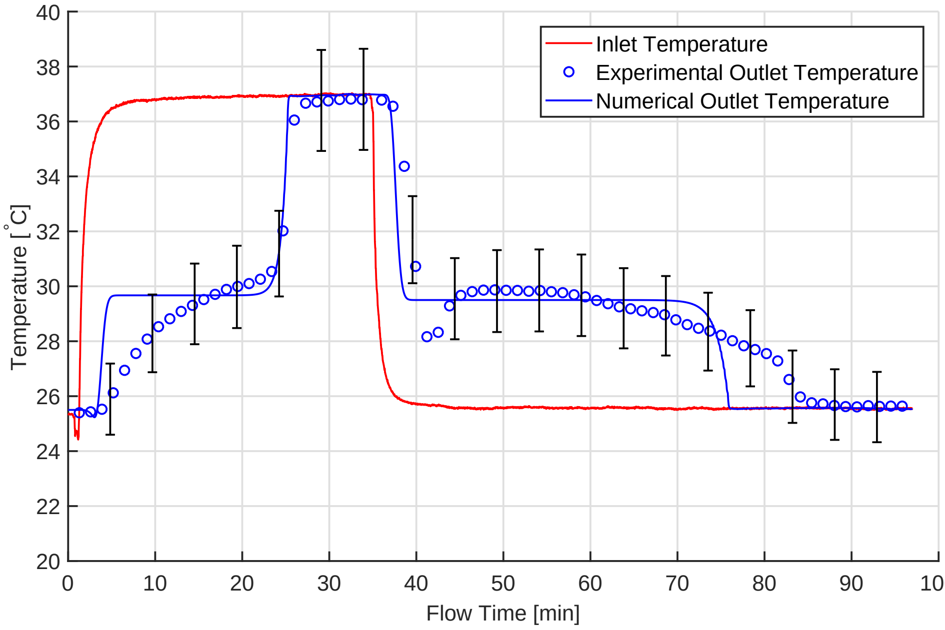

Figure 4.6: Complete melting and freezing results for experimental run 1.

*Note*: For extraction, the melt temperature was taken to be 29.66°C and for charging, the melt temperature was taken to be 29.5°C. These values are well within the range predicted by experiments.

Table 4.6: Time to complete melting and freezing processes for experimental run 2.

System Performance

| | | |
|---|---|---|
| Experimental melting completed: | 26.5 | min |
| Numerical melting completed: | 25.5 | min |
| Percent difference | **3.85** | % |
| Experimental freezing completed: | 89.5 | min |
| Numerical freezing completed: | 74.8 | min |
| Percent difference | **17.8** | % |

Run 2, with transient inlet and outlet temperatures reproduced in Fig. 4.7, generated similar results to Run 1. There are several key takeaways from the comparison of the experimental and numerical inlet and outlet temperature measurements.

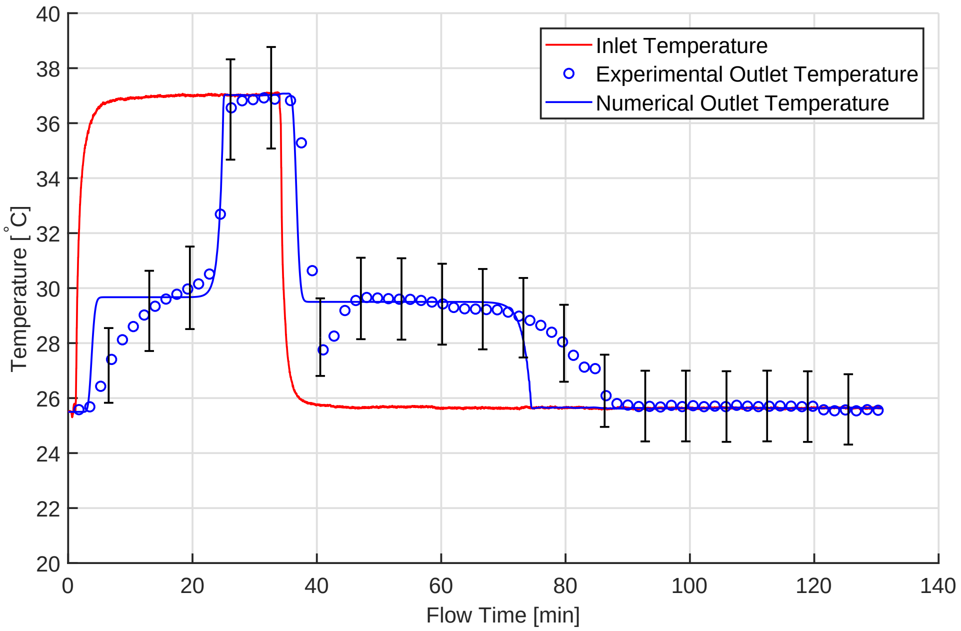

Figure 4.7: Complete melting and freezing results for experimental run 2.

It is challenging to capture the exact heat transfer physics with the computational program. This is evidenced by disagreement between the curves below the melt temperature for both extraction and charging. However, this disagreement falls mostly within the 5 % uncertainty associated with temperatures measured in the experiment. Where the numerical prediction does not fall within error bars, the absolute difference between experimental measurement and numerical prediction is around one to two degrees Celsius. This lends significant support to the accuracy of the model prediction. Even more importantly, the process completion time is quite close, ranging between 4 and 18 % difference. The highest discrepancy is observed during freezing. There, the numerical program is not designed to capture the poor nucleation rates that necessitate subcooling (at ∼ 40 minutes) before the phase change material can start freezing.

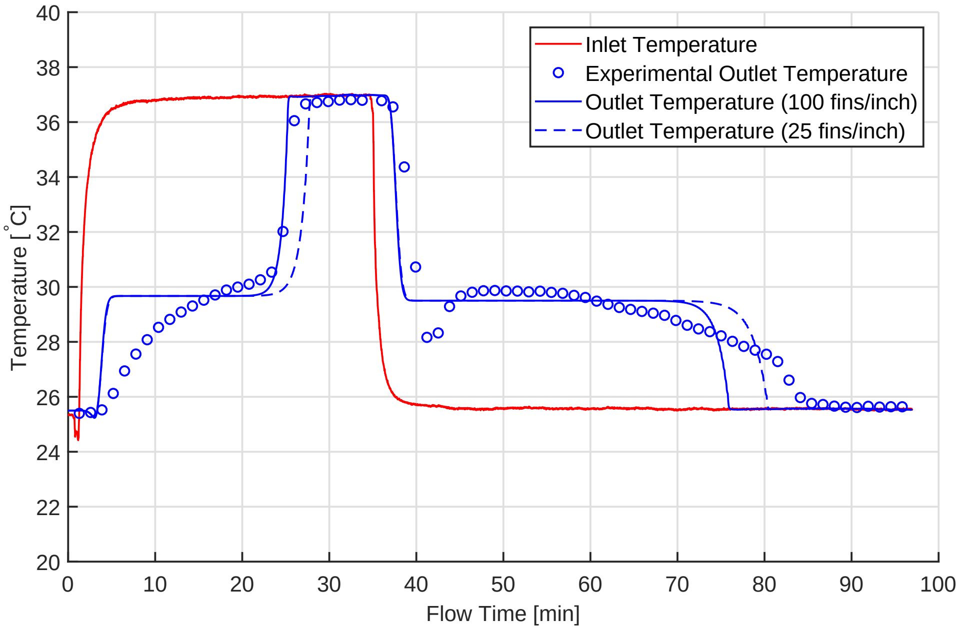

Figure 4.8: Complete melting and freezing predictions with fin design modifications.

Due to the accuracy with which the computational model can be used to predict process completion times, it can be used as a highly efficient and cheap design tool. For example, the number of fins per inch within the storage matrix sections can be reduced, thereby increasing the void fraction, and decreasing the overall heat transfer coefficient.

Table 4.7: Design modifications for run 1 impacting overall heat transfer coefficient, $\bar{U}$.

| | 25 fins/inch | 100 fins/inch | |
|---|---|---|---|
| Run 1 Extraction, $\bar{U}_{ext,1}$ | 2520 | 2990 | W/m$^2$K |
| Run 1 Charging, $\bar{U}_{char,1}$ | 2440 | 2880 | W/m$^2$K |

To maintain a consistent amount of energy storage capacity, the height of the storage matrix sections can be reduced, resulting in the same amount of PCM in the TES device. The conductance associated with this proposed design is enumerated in Table 4.7.

The result of this reduction in metal in the storage matrix is shown here. As evidenced by Fig. 4.8, the melting and extraction processes take only slightly longer than their 100 fins/inch counterpart prediction. This indicates that a cheaper design, using 1/4 of the metal in the storage matrix, would still produce a TES device that performs within the desired time. When considering an optimal design for a specific application, the designer will match the size with the operation time for given temperature conditions, as was demonstrated in the case study in Chapter 3.

## 4.6 Conclusions

The work discussed in this chapter demonstrates analytical and experimental validation of performance models for high-performance TES designs. We can confidently apply this numerical method having validated it via comparison to an exact analytical solution. Then, we presented a summary of performance tests of a TES unit with lithium nitrate trihydrate phase change material as a storage medium. The experimental research included thorough property determinations and cyclic testing of the PCM. The presented performance data is for complete dual-mode cycles consisting of extraction and charging. The model analysis is found to agree very well with experiments, within 5% for melting and within 18% for freezing. Higher percent deviation with the experimental data is attributed to conditions very near the initiation of freezing. This is a consequence of subcooling that is required to initiate solidification. Given the success of the cold finger techniques discussed herein, we see promise for eliminating these issues in subsequent comparisons. The work presented here demonstrates the viability of thermal energy storage for many latent heat TES applications. Moreover, this research is novel in its demonstration that spatial and temporal variation within a TES device can be effectively simulated and validated.

# Chapter 5

# Buildings Applications

## 5.1 Motivation

Buildings in the United States use 71% of our nation's electricity and produce 40% of the nation's greenhouse gases [54]. Thus, improving energy technology in buildings is crucial to addressing environmental and economic struggles that will continue to increase air pollution and burden both residential and commercial building owners with a high cost of energy. The implications of this large, and ever increasing, building energy demand is an issue that can be met with a consistent and efficient local technology like thermal energy storage [28]. Thermal energy storage is not particularly new in buildings. For many years, humans have employed thermal masses, like adobe walls, to store sensible energy and maintain comfortable temperatures despite diurnal fluctuations. By using solid-liquid phase change material in a TES device, both sensible and latent energy can be captured, greatly increasing the storage capacity currently available in buildings [59]. Simply put, the PCM will be frozen at night with a chiller and melted during peak daytime temperatures to supplement cooling. This can be used to shift energy demands to off-peak times when electricity is cheaper and air conditioning systems are more efficient.

Energy is primarily used in commercial and residential buildings to meet the cooling load via the refrigeration cycle. The energy efficiency of the refrigeration cycle is also directly tied to the temperature difference experienced by the working fluid. Energy use varies throughout the day, typically peaking at the hours of highest outside temperature and highest cooling load. This chapter examines the implementation of thermal energy storage to shave peak energy demand during the most critical hours. By providing a cold reservoir to capture heat during peak occupancy and outside temperatures, the entire refrigeration cycle is rendered more energy efficient. This heat sink allows for a consistent baseload electricity demand on the city grid or local power plant, eliminating the need for less efficient and higher polluting peak power plants. To be specific, a TES subsystem for building cooling would directly feed water-cooled pre-conditioning coils or indirectly augment vapor compression cycle heat pump performance.

## 5.2 Analysis Framework

With this motivation, we apply our subsystem model from Chapter 3 of a thermal energy storage device and a coupled heat exchanger (HX) to improve the operation of an air conditioning system (AC) as shown in Figure 5.1. This schematic is simplified to highlight a packaged AC unit and does not show the ductwork, piping, valves, actuators, and controls necessary to operate an HVAC system. In standard cooling applications, building heat is rejected to ambient air. Outside air is usually hot during daytime operation, putting a greater demand on the power consumption of the air conditioner in order to maintain the interior of the building between 20 and 25°C.

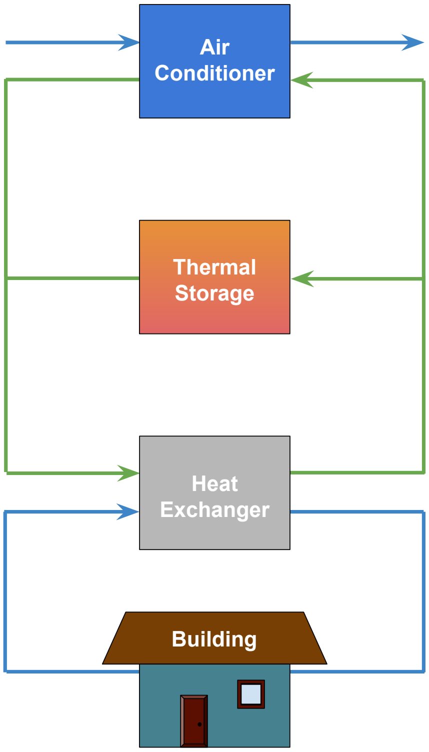

Figure 5.1: System schematic including building, air conditioner, and TES subsystem.

By incorporating a TES subsystem with phase change material into the cooling system, the temperature at which heat is rejected to ambient can be decreased, thereby improving the coefficient of performance (COP) of the air conditioner by demanding less net energy during operation by shifting the load to nighttime when the process is more efficient and electricity is cheaper. Realistic modeling of the building should include the energy generated ($\dot{E}_{gen}$) by people, lights, and appliances as well as the energy lost ($\dot{E}_{loss}$) to the outside environment through walls and windows. For the purposes of this project, a reasonable $\dot{E}_{gen}$

will be found for the building type (residential, commerical, data center) considered and $\dot{E}_{loss}$ can be neglected (provided that the inside temperature is lower than ambient).

## Air Conditioner Energy Balance

The subsystem is connected to an air conditioner, which removes heat from a building. The coefficient of performance of an air conditioner or refrigerator is given by:

$$COP_{\mathrm{R}} = \frac{Q_{low}}{W_{in}} = \frac{Q_{low}}{Q_{high} - Q_{low}} \tag{5.1}$$

For an ideal (reversible) air conditioner, this expression simplifies to:

$$COP_{\mathrm{R,rev}} = \frac{T_{low}}{T_{high} - T_{low}} = \frac{1}{T_{high}/T_{low} - 1} \tag{5.2}$$

Thus, a simple approximation for the COP of a real (irreversible) refrigerator could be:

$$COP_{\mathrm{R}} \approx .60 * COP_{\mathrm{R,rev}} \tag{5.3}$$

where we assume that an irreversible air conditioner might be able to achieve about 60 percent of the COP of a reversible one.

## Air Conditioner Governing Equations

In order to implement the above equations into the program and solve for the improved COP that is achieved with TES, $T_{open,out}$, the temperature of air after the pre-conditioning coil (external HX). This temperature is substituted for $T_{high}$ and the interior building temperature, $T_{room}$, is substituted for $T_{low}$.

$$COP_{\mathrm{R,TES}} \approx .60 * \frac{T_{room}}{T_{open,out} - T_{room}} \tag{5.4}$$

This can be compared to the case without TES by instead setting $T_{hot}$ to $T_{open,in}$, the temperature of ambient air.

$$COP_{\mathrm{R}} \approx .60 * \frac{T_{room}}{T_{open,in} - T_{room}} \tag{5.5}$$

The results can be verified by ensuring that the coefficient of performance of a standard air conditioner is less than that incorporating a thermal energy storage subsystem:

$$COP_{\mathrm{R}} \leq COP_{\mathrm{R,TES}} \tag{5.6}$$

## 5.3 Modelica Implementation

Modelica is a programming language used to develop models, simulate performance, test controls, demonstrate savings, and ultimately design systems. Modelica is declarative, which means that equations are written as (declared) relationships between (declared) variables. This is powerful because the declaration of these variables and relationships is separate from solution of the equations. This means that time is not spent hard coding numerical methods. Instead, a user must have a developed intuition of which solvers to select for the systems being analyzed. Michael Wetter at Lawrence Berkeley Laboratory is leading the development of the Modelica Buildings library specific to building systems simulation and controls [53]. With this resource so readily available, it made sense to port Matlab models into Dymola, a Modelica development environment.

Before constructing complex hybrid HVAC with thermal storage building models, I needed to validate Modelica's capability to effectively capture phase change physics. The model test setup is composed of a connected series of unit cells. On one side of these is the inlet mass flow source, representing the working fluid that enters the heat exchanger, and on the other side is a sink boundary condition. This simulated experimental setup is intended to functionally mimic experimental testing of a real TES prototype discussed in Chapter 4. The temperature of the fluid entering the system is defined by the measured temperatures from these experiments. We also measure the fluid exit temperature entering the sink reservoir.

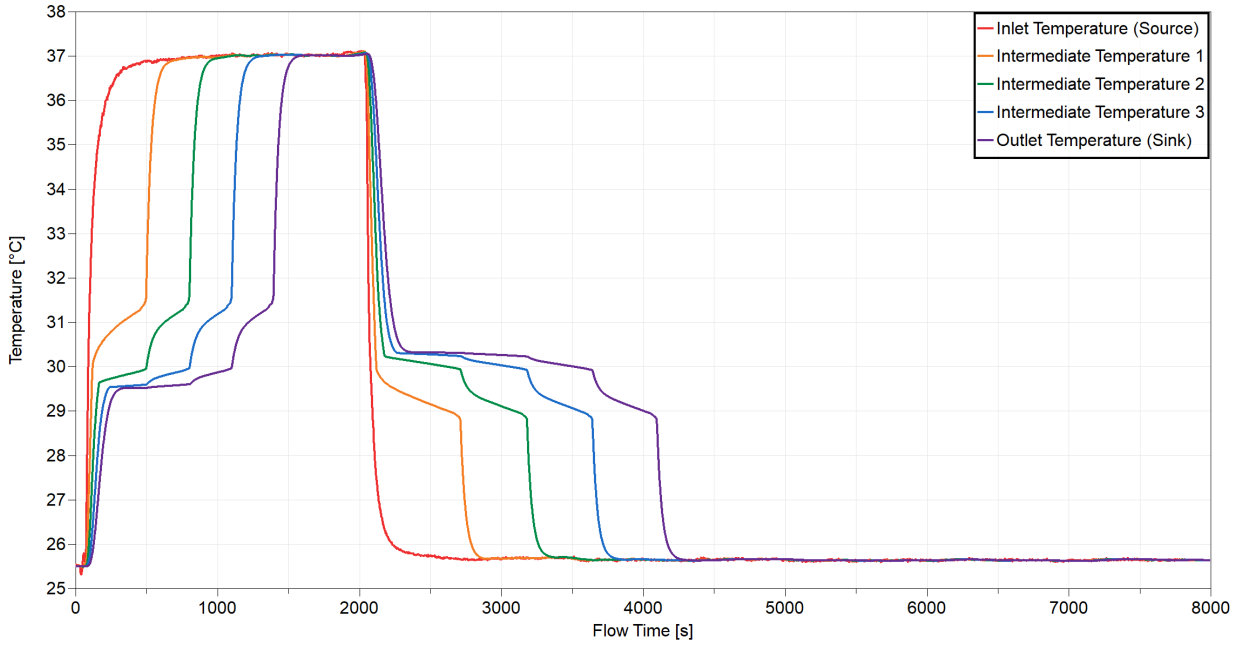

Figure 5.2: Time variation of local temperatures at various locations in the TES unit.

The model for a unit cell of the TES device includes two ports on either side that serve as inlets and outlets for the working fluid. There are also two temperature sensors, one before and one after interaction in the unit cell. At the center is a control volume around a section of working fluid pipe. This transfers heat via convection with the PCM matrix with associated properties documented as a material record. The PCM portion of the unit cell has several nodes of depth similar to the FTCS scheme described in Chapter 2, which terminates at an adiabat at the centerline of the PCM section between flow passages.

During simulation of the melting process, the TES device model was initialized to 25.5 °C, with a time varying inlet temperature boundary condition described above. The Modelica results reveal time variation of local temperatures at various locations in the TES unit from the inlet to the exit from the device, as shown in Figure 5.2. Temperature calculations demonstrate both the cooling effect of the PCM on the working fluid, and the temperature gradient through the PCM.

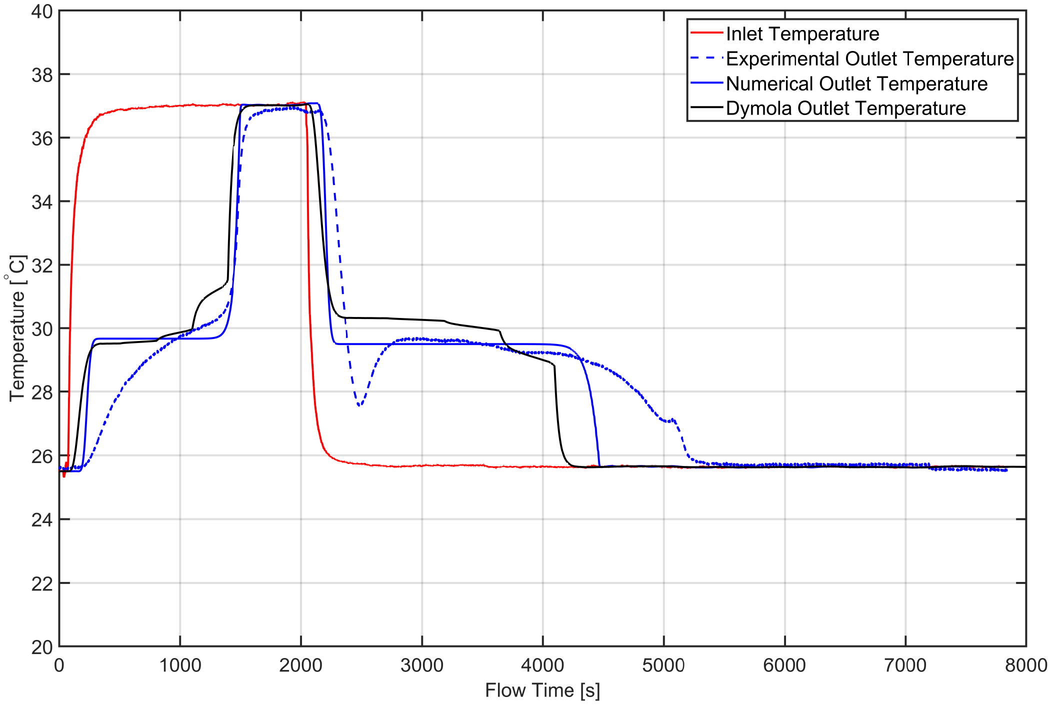

Figure 5.3: Comparison of Matlab and Dymola model simulations with experimental data.

The results from Modelica were imported into Matlab to facilitate comparison to previous studies, including both numerical model predictions and experimental data for the test conditions of a prototype TES unit from Chapter 4. In Figure 5.3, the TES inlet flow temperature is in red. It first increases to melt the PCM and then decreases to initiate freezing of the PCM, thereby producing a complete input/extraction cycle. The dashed blue line is the TES exit temperature from experimental data. The blue solid line is the exit temperature variation predicted by the previously developed first-principles computational model, and the black line is the exit temperature predicted from Modelica simulation.

The main conclusion is that this preliminary Dymola model agrees reasonably well with both the existing model and the data, and time-varying performance (melting and freezing) of the thermal storage is clearly demonstrated. To quantify this, we can compute the correlation coefficient, $R$, between the experimental and numerical results over $N$ points in time:

$$R = \frac{1}{N-1}\sum_{n=1}^{N}\Big(\frac{T_{exp,i} - \mu_{exp}}{\sigma_{exp}}\Big)\Big(\frac{T_{num,i} - \mu_{num}}{\sigma_{num}}\Big) \tag{5.7}$$

where $\mu$ and $\sigma$ are the mean and standard deviation of the temperature respectively.

The correlation coefficient between the experimental data set and Dymola model prediction is 0.911, while the comparison between the experimental data set and first principles model prediction is .944. In comparing the two numerical models, we find that their correlation coefficient is .964. There is a notable lag in Dymola modeled outlet temperature during the melt process compared to the measured performance. This may relate in part to differences between the experimental setup and Dymola model, which may not properly account for conductive pathways that enhance heat transfer. Improvements to the model are needed to increase the agreement between experiments and simulations. Regardless, this comparison, with R values greater than .9, indicates agreement within 10% and validates the use of Modelica for further studies.

## 5.4 Simulation of Rooftop Unit Integrated with Thermal Storage

This initial Dymola model of TES unit performance can be integrated into HVAC system models. These types of simulations are necessary to successfully design the TES subsystem for a commercial building scale HVAC system. Figure 5.4 shows an example rooftop unit (RTU) air conditioning system that utilizes thermal storage to supply chilled air to a room. Air enters the air-cooled chiller from the outside, interacts with a refrigerant, and exits at a higher temperature. Within this chiller, the refrigerant removes heat from water which runs through a closed loop containing both the TES and cooling coil, used to deliver cold supply air to a room. Pumps and valves are controlled by a TES controller, which determines when they are operating.

The PCM matrix in the TES model uses the Single Layer Conduction component in the Modelica Buildings library. The algorithm behind this object is the heat diffusion equation with specific internal energy, $u$, replacing temperature, $T$. Temperature is then modeled as a function of internal energy with a constitutive equation including $T_{sol}$, $T_{liq}$, $h_{ls}$, $c_p$, and $\rho$. This is represented by a cubic hermite spline interpolation with linear extrapolation. The material properties are initially set to those of lithium nitrate trihydrate although this

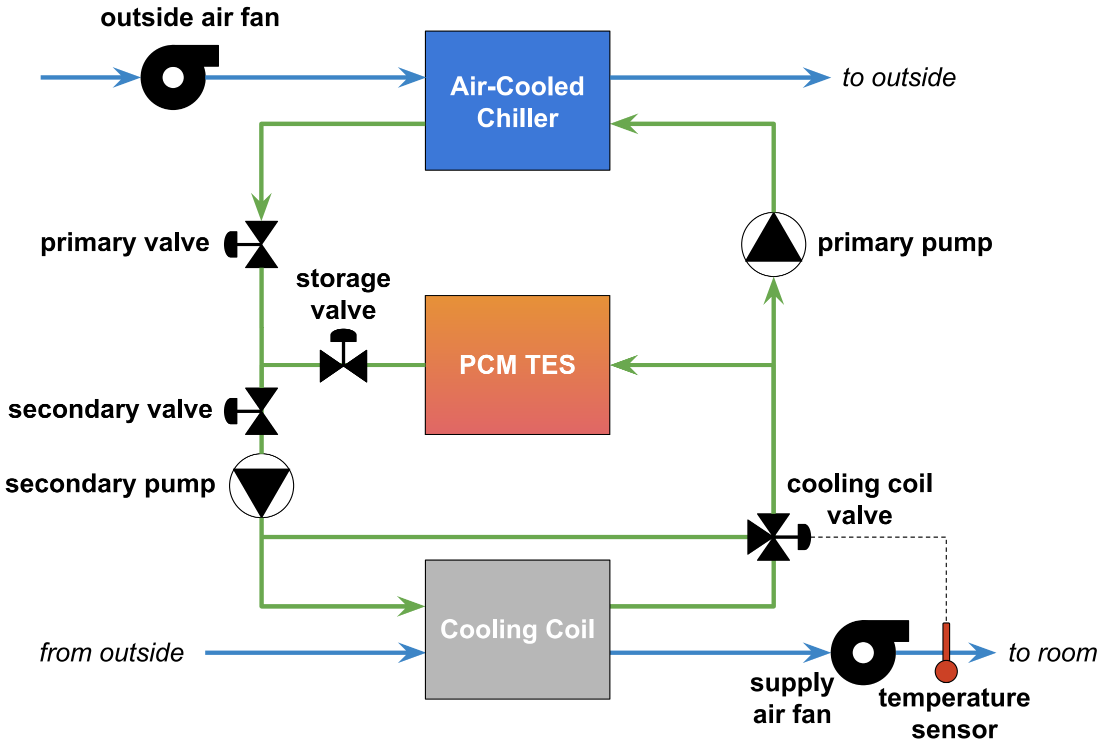

Figure 5.4: Components of building rooftop unit with TES for asynchronous cooling.

PCM should be replaced by something better suited for the application. Lower melting temperature materials are necessary for enhancing building energy systems with phase change thermal storage.

To model heat transfer in the TES unit cell in Modelica, we assume the PCM is exposed to convective heat transfer with the working fluid on one side and an adiabatic boundary condition on the other, as done in previous Matlab modeling. The thickness of the slab between these two boundaries is defined in the PCM material record. On the working fluid side, a constant convective heat transfer coefficient is used, although this could be replaced by a function to determine its value based on the Reynolds number. The heat transfer area mimics the experimental prototype, though it can be updated for different designs.

The full TES model is composed of a series of unit cells and uses the Buildings library Dry Coil Discretized heat exchanger as a basis of design. The model discretizes the TES into a number of heat exchange elements, composed of the most basic heat transfer phenomenon between the working fluid and PCM material. These elements are pieced together as sections of pipe and incorporated into flow models that account for manifolds to divide the flow and compute pressure drop in each parallel pipe. This model can have any number of parallel and sequential pipes according to user parametrization.

The RTU model is relatively simple; it brings in outside air, conditions it with an air-

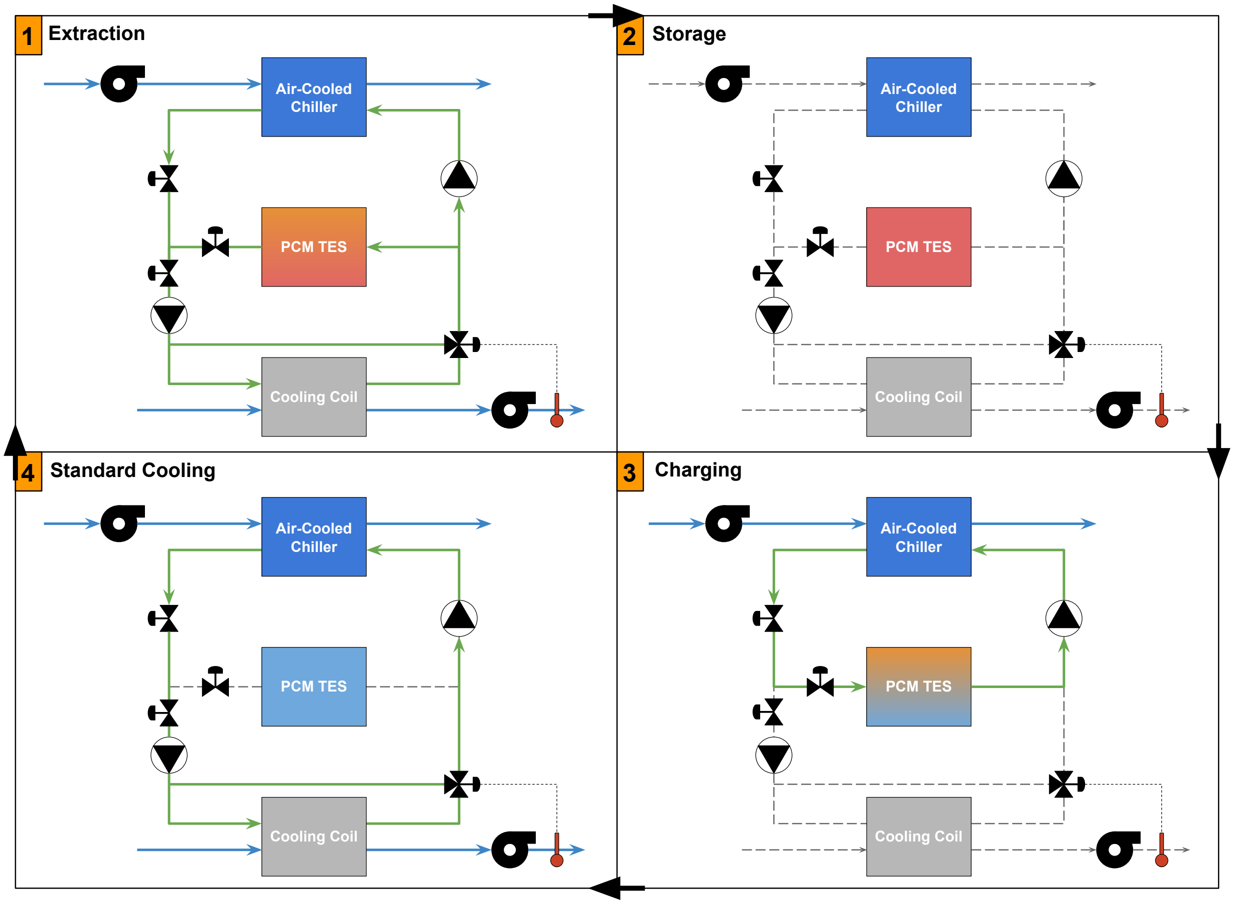

Figure 5.5: Complete daylong cycle of rooftop unit with thermal storage subsystem.

cooled chiller, and supplies it to a single thermal zone with a supply fan. The chiller generates chilled water for supply air cooling as well as charging the PCM. The supply air to the room is thus conditioned by a preconditioning coil sourced from the PCM during extraction and a cooling coil sourced from the air-cooled chiller.

The chilled water loop can be operated in two modes to interact with the TES, as depicted in Figure 5.5. During charging, the primary pump is used to circulate water through the chiller and TES, charging the PCM for cooling. The PCM is charged through both freezing and subcooling down to the chilled water supply temperature. During extraction, the valves are switched such that the primary pump circulates chilled water through the chiller and the cooling coil pipe network, utilizing a three-way mixing valve for control of flow through the cooling coil. A secondary pump is used to circulate water through the TES and preconditioning coil pipe network, also utilizing a three-way mixing valve for control of flow through the preconditioning coil. The water from discharging, preconditions the incoming supply air, as was done in the case study examples for power plants in previous chapters. The cooling coil subsequently conditions the supply air to meet the setpoint.

## 5.5 RTU Test Results

Initial tests for the RTU were performed for a daylong cycle in Denver, CO, with weather data for a typical summer day. A baseline RTU was developed to compare against the RTU with thermal storage. The baseline RTU is modeled in the same way as the RTU with thermal storage except that the components associated with the TES unit are removed. For this test, the RTU model was sized for delivering the proper amount of cooling to the space, with details in Table 5.1. In addition, the original TES was scaled up in order to increase the amount of PCM in the heat exchanger for appropriately serving the building load.

Table 5.1: Input parameters for thermal storage performance calculations in Modelica.

Chiller

| | | |
|---|---|---|
| Nominal Capacity, $P_{nom}$ | 471.2 | kW |
| Nominal Performance, $COP_{nom}$ | 5.89 | |

TES

| | | |
|---|---|---|
| PCM storage matrix section height, $H_{pcm}$ | 4.5 | cm |
| Number of working fluid channels, $N_{wf}$ | 12 | |
| Specific heat of PCM storage matrix, $c_{p,s}$ | 2369 | J/kg K |
| Density of PCM storage matrix, $\rho_s$ | 1809 | kg/m$^3$ |
| Thermal conductivity of PCM storage matrix, $k_s$ | 32.09 | W/m K |
| Latent heat of fusion of PCM, $h_{ls}$ | 202.87 | kJ/kg |
| PCM solidus temperature, $T_{sol}$ | 10 | °C |
| PCM liquidus temperature, $T_{liq}$ | 10.5 | °C |
| Convective heat transfer coefficient, $h_{wf}$ | 3470 | W/m$^2$ K |

Heat Exchanger

| | | |
|---|---|---|
| Effectiveness, $\varepsilon_{hx}$ | .8 | |

The results show the ability for the RTU integrated with thermal storage to maintain the cooling setpoint while shifting a portion of the peak load to the early morning charging hours. This can be seen in Figure 5.6, where high temperatures above the melting temperature of the PCM (10°C) occur outside but do not permeate the room.

To evaluate the improvement to the air conditioning system, we can consider cycle analysis for the vapor-compression refrigeration system within the air-cooled chiller, as shown in Figure 5.7. From Equation 5.1, we can see that the coefficient of performance of a refrigerator is the ratio of the cooling effect it provides to the work input required to achieve this.

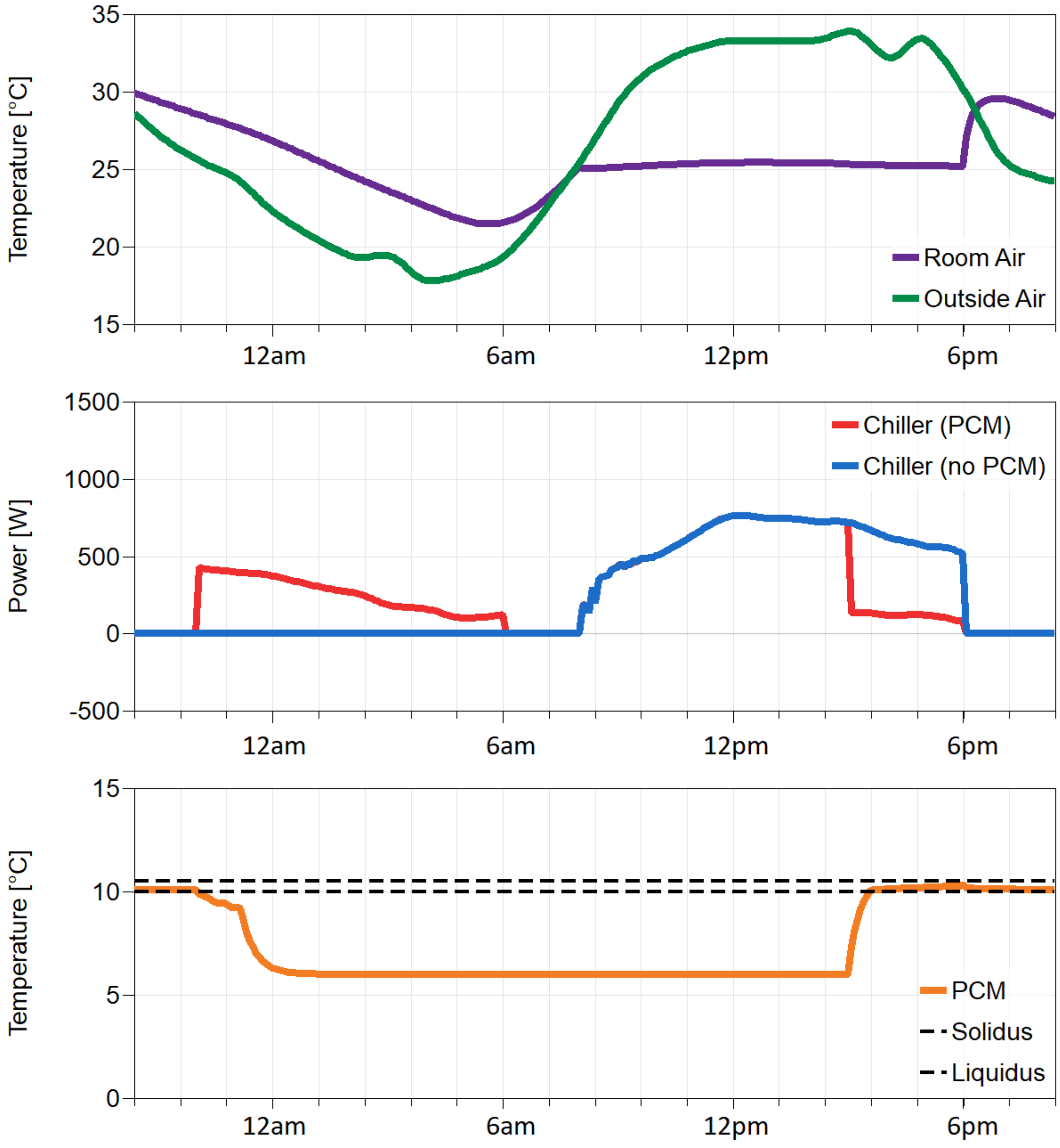

Figure 5.6: Room air and outside air temperature, chiller power consumption, and PCM temperature for daylong simulation of the baseline RTU and RTU with asynchronous cooling.

Thus, in order to maximize $COP_R$, we can either increase heat removed from the refrigerated space, decrease the net work input to the refrigerator, or, from a Carnot standpoint, bring $T_{high}$ and $T_{low}$ closer together.

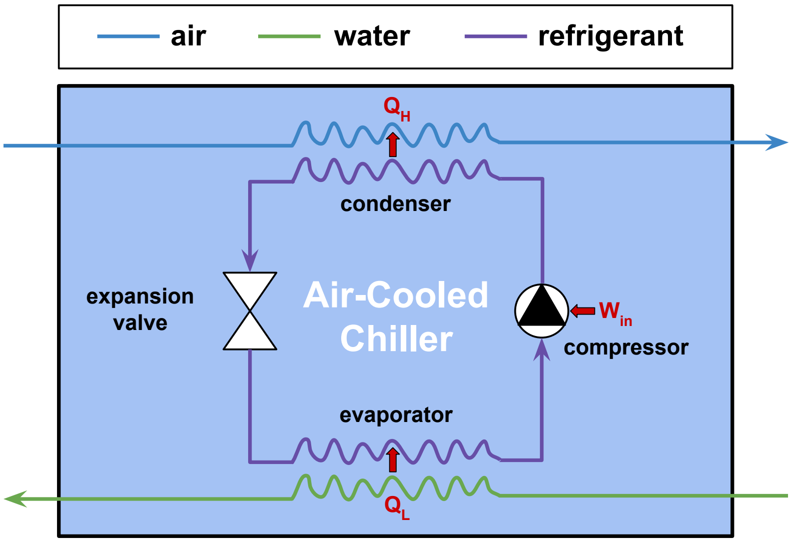

Figure 5.7: Details of vapor-compression system within the rooftop unit air-cooled chiller.

Over the period tested, the final energy consumption of the chiller of the RTU integrated with thermal storage is 2.4% less than the RTU without asynchronous cooling due to shifting of chiller usage to hours with lower outside air temperatures, thereby improving the efficiency of the chiller. The performance can be further improved with selection of PCM material with a lower melting temperature and improved charging and discharging control strategies.

## 5.6 Future Work

The noteworthy outcomes detailed above impact the next steps that should be taken to further explore the use of thermal storage for asynchronous cooling in buildings applications.

### Lower Melt Temperature Phase Change Materials

The material properties listed in Table 5.1 do not match any known phase change material. Instead these reflect the effective properties of lithium nitrate trihydrate in a metal matrix with reduced solidus and liquidus temperatures. Several existing salt hydrates with low melting temperatures might effectively fit building energy needs, including lithium chlorate trihydrate, sodium hydroxide hydrate, and potassium fluoride tetrahydrate with properties shown in Table 5.2 [16, 41, 1, 19, 13, 58, 10].

Table 5.2: Low melting temperature salt hydrate phase change materials.

| PCM | $T_m$ | |
|---|---|---|
| $LiClO_3 \cdot 3H_2O$ | 8.1 | °C |
| $NaOH \cdot 3.5H_2O$ | 15.4 | °C |
| $KF \cdot 4H_2O$ | 18.5 | °C |

There are also varieties of paraffin wax available from commercial sellers like Rubitherm (e.g. RT11 HC) and Climator (e.g. ClimSel C10).

## Improved Control Strategies

The charging and discharging modes are currently controlled through a single Boolean input signal. The control of the mixing valves for both coils is done through a feedback proportional controller based on coil exit temperature setpoints. This preliminary control of the RTU integrated with TES can be improved in the future through use of model predictive control (MPC) to optimize flow rates as well as operation times, as explored in Figure 5.8 for a vapor compression heat pump with TES.

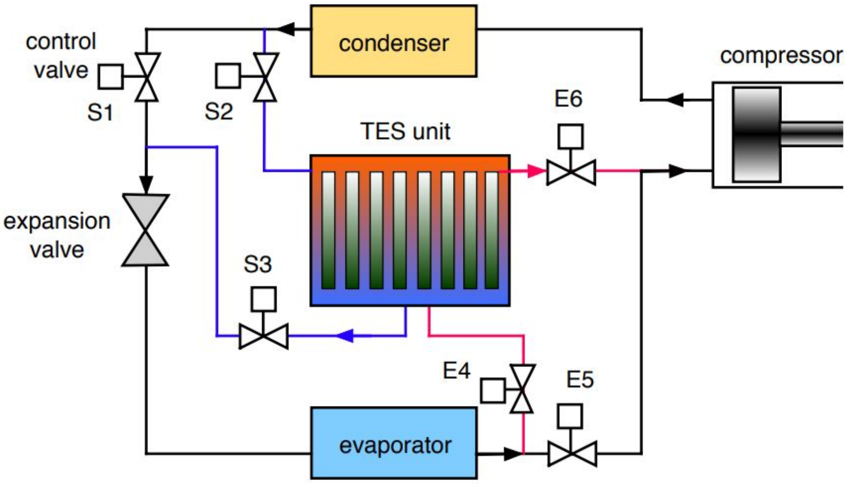

Figure 5.8: MPC can be used to modulate control valves for baseline, storage (S2, S3), and heat input (E4, E6) modes for the heat pump system.

# Chapter 6

# Concluding Remarks

In the previous chapters, I investigate sensible and latent heat transfer through heat exchanger matrix structures containing phase change material in the interstitial spacing. The heat transfer is driven by a temperature difference between fluid flow passages and the phase change material matrix which experiences sensible heat transfer until it reaches the phase change material fusion point; then it undergoes melting or solidification in order to input, or reject, energy. A dimensionless framework was established to model heat transfer in a thermal energy storage device much like effectiveness-NTU analysis methods for compact heat exchangers [27]. A key difference, however, is that in TES units, the overall heat transfer coefficient, $U$, within the phase change material matrix varies spatially in the unit and with time during charging or extraction. Determination of a mean $U$ for these processes was key to applying the effectiveness-NTU analysis to design of a TES unit. Chapter 2 assessed and identified strategies for determining the matrix overall heat transfer coefficient in a TES unit from model predictions.

In order to capture the effects of changing thermal resistance between the working fluid and melt front location, Chapter 2 presented a method using a resistor network analogy to account for thermal conductance as a function of melt fraction. This expression for thermal conductance is then implemented into the numerical framework developed in Chapter 1. Results are validated by comparing calculations for a single unit cell using a quasi-steady Stefan problem approach as well as a finite difference scheme. The variable approach was then compared with an average value for the overall heat transfer coefficient, U, to characterize the performance of a thermal energy storage unit consisting of a series of these unit cells. Overall effectiveness in the thermal energy storage device is found to be within 0.6% agreement when comparing these methods, though local percent deviation can be as high as 113%. Depending on the needed accuracy and use case for such a numerical framework, suggestions are provided on whether an average value for U is sufficient for characterizing such a thermal energy storage device. Discussion is also provided on the flexibility of the computation schemes described by testing the sensitivity of the results via changes in dimensionless input parameters.

Chapter 3 established a multi-scale design evaluation framework that integrates performance models for a thermal energy storage unit and a subsystem heat exchanger. The modeling facilitates analysis of transient input and extraction processes for the thermal energy storage device. The TES is examined within the context of a larger subsystem to illustrate how a high efficiency design target can be established for specified operating conditions that correspond to a variety of applications. The general applicability of the model framework is discussed and example performance calculations are presented for enhancement of a power plant via asynchronous cooling.

Subsystem heat exchangers cool down the storage at night when air temperatures are low; this cold storage is subsequently used to precool the air flow for a power plant air-cooled condenser during peak daytime air temperatures. This is computationally linked to a model of Rankine cycle power plant to predict how much additional power the plant could generate as a result of the augmentation provided by this subsystem. The goal of this study is to use this model to explore the parametric effects of changing phase change material, melt temperature, and the energy input and rejection control settings for the system. Operating conditions of interest were the mass flow rate of fluid through the TES flow passages, the volume of the TES, and the amount of time the system remains in the extraction process, and the PCM melt temperature. These conditions were varied to find combinations that maximized efficiency for a power plant operating in the desert regions of Nevada during an average summer day. The results suggest that for a full-sized power plant with a nominal capacity of 50 MW, the kWh output of the plant can be increased by up to 3.25% during the heat input/cold extraction period contingent on input parameters. Peak power output enhancements were observed to occur when the system operated in the extraction phase during limited hours near the peak temperatures experienced throughout a day, while total kWh enhancement was shown to increase as the extraction period increased. For the most optimized conditions, cost analyses were performed, and it was estimated that the TES system has the potential to provide additional revenue of up to $\sim$ \$5,500 per day, depending on input parameters as well as the local cost of electricity. Results suggest that with further adjustments in system parameters, weather data input, and control strategies, the predicted enhancement of the power output can be increased above the initial predictions reported here.

Model predictions of thermal energy storage performance explored in Chapters 2 and 3 is experimentally validated in Chapter 4. I presented a summary of performance tests of a high-performance TES unit using lithium nitrate trihydrate phase change material as a storage medium. The experimental program included thorough property determinations and cyclic testing of the PCM. Performance data was presented for complete dual-mode cycles consisting of extraction followed by charging. These tests simulate the daylong cyclic operation of a TES unit for asynchronous cooling in a power plant as initially explored in Chapter 3. The model analysis is found to agree very well, within 10%, with the experimental data except for conditions very near the initiation of freezing. Slight deviation from the predicted performance at that time is a consequence of subcooling that is required to initiate solidification. The comparisons presented here demonstrated the viability of thermal energy storage for augmentation of power plant air-cooled condensers as well as other potential applications.

In exploring these other applications, we developed an initial TES model in Modelica, incorporating unit cell heat transfer in the storage unit with modeling of the component scale time and space varying temperature of the phase change material and working fluid. Validation with previous experimental and numerical findings was necessary to move forward in designing the TES for a commercial building scale HVAC system. Chapter 5 describes the development of this model for the testing of a building rooftop unit integrated with TES. The results show the ability for this enhanced RTU to maintain the cooling setpoint while shifting a portion of the peak load to the early morning charging hours. The final energy consumption of the chiller in the TES integrated system is reduced due to shifting of chiller usage to hours with lower outside air temperatures, improving the efficiency of the chiller. The performance can be further improved with selection of PCM material with a lower melting temperature and better charging and discharging control strategies.

# Bibliography

[1] A Abhat. “Low temperature latent heat thermal energy storage: heat storage materials”. In: *Solar energy* 30.4 (1983), pp. 313–332.

[2] Hans T Aichlmayr and FA Kulacki. “The Effective Thermal Conductivity of Saturated Porous Media”. In: *Advances in Heat Transfer* 39 (2006), pp. 377–460.

[3] MM Alkilani et al. “Output Air Temperature Prediction in a Solar Air Heater Integrated with Phase Change Material”. In: *European Journal of Scientific Research* 27.3 (2009), pp. 334–341.

[4] C Bellecci and M Conti. “Transient Behaviour Analysis of a Latent Heat Thermal Storage Module”. In: *International Journal of Heat and Mass Transfer* 36.15 (1993), pp. 3851–3857.

[5] Theodore L Bergman et al. *Fundamentals of Heat and Mass Transfer*. John Wiley & Sons, 2011.

[6] Nadezhda S Bondareva and Mikhail A Sheremet. “3D natural convection melting in a cubical cavity with a heat source”. In: *International Journal of Thermal Sciences* 115 (2017), pp. 43–53.

[7] Jacques Bony and Stéphane Citherlet. “Numerical Model and Experimental Validation of Heat Storage with Phase Change Materials”. In: *Energy and Buildings* 39.10 (2007), pp. 1065–1072.

[8] AMC Chan, P Smereka, and M Shoukri. “An Approximate Analytical Solution to the Freezing Problem Subject to Convective Cooling and with Arbitrary Initial Liquid Temperatures”. In: *International Journal of Heat and Mass Transfer* 26.11 (1983), pp. 1712–1715.

[9] California Energy Commission et al. *Database of California Power Plants*. 2012.

[10] Jose Pereira Da Cunha and Philip Eames. “Thermal energy storage for low and medium temperature applications using phase change materials–a review”. In: *Applied Energy* 177 (2016), pp. 227–238.

[11] Hisham El-Dessouky and Faisal Al-Juwayhel. “Effectiveness of a Thermal Energy Storage System Using Phase-Change Materials”. In: *Energy Conversion and Management* 38.6 (1997), pp. 601–617.

[12] Ibrahim Dincer and Marc Rosen. *Thermal Energy Storage: Systems and Applications*. John Wiley & Sons, 2002.

[13] Mohammed M Farid et al. "A review on phase change energy storage: materials and applications". In: *Energy conversion and management* 45.9-10 (2004), pp. 1597–1615.

[14] Hassan ES Fath. "Heat Exchanger Performance for Latent Heat Thermal Energy Storage System". In: *Energy Conversion and Management* 31.2 (1991), pp. 149–155.

[15] Lauren B Gagnon, Dre Helmns, and Van P Carey. "Multi-Scale Modeling of Power Plant Performance Enhancement Using Asynchronous Thermal Storage and Heat Rejection". In: *ASME 2018 International Mechanical Engineering Congress and Exposition*. American Society of Mechanical Engineers. 2018, V08BT10A021–V08BT10A021.

[16] K Gawron and J Schröder. "Properties of some salt hydrates for latent heat storage". In: *International Journal of Energy Research* 1.4 (1977), pp. 351–363.

[17] MA Hamdan and FA Elwerr. "Thermal Energy Storage Using a Phase Change Material". In: *Solar Energy* 56.2 (1996), pp. 183–189.

[18] RL Hamilton and OK Crosser. "Thermal Conductivity of Heterogeneous Two-Component Systems". In: *Industrial & Engineering Chemistry Fundamentals* 1.3 (1962), pp. 187–191.

[19] SM Hasnain. "Review on sustainable thermal energy storage technologies, Part I: heat storage materials and techniques". In: *Energy conversion and management* 39.11 (1998), pp. 1127–1138.

[20] Andrea Helmns. "Modeling of Heat Transfer and Energy Efficiency of Thermal Energy Storage Incorporating Phase Change Material". MA thesis. UC Berkeley, Dec. 2016.

[21] Andrea Helmns and Van P Carey. "Modeling of heat transfer and energy efficiency performance of transient cold storage in phase change thermal storage components". In: *ASME 2016 Heat Transfer Summer Conference*. American Society of Mechanical Engineers. 2016, V001T05A009–V001T05A009.

[22] Andrea Helmns and Van P Carey. "Modeling of intramatrix heat transfer in thermal energy storage for asynchronous cooling". In: *ASME 2017 Heat Transfer Summer Conference*. American Society of Mechanical Engineers. 2017, V001T09A006–V001T09A006.

[23] Andrea Helmns and Van P Carey. "Multiscale Transient Modeling of Latent Energy Storage for Asynchronous Cooling". In: *Journal of Thermal Science and Engineering Applications* 10.5 (2018), p. 051004.

[24] Yang Hu et al. "Lattice Boltzmann simulation for three-dimensional natural convection with solid-liquid phase change". In: *International Journal of Heat and Mass Transfer* 113 (2017), pp. 1168–1178.

[25] KAR Ismail and MM Goncalves. "Thermal Performance of a PCM Storage Unit". In: *Energy Conversion and Management* 40.2 (1999), pp. 115–138.

[26] Yogesh Jaluria. *Computer Methods for Engineering with Matlab Applications.* Taylor & Francis, Inc., 2012.

[27] William Morrow Kays and Alexander Louis London. *Compact Heat Exchangers.* McGraw-Hill, New York, NY, 1984.

[28] Amar M Khudhair and Mohammed M Farid. "A Review on Energy Conservation in Building Applications with Thermal Storage by Latent Heat Using Phase Change Materials". In: *Energy Conversion and Management* 45.2 (2004), pp. 263–275.

[29] Navin Kumar and Debjyoti Banerjee. "Characterization Phase Change Materials (PCM) Using T-History Method". In: *ASME 2016 Heat Transfer Summer Conference collocated with the ASME 2016 Fluids Engineering Division Summer Meeting and the ASME 2016 14th International Conference on Nanochannels, Microchannels, and Minichannels.* American Society of Mechanical Engineers. 2016, V001T01A014–V001T01A014.

[30] Navin Kumar and Debjyoti Banerjee. "Phase Change Materials". In: *Handbook of Thermal Science and Engineering* (2018), pp. 2213–2275.

[31] M. Lacroix. "Study of the heat transfer behavior of a latent heat thermal energy storage unit with a finned tube". In: *International Journal of Heat and Mass Transfer* 36.8 (1993), pp. 2083–2092. ISSN: 0017-9310. DOI: `https://doi.org/10.1016/S0017-9310(05)80139-5`. URL: `http://www.sciencedirect.com/science/article/pii/S0017931005801395`.

[32] Randall J LeVeque. *Finite Difference Methods for Ordinary and Partial Differential Equations: Steady-State and Time-Dependent Problems.* Siam, 2007.

[33] G. S. H. Lock. *Latent Heat Transfer: An Introduction to Fundamentals.* Oxford University Press, 1994. ISBN: 0198562853.

[34] V. J. Lunardini. *Heat Transfer in Cold Climates.* Van Nostrand Reinhold Company, 1981. ISBN: 0442262507.

[35] V. J. Lunardini. *Heat Transfer with Freezing and Thawing.* Elsevier Science Publishing Company, 1991. ISBN: 0444889051.

[36] Harald Mehling and Luisa F Cabeza. *Heat and Cold Storage with PCM.* Springer, 2008.

[37] VH Morcos. "Investigation of a Latent Heat Thermal Energy Storage System". In: *Solar & Wind Technology* 7.2-3 (1990), pp. 197–202.

[38] Bruce R Munson et al. *Fundamentals of Fluid Mechanics.* John Wiley & Sons, 2013.

[39] Kinga Pielichowska and Krzysztof Pielichowski. "Phase change materials for thermal energy storage". In: *Progress in materials science* 65 (2014), pp. 67–123.

[40] Anand P Roday and Michael J Kazmierczak. "Melting and Freezing in a Finite Slab Due to a Linearly Decreasing Free-Stream Temperature of a Convective Boundary Condition". In: *Thermal Science* 13.2 (2009), pp. 141–153.

[41] J Schröder and K Gawron. "Latent heat storage". In: *International Journal of Energy Research* 5.2 (1981), pp. 103–109.

[42] Patrick J Shamberger and Timothy Reid. "Thermophysical Properties of Lithium Nitrate Trihydrate from (253 to 353) K". In: *Journal of Chemical & Engineering Data* 57.5 (2012), pp. 1404–1411.

[43] N Shamsundar and R Srinivasan. "Effectiveness-NTU Charts for Heat Recovery from Latent Heat Storage Units". In: *Journal of Solar Energy Engineering* 102.4 (1980), pp. 263–271.

[44] Atul Sharma et al. "Review on Thermal Energy Storage with Phase Change Materials and Applications". In: *Renewable and Sustainable Energy Reviews* 13.2 (2009), pp. 318–345.

[45] RN Smith, TE Ebersole, and FP Griffin. "Heat Exchanger Performance in Latent Heat Thermal Energy Storage". In: *Journal of Solar Energy Engineering* 102.2 (1980), pp. 112–118.

[46] A.D. Solomon. "A relation between surface temperature and time for a phase change process with a convective boundary condition". In: *Letters in Heat and Mass Transfer* 6.3 (1979), pp. 189–197. ISSN: 0094-4548. DOI: `https://doi.org/10.1016/0094-4548(79)90037-7`. URL: `http://www.sciencedirect.com/science/article/pii/0094454879900377`.

[47] Domingo Alberto Tarzia. "Relationship Between Neumann Solutions for Two-Phase Lamé-Clapeyron-Stefan Problems with Convective and Temperature Boundary Conditions". In: *arXiv:1406.0552* (2014).

[48] NHS Tay, M Belusko, and F Bruno. "An Effectiveness-NTU Technique for Characterising Tube-In-Tank Phase Change Thermal Energy Storage Systems". In: *Applied Energy* 91.1 (2012), pp. 309–319.

[49] "The Other Foot Print". In: *EPRI Journal* 2 (2010), p. 11. URL: `http://mydocs.epri.com/docs/CorporateDocuments/EPRI_Journal/2010-Summer/1021445_Footprint.pdf`.

[50] Zachary M Theroff, Dre Helmns, and Van P Carey. "Exploration of Variable Conductance Effects During Input and Extraction of Heat from Phase Change Thermal Storage". In: *ASME 2018 International Mechanical Engineering Congress and Exposition*. American Society of Mechanical Engineers. 2018.

[51] Xinglin Tong, Jamil A Khan, and M RuhulAmin. "Enhancement of Heat Transfer by Inserting a Metal Matrix into a Phase Change Material". In: *Numerical Heat Transfer, Part A Applications* 30.2 (1996), pp. 125–141.

[52] Saied Mohammad Vakilaltojjar and W Saman. "Analysis and Modelling of a Phase Change Storage System for Air Conditioning Applications". In: *Applied Thermal Engineering* 21.3 (2001), pp. 249–263.

[53] Michael Wetter et al. “Modelica buildings library”. In: *Journal of Building Performance Simulation* 7.4 (2014), pp. 253–270.

[54] “Why Do We Need Energy-Efficient Buildings?” In: (2016).

[55] A Cengel Yunus and A Boles Michael. *Thermodynamics: An Engineering Approach.* McGraw-Hill, New York, 2006.

[56] B. Zalba et al. “Review on Thermal Energy Storage with Phase Change: Materials, Heat Transfer Analysis and Applications”. In: *Applied Thermal Engineering* 23.3 (2003), pp. 251–283. ISSN: 1359-4311. DOI: `https://doi.org/10.1016/S1359-4311(02)00192-8`. URL: `http://www.sciencedirect.com/science/article/pii/S1359431102001928`.

[57] Yinping Zhang et al. “A General Model for Analyzing the Thermal Performance of the Heat Charging and Discharging Processes of Latent Heat Thermal Energy Storage Systems”. In: *Journal of Solar Energy Engineering* 123.3 (2001), pp. 232–236.

[58] Dan Zhou, Chang-Ying Zhao, and Yuan Tian. “Review on Thermal Energy Storage with Phase Change Materials (PCMs) in Building Applications”. In: *Applied Energy* 92 (2012), pp. 593–605.

[59] Na Zhu, Zhenjun Ma, and Shengwei Wang. “Dynamic Characteristics and Energy Performance of Buildings Using Phase Change Materials: A Review”. In: *Energy Conversion and Management* 50.12 (2009), pp. 3169–3181.